Proceedings of the 13th Symposium on Ultrasonic Doppler Methods for Fluid Mechanics and Fluid Engineering

ETH Zurich, Switzerland

13 - 15 June 2021

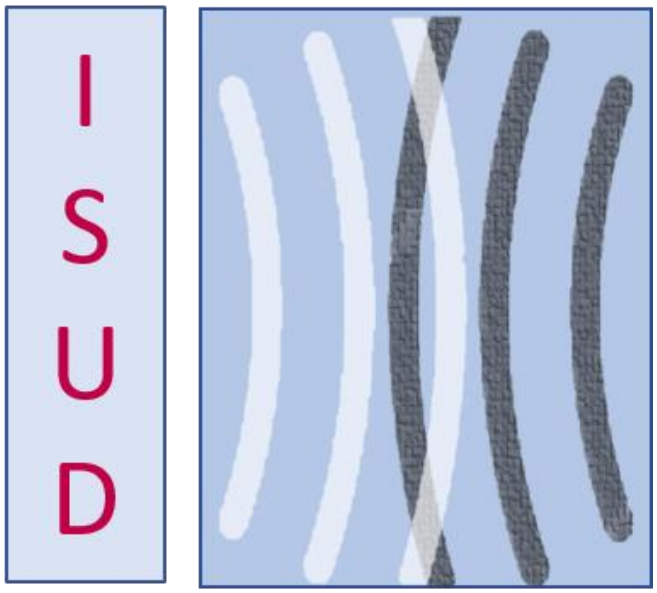

Editors:

Erich J. Windhab, Giovanni DeCesare, Yasushi Takeda, and Kim Mishra

Organizing and Scientific Committee:

Prof. Dr. -Ing. Erich J. Windhab, Dr. Giovanni De Cesare, Prof. Dr. Yasushi Takeda, Prof. Dr. Yuichi Murai, Prof. Dr. Hiroshige Kikura, Prof. Dr. Hideki Murakawa, Prof. Dr. Yuji Tasaka, Dr. Tomonori Ihara, Dr. Lucas Grob, Dr. Kim Mishra

Proceedings of the 13th International Symposium on Ultrasonic Doppler Methods for Fluid Mechanics and Fluid Engineering

ISBN: 978-3-907234-59-4

Published and distributed by:
Laboratory of Food Process Engineering
Institute of Food, Nutrition and Health ETH Zürich,
8092 Zürich,
Switzerland
`https://www.isud-conference.org/`

Printed in Switzerland by:
Print+Publish
ETH Zürich
HIL C 45
Stefano-Franscini-Platz 5
8093 Zürich

Preface

The ISUD 2021 (13^{th}) was held at ETH Zürich from the 13 - 15^{th} of June 2021. The conference took place in hybrid form due to the travel restrictions imposed by the COVID-19 pandemic. Participants from Switzerland, Japan, Korea, USA, Brazil, China, Germany, Sweden and France were present physically or virtually. Both academia and industry was represented at the conference.
The organizational committee would like to express their special thanks to our sponsors of the student awards, Ubertone, Met-Flow and Incipientus which were awarded to Kim Mishra, Sardini Sayidatun Nisa Sailellah and Lucas Grob.
Furthermore, the organizational committee would like to express their deepest gratitude to Patrick Reissner from Belimo AG, who held a talk on the application of US in HVAC processes.
The organizational committee would like to thank and congratulate Prof. Dr.-Ing. Erich J. Windhab for his outstanding dedication and support of the ISUD conference during his time as full professor at ETH Zürich. Professor Windhab will join the emeritus leage end of July 2021. We hope that he is still able to join the 14^{th} ISUD, which will take place **September 2023** in Kobe, hosted by Professor Murakawa of Kobe University.

July 16, 2021

Kim Mishra,
Erich Windhab,
Giovanni De Cesare,
and Yasushi Takeda

Contents

Preface **v**

1 Towards handheld UVP **1**

Marie Burckbuchler and Stéphane Fischer

2 UDV methods for characterizing flows in liquid metal batteries **7**

Jonathan Cheng, Bitong Wang, Ibrahim Mohammad, Gerrit Horstmann and Douglas Kelly

3 Extending Nyquist limit by velocity difference dealiasing rules using a triple PRT scheme **13**

Fabio Rizental Coutinho, Cesar Yutaka Ofuchi, Andre Luis Stakowian, Marco Jose da Silva, Rigoberto Eleazar Melgarejo Morales, Flavio Neves Jr and Susana Lais Silva de Souza

4 In situ ultrasonic measurement of the local liquid fraction of froth flotation **19**

Hannes Emmerich, Richard Nauber, Lars Büttner, Leon Knüpfer, Sascha Heitkam and Jürgen Czarske

5 Investigation and comparison of fluid dynamics in a hydrocyclone using UDVP **23**

Lucas Grob, Eileen Ott, Liridon Zeneli, Yasushi Takeda and Erich J. Windhab

6 Vertical bubbly pipe flow using combined signal of UD and EI profiles **29**

Takumi Hayashi, Hyun Jin Park, Yuji Tasaka and Yuichi Murai

7 Effects of inhomogeneous fluid field on UVP measurement 35

Tomonori Ihara and Tatsuya Hazuku

8 Multi-receiver Correction for VDM of (O/W) 2-phase Flow using Multi-line PWUD 41

Weiling Liu, Hao Liu, Chao Tan and Feng Dong

9 Minimum number of transects for flow measurements using moving vessel ADCPs 47

Mohammad Reza Maddahi, Majid Rahimpour, Robert Boes and Ismail Albayrak

10 Yield stress determination in thixotropic crystal-melt suspensions 53

Kim Mishra, Damien Dufour, Silas Ehrengruber, Julia Merkel and Erich Windhab

11 US remote leakage position estimation method for underwater exploration 59

Takeshi Moriya, Hiroshige Kikura and Hideharu Takahashi

12 UVP applied for Doppler scanning of fruit-internal structures and its working principle 65

Yuichi Murai, Taiki Yoshida, Hyun Jin Park and Yuji Tasaka

13 Measurements of continuously released bubbles motion in liquid-metal using US 71

Hideki Murakawa and Tomonori Shimizu

14 Flow Visualization using UVP and Elemental Analysis using Sonoluminescence 77

Sardini Sayidatun Nisa Sailellah, Hideharu Takahashi and Hiroshige Kikura

15 Viscoelasticity of PVP aq. solutions by novel map repr. based on US spinning rheometry 83

Kohei Ohie, Taiki Yoshida, Yuji Tasaka, Masako Seki and Yuichi Murai

16 FA of (W/O) Emulsion Produced by Taylor-Couette System Using UD and UA Method **89**

Yoshihiko Oishi, Hideki Kawai, Daichi Sasayama and Hiroshige Kikura

17 Measurement of size and velocity of rising bubbles by a vector UVP **95**

Hyun Jin Park, Shintaro Akasaka, Yuji Tasaka and Yuichi Murai

18 Bedload transport assessment on a physical model of a large river widening using UDV **101**

Jean-Noël Saugy, Azin Amini and Giovanni De Cesare

19 UDV as a co-indicator for the eco-morphological assessment in a residual flow reach **107**

Robin Schroff, Christian Moertl and Giovanni De Cesare

20 Advanced UVP Instruments Applicable to 3-D Velocity Vector Measurement **113**

Naruki Shoji, Hideharu Takahashi and Hiroshige Kikura

21 Remote Investigation in FDNPP by Advanced Super Dragon Articulated Robot Arm **119**

Hideharu Takahashi, Naruki Shoji, Gen Endo, Ikuo Wakaida and Hiroshige Kikura

22 Evolving UVP and eUVP **125**

Yasushi Takeda, Hiroshige Kikura and Erich Windhab

23 In-line rheometry based on UVP measurement for non-Newtonian fluids **131**

Yuji Tasaka, Taiki Yoshida and Yuichi Murai

24 UVP-based viscosity and pressure estimation in shear-thinning unsteady flow **137**

Neetu Tiwari and Yuichi Murai

25 Optimal Vessel Materials for Indirect-contact Ultrasound Measurements **143**

Bitong Wang and Douglas Kelley

26 Flow process and rheology control by UD along the FVC from MPP to GI digestion **149**

Erich Windhab, Yasushi Takeda, Damien Dufour, Kim Mishra, Samsun Nahar and Beat Birkhofer

27 The development of UV profiler for velocity vector profile measurement in bubbly flow **155**

Wongsakorn Wongsaroj, Hideharu Takahashi, Natee Thong-Un and Hiroshige Kikura

28 An instantaneous velocity vector measurement using conventional US transducers **161**

Dongik Yoon, Hyun Jin Park and Tomonori Ihara

29 MS for Flow Mapping and Shape Detection using Sectorial Array Sensors **167**

Zeliang Zhang, Munkhbat Batsaikhan, Hideharu Takahashi and Hiroshige Kikura

30 Awards **173**

31 Group Foto **177**

1 Towards handheld UVP

13th International Symposium on Ultrasonic Doppler Methods for Fluid Mechanics and Fluid Engineering
Zürich, Switzerland (13.-15. June 2021)

Towards handheld UVP

Marie Burckbuchler[1], Stéphane Fischer[1]

[1] Ubertone SAS, 14 rue du Brochet, 67300 Schiltigheim, France

Through its hardware size, the installation and handling of UVPs was not convenient. Also the setup complexity limited the UVP technology to trained users or ultrasonic technology experts. In this extended abstract, we present the world's first handheld UVP, which simplifies its use on large setups and moving systems. The UB-Lab P has, through the presented results, proven its efficiency in hydraulics engineering studies on physical models, especially with a moving carriage. The high sensitivity of the UB-Lab P enables measurement even in low scatterers suspension conditions, such as low flow rates. The cloud.ubertone.eu processing and visualization tool allows fast visualisation of raw measured data. It also provides processing scripts to prepare the data for non-acoustics-experts, synchronising carriage positioning systems with velocity measurements, processing the raw Doppler velocity measurements in multi-components vectors and filtering data.

Keywords: UVP, compact, autonomous, hydraulics, flow scanning

1. Introduction

As Ubertone's first goal is to bring the UVP technology to more users and applications, we follow several RTD (research and technology development) axes. One axis concerns the multiplication of measured velocity components along a profile, while keeping a high space-time resolution, which led to the UB-Lab 2C, launched in 2018, a commercial ADVP (Acoustic Doppler Velocity Profilers). Another axis is mobility and easy installation with miniaturisation and autonomy. While UVPs are usually of the size of PC towers, Ubertone released its first compact laboratory UVP in 2011. Continuing in this direction, we launched last september 2020 the UB-Lab P, the world's first handheld UVP, a ready-to-use battery-powered instrument, with an embedded web-interface accessed by wifi.

Apart from the convenience of having instruments of small size and wireless that can be controlled with a smartphone, these characteristics may be a strong advantage when working on large setups, industrial plants or on moving systems. This is the case in many physical models used in hydraulic engineering [1] or on small rivers [2] in which high resolution velocity measurements are needed.

This presentation will focus on the UB-Lab P, with an application example on a physical model of a river section.

2. Material and Method

2.1 The UB-Lab P

The UB-Lab P is a handheld profiler equipped with a Wifi connexion and an internal battery in a compact enclosure. Some specifications are given in Table 1.

Table 1: Specifications of the UB-Lab P

Emitting frequency	0.025 to 3.6MHz
Spatial resolution	Down to 0.73 mm
Cells number	200
Transducers channels	2
Velocity accuracy	0.2 to 1 %
Sampling rate	up to 15 Hz
Trigger	IN/OUT
Communication	Wifi
Weight	0.2 kg
Consumption	2.5 W, on battery

A trigger 'in' or 'out' is available on the device. The input mode has been used in this measurement campaign. When a recording is started through the graphical user interface, the input signal enables the storage of data. Only blocks where the "trigger" signal is at high level (at the beginning and the end of the block) are effectively stored in the record file.

2.2 UVP Measurements

The UVP (Ultrasonic Velocity Profiler) technique has been introduced to Fluid Mechanics by Takeda [3]. This technique based on coherent Doppler provides velocity profiles measurements with a high spatial and temporal resolution. An ultrasonic pulse is emitted in a narrow beam and the particles, suspended in the flow, scatter the pulse. The echoes of the particles are received by the same transducer (monostatic mode) which allows the observation of a profile composed of many measurement cells distributed along the beam axis. The signal is processed providing information of the velocity component projected on the transducer's axis.

Combining cells in two diverging beams allows getting average two-components velocity profiles.

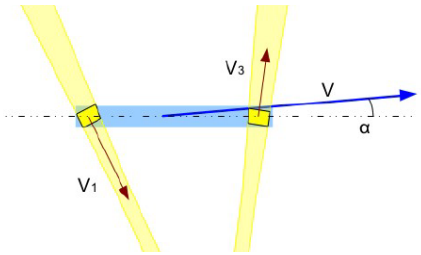

Figure 1: Combining two velocity projections on two transducers to get the velocity vector orientation and module

The backscattered echo amplitude is recorded simultaneously with the velocity measurement. The water level (or of any other interface) can be evaluated by observing a strong variation of the backscattered echo amplitude gradient.

2.3 Setup

The flume is a physical model of a river with a hydraulic structure and is situated in the hydraulics lab hall of the CNR - Compagnie Nationale du Rhône, in Lyon, France.

The maximal depth in the flume is around 50 cm and flow velocities vary from -10 to 50 cm/s.

The CNR was interested in the flow mapping over the whole physical model. They defined a few specific transects of interest.

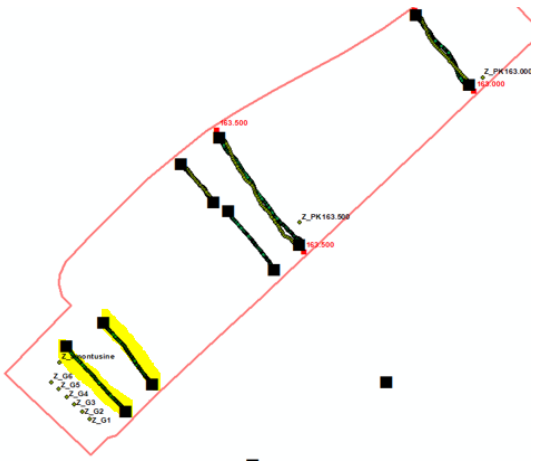

Figure 2: Flume sketch. Hydraulic structure situated downstream in the bottom left corner. Transects of interest indicated with lines.

The flume was equipped with a programmable carriage, recording xyz positions and able to manage a few sensors.

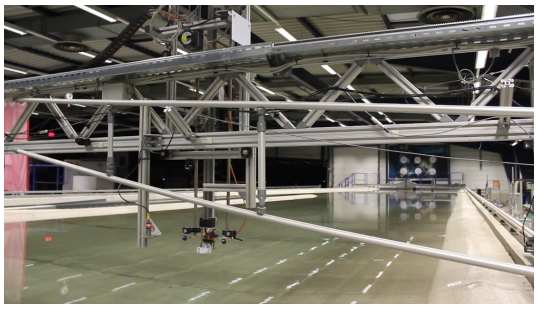

Figure 3: Carriage above the flume

2.4 Installation

The instrument's small size, weight and wireless communication make the installation easy.

As the access to the graphical user interface goes through a common web browser and is compatible with a smartphone, the use of this device is plug-and-play simple.

The internal battery of the UB-Lab P has a 4 hours autonomy. The use of an external power bank can enhance the autonomy up to a few days.

The trigger input of the UB-Lab P was connected to the carriage control unit.

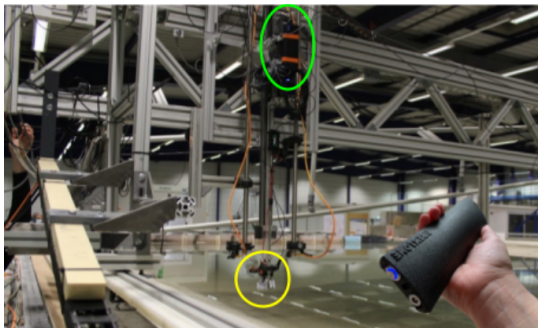

Figure 4: UB-Lab P (within the green circle) installed on the carriage

Two diverging transducers are used to get average two-component velocity profiles along the vertical axis, and a motor orients the transducer holder between U/W or V/W plane.

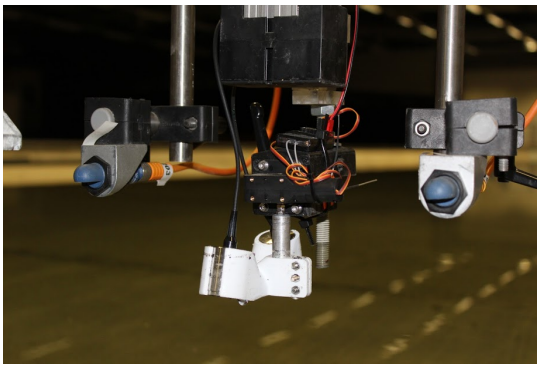

Figure 5: Transducers holder beneath the carriage (within the yellow circle in fig 4)

2.5 Procedure

The recording is started on the UB-Lab P, then the carriage routine is started. Profiles indeed recorded by the UB-Lab P are downloaded, after stopping the recording, in a binary data file (.udt). Human readable .csv files can be extracted from it when uploading it to the cloud.ubertone.eu processing and visualization tool.

The carriage xyz positions are recorded simultaneously and custom scripts on Ubertone's cloud allow synchronizing data from the carriage file with the UB-Lab P data. We also adapted our interface detection to obtain a robust and accurate measurement of the riverbed position, using echo amplitude profiles.

In those scripts, the velocity data beyond the detected interface are kept out and the data are filtered with the Doppler signal-to-noise ratio (SNR) measured by the UB-Lab P. U and W components are processed from the monostatic projected velocities and the Doppler angles given by the user. Other input parameters allow taking into account environment aspects such as model scale, for lab vs field measurement comparisons.

For the measurements presented here, two 3MHz transducers were used, with a spatial resolution of 5mm. The UB-Lab P switched periodically between both transducers to alternate the measurements of both monostatic components. Each cycle lasted about 1s.

3. Results and Discussion

3.1 Dynamic measurements

The first routine was to scan several transects and record continuously during the displacement, the trigger was set to low when transiting between transects to avoid recording.

In the following figures, in each group of three graphs, the first above represents the U component profiles, the central the W component profiles and the one below the distance between the transducer and the flume bed. The y-axis is the depth and the x-axis is the resulting profile number obtained along the transect.

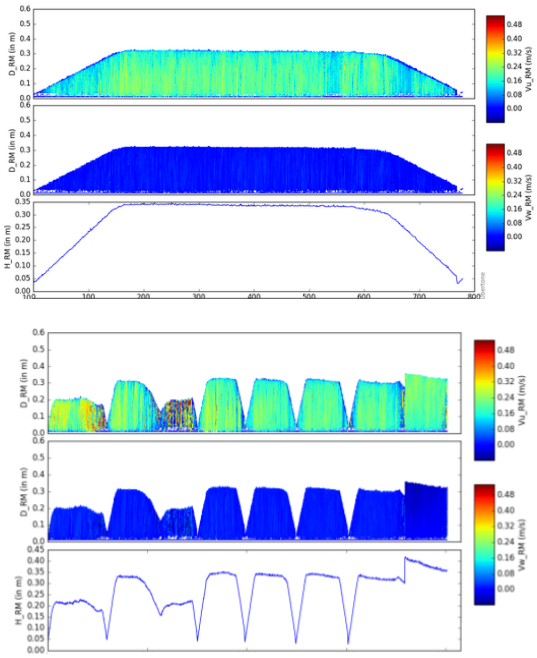

Figure 6: Processed dynamic transects acquisition

3.2 Static measurements

As for some discharge conditions, the signal was weaker, scatterers settling faster, another routine was to measure in fixed positions of the transect for a few seconds. Another script developed by Ubertone on the cloud application then averages the data collected in each fixed position for a better spatial cover.

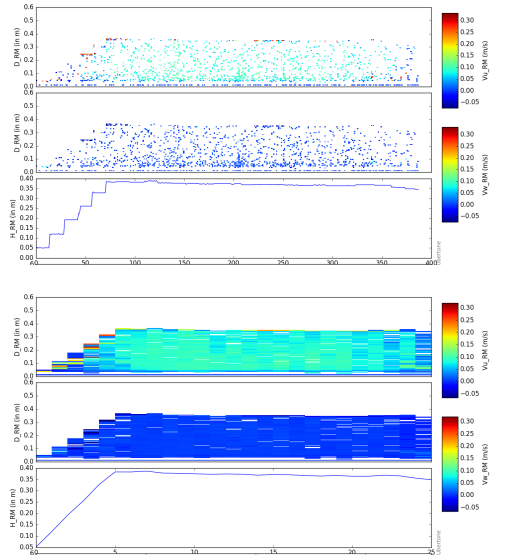

Figure 7: Processed static-positions-wise transect acquisition

In Fig. 7, the first display shows the measurements processed by the dynamic script. The second shows the result after averaging per fixed position.

6. Summary

Using a handheld UVP device can be helpful in mechanical design of setups, especially where the weight of the moving carriage is critical. The wireless communication and plug-and-play simplicity enables easy on-the-spot UVP measurements.

The next step in handyness improvement will be a wireless trigger management.

As shown in this abstract, the UB-Lab P's high sensitivity results in good quality velocity profile measurements even when few scatterers are in suspension. The Doppler SNR filtering improves the quality of the average velocity.

The echo signal is used to detect the bed and prepare the data for post-processing analysis.

The cloud.ubertone.eu processing and visualization web tool easens the work for non-acoustics-experts, providing processing scripts. The data is prepared for further analysis: synchronisation of carriage positions with velocity measurements, processing of raw Doppler velocity measurements in multi-components vectors and data filtering.

Now for hydraulics studies, the following development will be to measure 3 components by adding transducer channels.

References

[1] De Cesare G, *et al.*: River intake and desander efficiency testing on a physical model using UVP and LSPIV, ISUD 7 (2010).

[2] Burckbuchler M & Fischer S: A miniature uvp hardware applied to environmental monitoring, HydroSenSoft (2017).

[3] Takeda Y: Measurement of velocity profile of mercury flow by ultrasound Doppler shift method, Nucl. Technol. 79 (1987), 120-124.

2 UDV methods for characterizing flows in liquid metal batteries

13th International Symposium on Ultrasonic Doppler Methods for Fluid Mechanics and Fluid Engineering
Zürich, Switzerland (13.-15. June 2021)

UDV methods for characterizing flows in liquid metal batteries

Jonathan Cheng[1], Bitong Wang[1], Ibrahim Mohammad[1], Gerrit Horstmann[2], Douglas Kelley[1]

[1] Dep. of Mechanical Engineering, University of Rochester, Rochester, NY 14627, USA
[2] Dep. of Helmholtz-Zentrum Dresden-Rossendorf, Dresden 01328, Germany

We present ultrasound measurements from a laboratory model of a liquid metal battery (LMB). Two major flow drivers interact within LMBs: thermal gradients due to the presence of internal heating, and electrovortex flow (EVF) driven by diverging current densities. The product of these interactions remains poorly characterized. We approach this problem with ultrasonic Doppler velocimetry (UDV) combined with a laboratory model of an LMB fluid layer. Using ultrasound probes placed around a liquid gallium vessel, we elucidate typical velocities, flow structures, and flow statistics in a representative volume of the flow field. UDV measurements reveal that pure convection takes the form of the recently-discovered 'jump rope vortex,' with a characteristic frequency visible in velocity statistics. They also indicate that EVF goes through stable, unstable, and oscillatory flow regimes. In progress is an approach for training physics-informed neural networks (PINNs) on UDV data, allowing us to reconstruct flow in regions where no probe measurements have taken place by leveraging the equations of motion.

Keywords: Industrial flow, Velocimetry, Liquid metals, Convection, Magnetohydrodynamics

1. Introduction

Over the course of a day, energy demand in the US can vary by up to 50% in a given region [1]. For renewable sources like wind and solar power, energy production cannot be dynamically controlled and instead subject to the whims of the environment. This means that a time lag often exists between the hours of peak production and peak demand, requiring rapid ramping of nonrenewable energy supplies which lead to operational inefficiencies and, in the case of a large renewable presence, potential waste of surplus energy. Grid-scale energy storage is one way to curb these inefficiencies. Among the variety of storage technologies in development, liquid metal batteries (LMBs) stand out as being particularly cost-effective [2]. Much of this owes to the liquid nature of the battery: construction becomes simpler, damage to the reactive components is self-healed, and materials are inexpensive.

However, the fluid nature of LMBs lends them a strong propensity for flow: a variety of thermal, chemical, and electromagnetic forces play against one another in both helpful and harmful ways [3,4]. The fluid dynamics occurring in LMBs can be paramount to their operation. Leading approaches to understanding LMB flows generally center on direct numerical simulations [5,6]. However, laboratory experiments provide some distinct advantages: we can efficiently conduct surveys over broad ranges of the governing parameters. By varying two or more forcing factors in the flow, we can construct phase diagrams that indicate when transitions in flow morphology take place. Laboratory setups also allow us to verify whether the physics in idealized simulations actually manifest the same way in real-world settings.

To make laboratory measurements relevant to LMBs, opaque liquid metals must be employed. This greatly limits which velocity measurement techniques are useful; most particle tracking, Schlieren, and dye based techniques become unviable. Ultrasonic Doppler Velocimetry (UDV) is perhaps the best option available under these circumstances. Instead of measuring a 2D flow field, UDV only measures along 1D lines, meaning that special care must be taken in the planning stages to ensure that it succeeds in characterizing the flow field.

In this study, we discuss a variety of methodologies for making UDV measurements within a layer of liquid gallium under thermal and electromagnetic flow forcings. UDV uncovers myriad and interesting flows occurring in a laboratory model of a liquid metal battery. In section 2 we discuss the theoretical background for LMB flows. In section 3, we describe the fundamentals of UDV and the experimental design considerations for optimizing our UDV measurements. In section 4, we show results and elaborate on our postprocessing methods for UDV data.

2. Theoretical background

Figure 1a is a schematic of a liquid metal battery. LMBs are identical in principle to solid batteries: they are galvanic cells with two materials – the cathode and anode – which undergo an energetically favorable reaction. These are separated by a third material in the middle, an electrolyte which allows positive ions through and forces electrons to find an alternate pathway. They are a developing technology, with various container geometries and chemical compositions currently being explored [2]. It is thus important to develop a broad understanding of how different flow forcings interact with one another via scaling laws between governing parameters that can generalized to different systems.

Two of the most prominent drivers of flow are thermal gradients and electromagnetic forces. A thermal gradient which leads to lighter fluid above denser fluid is stabilizing. In the reverse case, unstable thermal gradients lead to convection, characterized by the Rayleigh number:

$$Ra = \frac{\alpha g \Delta T H^3}{\nu \kappa} \quad (1)$$

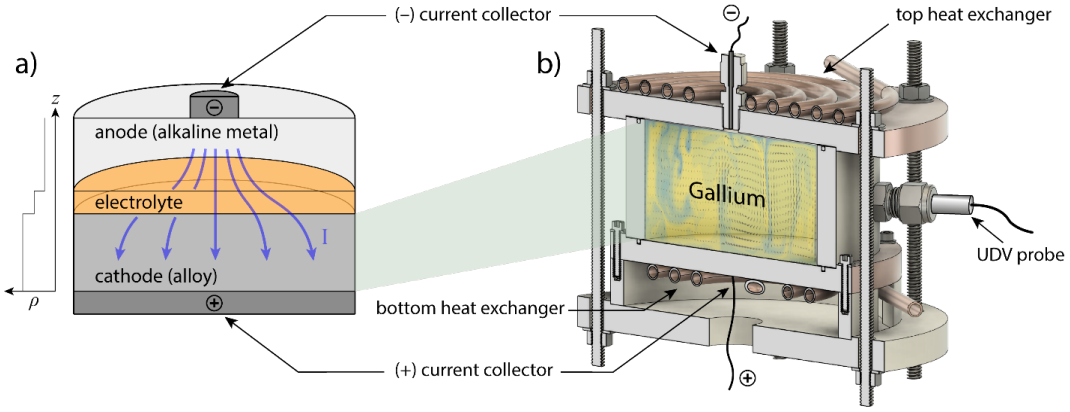

Figure 1: Schematic demonstrating how our novel experimental setup models a layer of a liquid metal battery. Panel a) shows that liquid metal batteries are composed of three fluid layers, each with greater density than the layer above it. The top current collector is typically narrower than the bottom leading to a horizontally diverging current density. Panel b) is a design drawing of our laboratory setup. The top current collector is a narrow copper cylinder while the bottom is the copper plate forming the bottom boundary of the gallium fluid layer. The sidewall of the container is made of nonconductive acetal plastic. UDV probes are placed in the sidewalls and top lid of the setup. The flow field visualized in the container is from simulations by Personnettaz *et al.* [6].

where α is the coefficient of thermal expansion, g is gravitational acceleration, ΔT is the magnitude of the temperature gradient, H is the height of the container, ν is kinematic diffusivity, and κ is the thermal diffusivity.

While many forms of electromagnetic flow could occur in LMBs, we focus on one prominent player known as electrovortex flow (EVF). EVF is induced by horizontally diverging current densities. The strength of EVF is characterized by a so-called EVF parameter [7,8]:

$$S = \frac{\mu_0 I^2}{4\pi^2 \rho \nu^2} \qquad (2)$$

where μ_0 is the vacuum permeability, I is the imposed current, and ρ is the fluid density.

Our apparatus is designed to explore the combination of convection or stable stratification with EVF. One way to quantify the resultant flows with an overall descriptor of system dynamics, the Reynolds number $Re = UD/\nu$ where L is a typical length scale and U is a typical flow speed.

3. Experimental design

3.1 Ultrasonic Doppler Velocimetry

We use Signal Processing transducers to perform our UDV measurements. Velocities are measured along a straight line in front of each probe. Ultrasonic pulses are released in quick succession from the probe and backscattered by particles in the fluid. Velocities as a function of time are determined by the shift in position of these particles between pulses: particles moving toward the probe register a negative velocity while those moving away from the probe have positive velocity. Probes operate at 4 MHz or 8 MHz. Rather than seeding particles in the fluid, naturally occurring oxide particles serve as the scattering agent in our study. Up to 9 ultrasound probes are placed in various locations around the container.

3.2 Apparatus

Figure 1b shows a design drawing of our device. The working fluid is liquid gallium, which is liquid near room temperature, confined to a cylindrical space of diameter $D = 10$ cm and height $H = 5$ cm (Aspect ratio $\Gamma = 2$). The top and bottom boundaries are copper plates. To each plate is soldered a copper coil which serves as a heat exchanger: two thermal baths recirculate water through

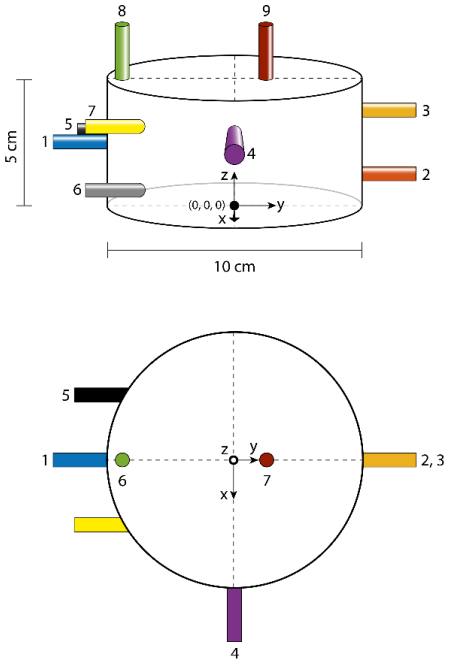

Figure 2: Distribution of UDV probes around the gallium fluid layer. They are positioned to optimally capture expected flow structures in convection and EVF.

each of these coils such that either a stabilizing or destabilizing temperature gradient can be imposed on the gallium layer. The spirals are wound non-inductively to prevent horizontal temperature gradients. The sidewall of the vessel is a 1.1cm thick Delrin cylinder, a non-conductive material that ensures all currents pass through the gallium layer.

Currents from 0 to 90 Amperes are controlled by a power supply. The negative electrode is a copper rod of diameter 1/4 in attached to the top plate. It is separated from the top copper plate by a plastic fitting such that current lines do not pass through the plate. The bottom plate is mated to a copper rod connected to the power supply: with the high conductivity of copper, the entire bottom plate forms the positive electrode. With a diameter ratio between electrodes of $\Gamma_e = 0.06$, a large horizontal divergence in the current lines trigger EVF. Figure 2 shows the locations of UDV probes throughout the system. Positions are limited by the shape of our vessel: each probe requires clearance while the electrode and copper coils on the top plate also occupy space.

Literature predicts that convection and EVF take the form of overturning rolls in the tank. In the former case, flow rises along the centerline and falls along the sidewalls [9] while in the latter, a vertical jet descends along the centerline inducing rising flow along the sidewalls [8]. We therefore place two vertical probes facing down into the fluid layer: one near the center line and one close to the sidewall. Strong horizontal flows should be situated near the top and bottom of the tank, with a transition from positive to negative velocities near the middle. Thus, horizontal radial probes are situated at $z = 0.75H$ and $z = 0.25H$ (and at different angles to account for non-axisymmetric behaviors). Three probes oriented along chord positions ($x = -0.25D, 0.25D$) at different heights are used to detect azimuthal flows, which are known to arise in EVF when external magnetic fields are involved.

4. Results

4.1 UDV data

Figure 3a shows a typical Dopplergram from a convection case, absent any imposed current. Instead of a steady flow, an obvious periodic behavior dominates the flow: this can be seen in both the time-dependent, spatially averaged data (Figure 3c) and the fast Fourier transform (FFT) spectrum (Figure 3d). The peak frequency corresponds to a recently-discovered mode known as the 'jump rope vortex,' where the core of the overturning circulation orbits around a horizontal axis [10]. This mode may encourage greater mixing than previously expected in LMBs.

Figure 4 shows several Dopplergrams from EVF cases over a range of S values. Here, the flow clearly undergoes a behavioral transition from stable in Figure 4a to unstable in Figure 4c. In the intermediate range, Figure 4b, a curious transition occurs involving periodic behaviors. Such clear periodicity has not been previously observed in this transition to our knowledge, and further study is warranted.

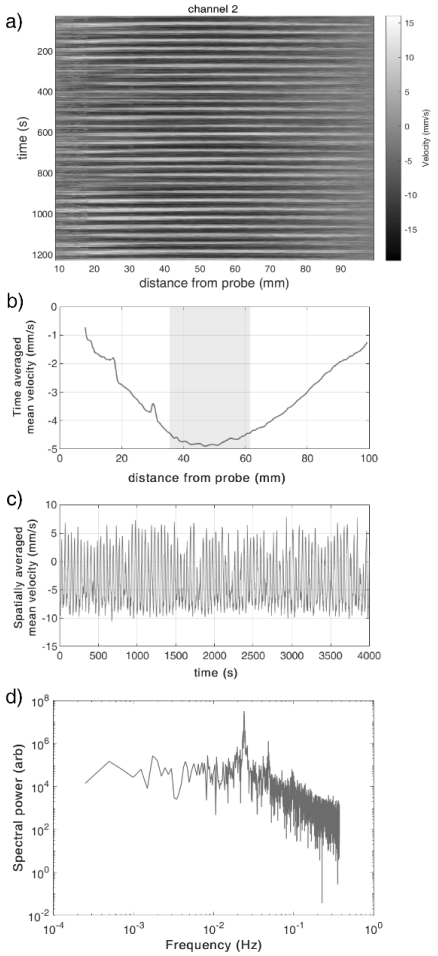

Figure 3: UDV data from convection at $Ra = 2.04 \times 10^5$. Panel a) shows a Dopplergram for probe 2 (see Figure 2): time plotted versus distance from probe with color representing velocity. Panel b) shows the time-averaged velocity versus distance from probe and panel c) the spatially averaged mean velocity versus time. Panel d) shows that the periodic signature visible in a) and c) corresponds to a prominent frequency peak at 0.024 Hz.

4.2 Analysis and postprocessing

Translating UDV results to characteristic velocities and flow structures is nontrivial. Since probes are only positioned in select locations and only detect the component of flow parallel to them, we must ascertain which portion of a UDV Dopplergram – both spatially and temporally – represent characteristic velocities.

In Figure 5, we use several different methods to estimate the Reynolds number from raw UDV data, comparing the resultant Re vs. Ra scaling laws against those in the literature. The caption contains more details on these methods. Although absolute Re values vary, each method still delivers very similar best-fit scalings. They also agree closely with theoretical scaling laws from Ahlers *et al.* [11], who predict $Re \propto Ra^{0.4}$ for these parameter ranges.

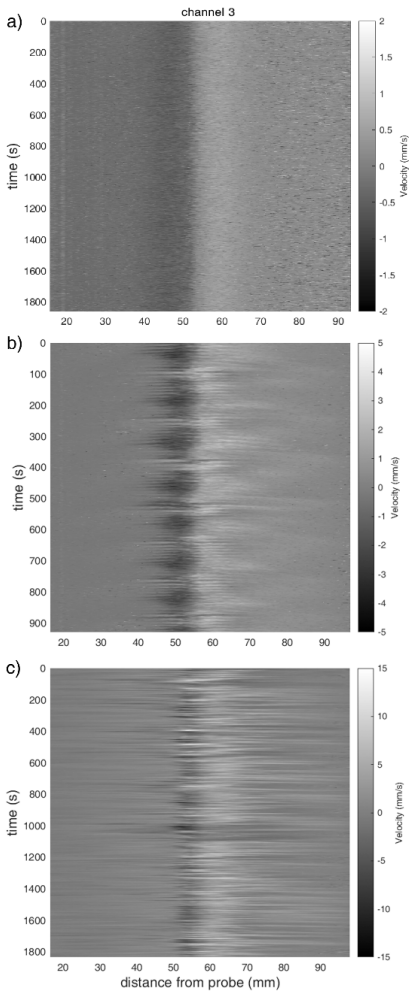

Figure 4: UDV Dopplergrams of probe 3 (see Figure 2) in electrovortex flow cases, at a) $S = 1.05 \times 10^3$, b) $S = 9.47 \times 10^3$, c) $S = 6.74 \times 10^4$. As S increases the flow transitions from stable to periodic to unstable.

Large spatial data gaps are inevitable with UDV. We are exploring the viability of using Physics-Informed Neural Network (PINN) to fill in these data gaps in a reliable way. PINNs are a machine learning tool that takes into account not only the input data but also how well results match the governing equations of motion. This allows the neural network to make an educated guess at the morphology and velocity of flow between different probe lines.

5. Summary

In this work we have shown that UDV is an effective technique for determining the flows occurring in LMBs, eventually helping to predict how flows will affect batteries in an industrial setting. Convective signals manifest a periodic signature of the recently discovered jump-rope vortex, and velocity estimates from UDV show strong agreement with previous studies and theoretical

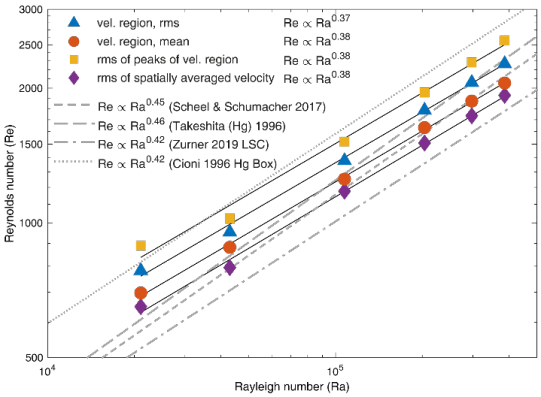

Figure 5: Re vs. Ra data plotted for several different methods of estimating typical velocities from UDV data. Triangles, circles, and squares only take into account the 'velocity region,' where the flow is likely parallel to the UDV probe direction (see highlighted region in Figure 3b). Triangles use the root mean square velocity over all time, circles take the mean over all time, and squares only consider times when the velocity magnitude is near its peak. Finally, diamonds consider the velocities over the region. Data between all probes are averaged in each case. Previous measurements from the literature are plotted in gray.

predictions. EVF undergoes behavioral transitions as the imposed current is varied, showing stable and unstable regimes with periodic behaviors at the transition. PINNs are a promising, if nascent, approach to filling in the necessarily large spatial gaps characteristic of UDV data.

References

[1] https://www.eia.gov/todayinenergy/detail.php?id=42915
[2] Kim H, *et al.*: Liquid metal batteries: past, present, and future, Chem. Rev. 113.3 (2013), 2075-2099.
[3] Kelley DH, & Weier T: Fluid mechanics of liquid metal batteries, App. Mech. Rev. 70.2 (2018).
[4] Weber N, *et al.*: Electromagnetically driven convection suitable for mass transfer enhancement in liquid metal batteries, Appl. Therm. Eng. 143 (2018), 293-301.
[5] Shen Y & Zikanov O: Thermal convection in a liquid metal battery, Theor. Comput. Fluid Dyn. 30.4 (2016), 275-294.
[6] Personnettaz P, *et al.*: Mass transport induced asymmetry in charge/discharge behavior of liquid metal batteries, Electrochem. Comm. 105 (2019), 106496.
[7] Lundquist S: Hydromagnetic viscous flow generated by a diverging electric current, Ark. Fys. 40 (1969), 89-95.
[8] Davidson PA: An Introduction to Magnetohydrodynamics, Cambridge University Press, Cambridge (2002).
[9] Ashour RF, *et al.*: Competing forces in liquid metal electrodes and batteries, J. of Power Sources 378 (2018), 301-310.
[10] Vogt T, *et al.*: Jump rope vortex in liquid metal convection, Proc. Natl. Acad. Sci., 115.50 (2018), 12674-12679.
[11] Ahlers G, *et al.*: Heat transfer and large scale dynamics in turbulent Rayleigh-Bénard convection, Rev. Mod. Phys. 81.2 (2009), 503.

3 Extending Nyquist limit by velocity difference dealiasing rules using a triple PRT

13th International Symposium on Ultrasonic Doppler Methods for Fluid Mechanics and Fluid Engineering
Zürich, Switzerland (13.-15. June 2021)

Extending Nyquist limit by velocity difference dealiasing rules using a triple PRT scheme

Fabio Rizental Coutinho[1], Cesar Yutaka Ofuchi[2], Suzana Lais Silva de Souza[1], Andre Luis Stakowian[2], Marco Jose da Silva[2], Rigoberto Eleazar Melgarejo Morales[4] and Flavio Neves Jr[2]

[1] Dep. of Electronics Engineering, Federal University of Technology – Paraná (UTFPR), R. Cristo Rei 19, Toledo, 85902-490 Brazil
[2] Graduate School of Electrical Engineering and Computer Science (CPGEI), Federal University. of Technology - Paraná (UTFPR), Av. 7 de Setembro 3165, Curitiba, 80230-901, Paraná, Brazil
[3] Mechanical & Materials Engineering Postgraduate Program (PPGEM), Federal University of Technology - Paraná (UTFPR), Av. 7 de Setembro 3165, 80230-901, Curitiba, Paraná, Brazil

The staggered trigger technique consists of using non-uniform Pulse Repetition Times (PRT) to mitigate the range-velocity ambiguity. In a triple PRT technique, three different flow velocities are estimated for each PRT. The velocity difference between these three velocities is used to estimate in which Nyquist interval is the real flow velocity. In this work, a triple PRT method is applied to a rotating cylinder flow experiment. By using a PRT scheme 2/3-3/4, where pulse emission occurs as a two, three, and four times a base period, we demonstrate that this method achieves 6 times the maximum conventional velocity. The number of cycles emitted for the triple PRF was studied. For the experimental conditions set, a 6-cycle burst guarantees an accurate velocity estimation. A theoretical relation between Signal to Noise Ratio (SNR) of the signal received and the number of cycles emitted is presented.

Keywords: Staggered trigger, Doppler technique, triple PRF

1. Introduction

The Doppler method consists of estimating a spatial velocity profile of a liquid flow through the echoes of a pulsed ultrasonic transducer [1]. It generally uses a phase-shift or autocorrelation algorithm to extract the velocity from the signal received [2]. This technique has a limitation on the maximum velocity that can be measured. Whenever flow velocity surpasses this limit velocity aliasing occurs [1]. Reducing the period between ultrasound emissions can extend the velocity limit of the technique, however with a proportional reduction in the maximum distance that can be measured. Several dealiasing techniques were proposed to overcome this issue. A multifrequency arrange [3-5], is based on using two ultrasonic transducers of different resonant frequencies to increase the velocity limit. Another approach is based on using a different algorithm for estimating the velocity. The cross-correlation method [6], the extended autocorrelation method [7], and the velocity matched spectrum analysis [8] use different mathematical approaches to estimating velocity that can increase maximum velocity compared to the conventional phase-shift estimator. However, these advanced velocity estimators are computationally more intensive [9,10].

Velocity dealiasing can also be achieved by using a non-uniform period between ultrasound pulses. With this approach, up to 6 times, the conventional velocity could be attained. Thus, it allows measuring large velocities in long-range measurements. Also, since this method uses a long period between ultrasound emissions it will imply in fewer data to process and less complex acquisition hardware. Staggered PRT (Pulse Repetition Time) or dual PRT is characterized by alternating the period between ultrasonic bursts. The first works using this concept were applied for blood flow [11] and after for weather radar [12,13]. The first industrial flow application of the staggered PRT was reported in [13-14]. Velocity estimation was done by an algorithm denominated as a feedback method. They reported that this technique can measure up to 5 times greater than Nyquist limit. A different form of deciding the aliasing factor for the staggered PRT was proposed in [15]. They used the velocity difference from the velocities estimated for each PRT to decide the dealiasing factor. This work was focused on weather radar application and showed that it could reach up to 2 times the maximum conventional velocity regarding the short PRT period. We have adapted the method of [15] and applied it to fluid engineering [16-17]. Simulation results of [16] showed that the technique can reach velocities higher than described in [15] and with low temporal resolution than [14]. However, experimental results of [17] showed that with a 1-cycle ultrasound pulse emission the maximum velocity was limited to 2 times the maximum conventional velocity regarding the short PRT period. More recently, the work of [18] showed that the staggered method can be further extended to a multiple PRT. Their application was focused on medical imaging systems. They reported measuring up to 6 times the Nyquist limit by using a 2/3-3/4 multiple PRT or triple PRT. This was reached using a 6-cycle ultrasound pulse and they also reported a low temporal resolution.

Triple PRT or dual PRT can also be used to extend the maximum distance measured in applications which velocity aliasing is not an issue. A conventional uniform PRT using a phase-shift estimator can be converted to a dual or Triple-PRT by dropping lines of emissions. Increasing the period between emissions implies in a large range of distance measured. For a triple PRT, an increase

of 6 times in distance can be attained. Another benefit in this approach, is the reduction of data processing. As an example, a minimum of 6 lines of emissions can be dropped in comparison with the uniform period of emissions. This also implies in using pulse repetition frequency (PRF) roughly 1/6 compared to the uniform period of emissions. Also, reducing the PRF enables the use of a higher voltage pulses for excitation, since transducer dissipation power is proportional to the PRF used.

Inspired by the work of [18] we adapted the triple PRT for industrial application. Using a classical rotating cylinder flow we have assessed the accuracy of this technique. Several numbers of ultrasonics burst cycles were tested to find the appropriate ultrasonic excitation scheme for this technique. We finish, showing a theoretical relation for the technique based on the SNR ratio.

2. Triple PRT method

The base principle of the triple method is to alternate PRT between 3 different periods: T_1, T_2 and T_3, where $T_1/T_2 = m/n$ and $T_1/T_3 = n/p$ and m, n and p are positive integers relatively prime. For this work, $m = 2$, $n = 3$, and $p = 4$, also referred to as 2/3-3/4 scheme. The autocorrelation method is applied three times for each PRT resulting in three velocities estimated v_1, v_2 and v_3 (Figure 1). As in the conventional phase-shift method these three velocities are limited to [1]

$$v_{a1} = \frac{c}{4T_1 f_c}, \tag{1}$$

$$v_{a2} = \frac{c}{4T_2 f_c}, \tag{2}$$

$$v_{a3} = \frac{c}{4T_3 f_c}, \tag{3}$$

also known as Nyquist limit, where c is the sound velocity of the medium and f_c is the transducer central frequency. Each time flow velocity surpasses one of these limits the correspondent estimated velocity will be aliased. The velocity difference $v_{21} = v_2 - v_1$ and $v_{31} = v_3 - v_1$ are used as inputs to a set of dealiasing rules. They are arranged in a lookup table that will result in the aliasing factor n_1, n_2 and n_3 [20]. And the velocities are dealiased by the following relation

$$v_{1d} = v_1 + 2n_1 v_{a1}, \tag{4}$$

$$v_{2d} = v_2 + 2n_2 v_{a2}, \tag{5}$$

$$v_{3d} = v_3 + 2n_3 v_{a3}. \tag{6}$$

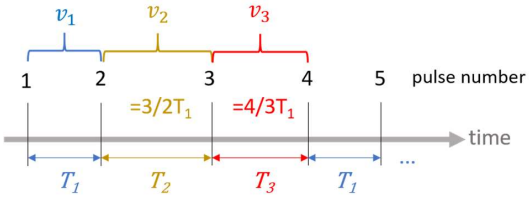

Figure 1: Triple PRT pulsing scheme.

If the technique were a dual PRT, the maximum dealiased velocity measured would be $2v_{a1}$ and $3v_{a1}$, for $T_1/T_2 = 2/3$ and $T_1/T_3 = 3/4$, respectively. However, the combination of the inputs v_{21} and v_{31} is used to increase the maximum dealiased velocity. For $m = 2$, $n = 3$, and $p = 4$ the maximum velocity regarding v_{a1} is least common multiple between m, n, or $6v_{a1}$ [18].

2.1 Minimum SNR

According to [18] the maximum allowable error of velocity estimates for a 2/3-3/4 triple scheme is given by

$$|e_{\max}| = \frac{v_{a1}}{\sqrt{12} + 4}. \tag{7}$$

In [21] it was derived a relationship between SNR and frequency standard deviation for the autocorrelation algorithm as

$$SNR = \frac{1}{\sqrt{2x^2 e^{-x^2}\left(\frac{N\sigma^2}{F_\sigma^2}\right) + e^{-x^2} - 1}} \tag{8}$$

Where it was assumed that the spectrum of the signal is Gaussian in shape, F_σ is the frequency spread, N denote the number of lines used for estimation, and $x = 2\pi F_\sigma T$ and T is the period between emissions. This equation was derived for the conventional autocorrelation method. However, triple PRT estimation can be treated as three different autocorrelation estimators, each one with its own period between emissions.

Let us assume that this standard deviation, σ, will result in the error in the triple PRT, thus $\sigma \leq |e_{\max}|$, and Eq. (8 becomes

$$SNR = \frac{1}{\sqrt{2x^2 e^{-x^2}\left(\frac{4f_c^2 N e_{\max}{}^2}{c^2 F_\sigma^2}\right) + e^{-x^2} - 1}}, \tag{9}$$

where $(2f_c/c)^2$ was added to translate the maximum velocity error in a maximum Doppler frequency error, f_c is the transducer central frequency and c is the sound velocity.

3. Measurement Method

A cylinder, submerged in a water tank, was filled with 1.8

L of a density match solution (water and glycerol). A 0.5 g of trace powder (EMS GRILTECH 1A P82) with 1.07 g/cm^3 was added to the solution. A 4 MHz ultrasonic transducer (Met-flow) was positioned at 31.5 mm from the central axis (Figure 2). This set-up is a classical rotating cylinder flow with a uniform spatial velocity profile [1].

Cylinder reference velocity is measured by an encoder. Ultrasound emission and acquisition are sampled at 40 MHz by proprietary hardware. Data acquired is processed offline by a personal computer.

Transducer emissions of 2,4,6 and 8-cycles bursts were used in the experiment. For each condition, 18 different angular velocities, ranging from 0.73 to 9.3 rad/s (7 to 89 RPM) were tested. A total of 2 seconds of data was acquired for each velocity. The PRT was set to 2,25 ms (T_1), 3.375 ms (T_2) and 3 ms (T_3) resulting in a PRT ratio of $T_1/T_2 = 2/3$ and $T_1/T_3 = 3/4$. In this condition, the conventional maximum velocities are $v_{a1} = 47.5\ mm/s$ or 14.4 RPM, $v_{a2} = 31.7\ mm/s$ or 9.6 RPM and $v_{a3} = 35.6\ mm/s$ or 10.8 RPM.

Due to the nonuniform pulse repetition period used, the data were filtered to remove stationary echoes using a second-order polynomial regression filter (length M_f=20) [20]. Velocities data were calculated for every 51 emissions resulting in a temporal resolution of 0.144 s. Since velocity is estimated for each PRT, the three velocities are estimated using only 17 pulse emissions each. The spatiotemporal velocity maps were post-processed using a median filter with 3x3 matrix size. Range gate length was set as $4N_{cycle}\lambda$, where N_{cycle} is the number of cycles burst and λ is the wavelength.

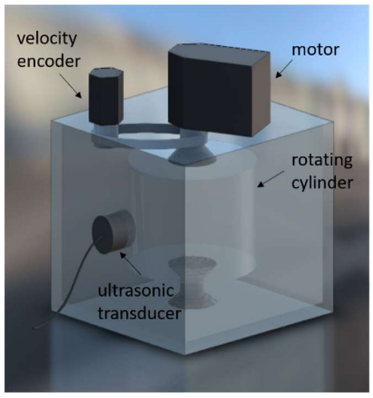

Figure 2: Rotating cylinder flow experimental set-up.

4. Results

The triple PRT overall performance was evaluated by the mean value of the spatial velocity profile (Figure 3). This result was computed for cylinder velocities varying from $0.49v_{a1}$ up to from $6.2v_{a1}$ (approximately 7 RPM up to 89 RPM). The PRT ratio of 2/3/4 has a theoretical limit of $6\,v_{a1}$. Measurements were done using a 6-cycle burst emission. It can be noticed that the technique can estimate the cylinder velocity with less than 5% of error up to the theoretical velocity limit ($6v_{a1}$).

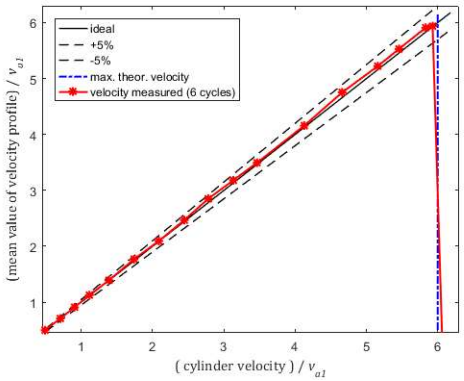

Figure 3: Normalized spatial mean velocity measured versus normalized cylinder reference velocity for a 6-cycle ultrasound emission.

The accumulated root mean square error for the spatiotemporal velocity map was computed for 2,4,6 and 8-cycles. This analysis aimed to evaluate the accuracy of each burst emission (Figure 4). The 2-cycles burst presented a poor result, therefore is not recommended for the 2/3-3/4 technique. The 4,6 and 8-cycles emission presented a similar result, but for velocities in the vicinity of $6v_{a1}$ the 4-cycles emission results in a high RMSE value of 145 mm/s meanwhile the 6-cycles and 8 cycles bursts result in RMSE of 31 mm/s and 38 mm/s, respectively.

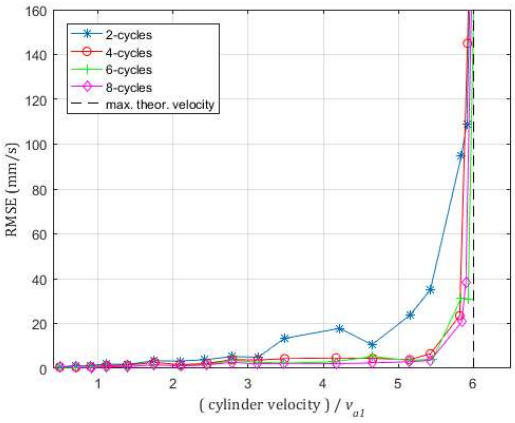

Figure 4: Global root-mean-square error as function of normalized cylinder velocity for 2,4,6 and 8-cycle ultrasound emission.

4.1 SNR Results

Eq. (9) was applied for the experimental setup proposed. It was considered the worst-case scenario, which was $T = T_1 = 2.25\ ms$. Frequency spread was obtained by [1]

$$F_\sigma = \frac{2f_c v_{a1}}{N_{cycles}}c, \qquad (3)$$

where f_c is the transducer central frequency and N_{cycles} is

the number of ultrasound pulses. The number of lines used was $N = 17$. Figure 5 show the results of the dependency of the SNR as the number of cycles are increased. From 2-cycles to 6-cycles burst the SNR decreases 11.7 dB. As the number of cycles increases the spectrum´s frequency spread decreases (Eq. (3)). Narrowing the Doppler spectrum implies in more accurate frequency estimate (or velocity estimate) and a smaller frequency standard deviation value. It explains why the number of cycles influence in the technique accuracy. Fig. 5 also serves as a specification for experimental setup. It should be observed that it is neglected that the increase in the N_{cycles} could also increase the signal power thus increasing SNR.

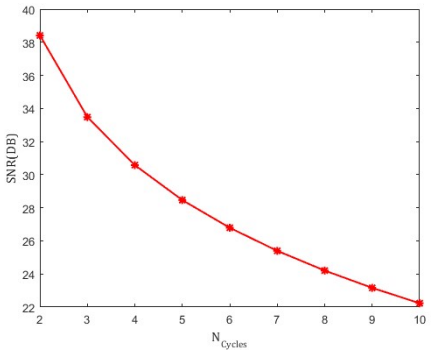

Figure 5: SNR relationship with the number of emitted cycles.

5. Summary

The triple PRT technique 2/3-3/4 implemented showed that it can measure velocities up to 6 times the Nyquist limit. To reach this same result with a dual PRT, it would be necessary to use a PRT ratio of $T_1/T_2 = 6/7$. At this ratio, the relative mean square error increases significantly [18].

The number of ultrasonics cycles emitted was studied. For the experiment described, a 6-cycles ultrasound emission should be used to guarantee accurate measurement in the vicinity of Nyquist limit. It should be noted that the increase of the ultrasound burst will directly increase the spatial resolution of the velocity profile.

A theoretical equation for the SNR was presented. It shows the relation of the SNR with the number of cycles emitted. This relationship could be studied further using simulated ultrasound signals where is possible to have accurate SNR values. In typical applications of Doppler technique, the margin for increases SNR ratio is the use of a higher pulse voltage excitation or increasing the number of cycles emitted.

6. Future work

We plan to conduct additional studies using simulation of ultrasound signals to fully understand the relationship between SNR and the number of pulses emitted.

The triple PRT code will be adapted to Python language and will be available for free as a Python library at https://github.com/cesarofuchi/pyuvp.

References

[1] Takeda Y: Ultrasonic Doppler fluid flow, Springer, (2012).
[2] Namekawa K, *et al*.: Realtime bloodflow imaging system utilizing autocorrelation techniques. In: Lerski RA Morley P (eds) Ultrasound '82, pp 203-208, Pergamon, New York (1982).
[3] Fer R, *et al*.: New Advances in colour flow mapping: quantitative velocity measurement beyond Nyquist limit. Br J Radio 64 (1991), 651.
[4] Nitzpon HJ, *et al*.: A new pulsed wave Doppler ultrasound system to measure blod velocities beyond Niquist limit. IEEE Trans Ultrason. Ferrroelec. Freq. Contr. 42 (1995), 265-279.
[5] Zedel L & Hay AE: Design and performance of a new Multi-frequency coherent Doppler profiler. 33rd IAHR Congress, 2009.
[6] Jensen, JA: Estimation of blood velocities using ultrasound: A signal processing approach. Cambridge Univ. Press, (2006).
[7] Lai X & Torp H: An Extended Autocorrelation Method for Estimation of Blood Velocity, IEEE Trans. Ultrason., Ferroelec., Freq. Contr. 44 (2007), 1332-1342.
[8] Torp H & Kristoffersen K: Velocity matched spectrum analysis: a new method for suppressing velocity ambiguity in pulsed-wave Doppler. Ultrasound Med. Biol. 21(1995), 937-944.
[9] Ofuchi, CY, *et al*.: Extended autocorrelation velocity estimator applied to fluid engineering, Proc. of the 9th ISUD, Strasbourg (2014), 109-112.
[10] Ofuchi C. Y. et al. Evaluation of an extended autocorrelation phase estimator for ultrasonic velocity profiles using nondestructive testing systems. Sensors. 16 (2016), 1250.
[11] Nishiyama H & Katakura K. Non-equally-spaced pulse transmission for non-aliasing ultrasonic pulsed Doppler measurement, J. Acoust. Soc. Jpn. 13, 4 (1992), 215-222.
[12] Franca MJ & Lemmin U: Eliminating velocity aliasing in acoustic Doppler velocity profiler data, Meas. Sci. Tech. 17 (2006), 313-322.
[13] Holleman I & Beekhuis H: Analysis and Correction of Dual PRF Velocity Data, J. Atmos. Ocean. Tech. 20 (2003), 443-453.
[13] Murakawa H, *et al*.: Higher flowrate measurement using ultrasonic pulsed Doppler method with staggered trigger. Proc. of ISUD9, Strasbourg (2014), 117-120.
[14] Murakawa H, *et al*.: A dealiasing method for use with ultrasonic pulsed Doppler in measuring velocity profiles and flow rates in pipes. Meas. Sc. Tech, 26,8 (2015).
[15] Torres S M & Dubel Y: Design, implementation, and demonstration of a staggered PRT algorithm for the WSR-88D. J. Atmos. Oceanic Tech. 21 (2004), 1389-1399.
[16] Coutinho, F R Implementation of a staggered trigger algorithm by velocity difference dealiasing rules. Proc. of ISUD10, Tokyo (2016), 45-48.
[17] Coutinho, F R, *et al*.: Implementation of a staggered trigger algorithm by velocity difference dealiasing rules: experimental results. Proc. of ISUD11, Berlin (2018).
[18] Posada D, *et al*.: Staggered multiple-PRF ultrafast color Doppler. IEE Trans. On Med. Imag., 35, 6, 1510-21 (2016).
[19] Posada D. Ultrafast echocardiography. Master´s Thesis. Biomedical Engineering Dep, University of Montréal (2015).
[20] Torres S M & Zrnic D S. Ground clutter cancelling with a regression filter. J. Atmos. Ocean. Tech. 16 (1999), 1364-1372.
[21] Loupas T & Powers JT. An Axial Velocity Estimator for Ultrasound Blood Flow Imaging, Based on a Full Evaluation of the Doppler Equation by Means of a Two-Dimensional Autocorrelation Approach. IEEE Trans. Ultrason. Ferroelectr. Freq. Contr. 42, 4, (1995), 672-88.

4 In situ ultrasonic measurement of the local liquid fraction of froth flotation processes

13th International Symposium on Ultrasonic Doppler Methods for Fluid Mechanics and Fluid Engineering
Zürich, Switzerland (13.-15. June 2021)

In situ ultrasonic measurement of the local liquid fraction of froth for flotation processes

Hannes Emmerich[1], Richard Nauber[2], Lars Büttner[1], Leon Knüpfer[3], Sascha Heitkam[3] and Jürgen Czarske[1]

[1] Lab. of Measurement and Sensor System Techniques, Technische Universität (TU) Dresden, 01069 Dresden, Germany
[2] Institute for Integrative Nanosciences, Leibnitz-Institute for Solid State and Materials Research Dresden, 01069 Dresden, Germany
[3] Institute of Fluid Dynamics, Helmholtz-Zentrum Dresden-Rossendorf, 01328 Dresden, Germany

Receiving in situ information of multi-phase mixtures is an ongoing interest of the industry to optimize processes. Controlling process parameters in froth flotation, as the liquid fraction or the bubble size, opens up potential to save resources, to reduce energy consumption and to increase the process yield and grade. Using ultrasound in the low kilohertz range, we are able to receive backscattered ultrasound signals from the inside of froth. Based on these echo signals and the assumption that Plateau borders cause the backscattering, we employ an one dimensional model of the sound propagation through the foam. Regarding dry foam (liquid fraction < 0.8 %) the calculated backscattering coefficient shows a proportional relation to the liquid fraction and increases with rising liquid fraction. By time gating the echo signal, we achieve an axial spatial resolution of 3.9 mm with a measurement uncertainty of σ_Φ = 0.094 %. With these measurements for calibration, we demonstrated a time-resolved measurement of a sudden change of the liquid fraction. We therefore demonstrated a first possible approach to gather in situ information of foam's liquid fraction and set up the way for mass flow measurements in strongly attenuating suspensions with possible applications in froth flotation.

Keywords: Froth, In situ, Liquid fraction, Backscattering coefficient

1. Introduction

To extract copper minerals from ore it is grinded to particles and put in a flotation cell. Surfactant containing solutions selectively render the mineral particles hydrophobic. Thus they attach to rising bubbles and move to the top-lying froth overflowing the vessel and extracting the mineral in high purity.

44 million tons of water are used every year in only one conventional froth flotation circuit for copper [1]. Regarding this massive amount of resources needed to carry out this process, a closed loop-control is essential for a potential save of resources, energy and an increase of the yield.

However, gathering in situ information of strongly damping materials is a metrological challenge. Optical measurements hardly enter the inner of a multiple phase solution as froth [2]. The same problem occurs with high frequency ultrasound. Especially suspension like compounds as water air mixtures additionally cause a high acoustic impedance jump and a lot of scatter. However, using ultrasound in the low kilohertz range enables a penetration of some centimeters into the froth [3]. Parameters such as bubble size, liquid fraction Φ and particle flow could be controlled, if one is able to measure them in situ with a robust measurement system. We therefore investigate the possible deduction of the local liquid fraction Φ from ultrasound backscattering for dry foam (Φ < 0.8 %).

2. Experimental setup

A scheme of the experimental setup, seen in Figure 1, illustrates the build of an acrylic glass cylinder. The liquid at the bottom consists of deionized water with additional 10 g/l sodium dodecyl sulfate (SDS) and 0.75 g/l potassium chloride (KCl). Air enters the cylinder with a constant flow rate through a drilled smaller tube at the bottom. The tenside solution foams up until the acrylic cylinder is filled up completely. The airflow is then terminated. The determined bubble diameter amounts to 2 ±1.7 mm. During that time a double syringe pump (Harvard Apparatus - Model 33) pumps up the tenside solution from the bottom of the cylinder to a sprinkler at the top with a volume flow of 20 ml/min. The water enters the foam and drains downward, yielding a steady and homogeneous liquid fraction distribution [4]. After three minutes, the liquid flow rate is turned off as well and the foam begins to dry. Now the measurement is started, observing the drying phase of the foam.

Two ultrasound transducers (multicomp-MCUSD19A175B11.5RS) are mounted at the same height of the cylinder, with direct contact to the foam. Due to a long ringing of the emitting transducer, a second transducer had to be used for receiving. The transducers with a diameter of 19 mm and a center frequency of 175 kHz have been used to send/ receive a logarithmic chirp from 165…185 kHz. An in house developed generic ultrasound research platform "Phased array Doppler velocimeter" (PAUDV) [5] was used for the electrical activation and data acquisition (see Table 1).

Two electrodes, connected to a digital oscilloscope (PicoScope) are covered in foam and measure the reference liquid fraction according to Feitosa et al. [6] via an electrical impedance measurement. The electrodes are one resistor in a voltage divider, whereas the other resistor is constant and has 1 kΩ.

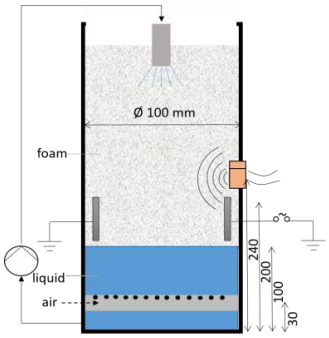

Figure 1: Scheme of experimental setup to determine a local liquid fraction in foam with ultrasonic echo measurements.

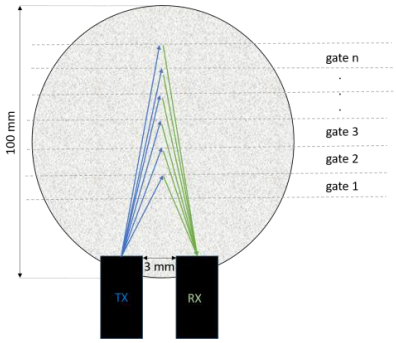

Figure 2: Scheme of the time gated equivalent spatial gates for a local liquid fraction measurement with two ultrasound transducers.

Table 1: Parameter of data acquisition

pulse repetition frequency	50 Hz
number of pulses to average	10
measurement frequency of impedance reference	0.33 Hz
sample frequency	5 MHz

3. Calibration measurement

The drying foam was measured not longer than 5 minutes to prevent bubble coarsening [7] and the measurement was repeated four times. An approximate liquid fraction range from 0.1 % < Φ < 0.8 % is achieved. Acquired echo data could only be investigated between 300…437.4 µs after the transducer excitation. Talk-over, transducer ringing and backwall echo of the cylinder, therefore minimize the regarded spatial area to 23.7 mm close to the backwall. The received signal is transformed into an analytical signal by Hilbert transformation and the envelope is time-gated to achieve a spatial resolution. As foam is holding the liquid in the Plateau borders and vertices between the bubbles we aim at a local resolution of about twice the bubble diameter (e.g. ~ 4 mm). To achieve the highest possible spatial resolution, the analyzed part of the signal has been divided into 6 equally sized time gates. This equals λ/4 of the whole sent pulse and corresponds to a spatial resolution of 3.9 mm (regarding the speed of sound in air $c_{air} = 345\ m/s$). A general scheme to illustrate the spatial equivalent to the time gates is shown in Figure 2.

The backscattering coefficient r_n can be determined by Equation 1 and 2, where RX_n is the integrated amplitude envelope for the specific time gate n and I_0 is the total backscattered energy after talk-over and transducer ringing.

$$r_0 = \frac{RX_0}{I_0} \tag{1}$$

$$r_n = \frac{RX_n}{I_0 \prod_{i=1}^{n}(1 - r_{i-1})^2} \tag{2}$$

Two of 2400 backscattering coefficients exceeded the maximal physically possible backscattering coefficient of r = 1 (total reflection) and therefore have been set to one. Regarding all backscattering coefficients r_n for the drying foam, a linear regression has been derived to show the dependency of the backscattering coefficient r_n on the liquid fraction Φ. Figure 3 illustrates this dependency. A proportional relation is visible, where the backscattering coefficient increases for a rising liquid fraction. Presumably, thicker Plateau borders increase the amount of backscattered energy and hypothetically establish our physical effect. These measurements are used to calibrate the measurement system. The deviation of the backscattering coefficient increases for higher liquid fractions and penetration depth.

The residuals between the predicted and the actual liquid fraction serve to calculate the measurement uncertainty according to the *Guide to the Expression of Uncertainty in Measurement* (GUM [8]) considering the unknown systematic and the random error and add up to σ_Φ = 0.094 %.

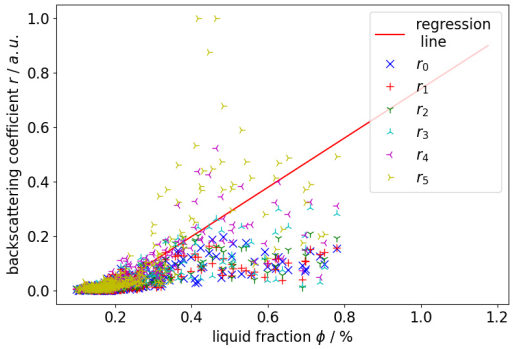

Figure 3: Backscattering coefficients r of the six time gates of the analyzed echo signal over a varying liquid fraction during a drying process of foam. Presumably a higher attenuation for a higher liquid fraction leads to an increased deviation in the section Φ > 0.4 %.

4. Results of model experiment

As a validation of our measurement system, we conducted a model experiment with a sudden change of liquid fraction. Therefore, the sprinkler was pulled of its hose and the loose end of the hose was attached in the foam to the backwall of the cylinder, 5 cm above the transducer height. Approx. 23 s after the measurement started, the tenside liquid was pumped from the bottom of the acrylic cylinder towards the loose end of the hose and therefore to the backwall of the cylinder, with a volume flow of 60 ml/min. Due to capillary pressure, this liquid does not accumulate at the wall but is sucked into the foam near the wall. This forms a wetting front that moves downward through the foam.

Figure 4 displays the temporal change of the liquid fraction in the different gates. Backscattering coefficients exceeding the calibration range have been excluded as outliers. After approximately 30 seconds the wetting front reaches the measurement position and the liquid fraction in all measurement positions increases. With gate 6 as the closest gate to the backwall of the cylinder (epicenter of the change of the liquid fraction) and gate 1 as the closest gate to the transducers, a significant higher increase of the liquid fraction in the gates closer to the backwall is observed.

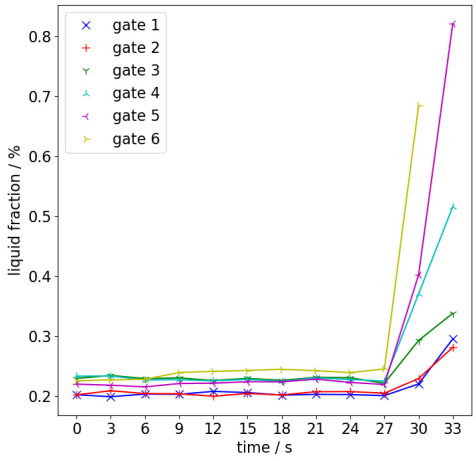

Figure 4: Model experiment: Sudden local change of liquid fraction allows a spatio-temporally resolution and validates the measurement system.

5. Summary

Drying foam has been analyzed by the means of ultrasound echo measurements and a calibration of the measurement system has been achieved with a measurement uncertainty less than 0.1 % (σ_Φ= 0.094 %). A model experiment with a sudden local change of liquid fraction has been conducted to validate our measurement system. We therefore showed a spatially and temporally resolved measurement of the liquid fraction in foam. Future work aims to decrease the deviation for higher liquid fractions by the use of transducers, that introduce more energy into the medium. Additionally, Doppler measurements will be conducted to build up the mass flow measurement. A local reference for the local liquid fraction will be derived by neutron imaging [9].

Funding: The IGF project No. 21151 BR of the research association DECHEMA, Gesellschaft für Chemische Technik und Biotechnologie e.V., Theodor-Heuss-Allee 25, 60486 Frankfurt am Main, Germany, was funded by the German Federal Ministry for Economic Affairs and Energy through the German Federation of Industrial Research Associations (AiF) within the framework of the program for the promotion of joint industrial research (IGF) on the basis of a resolution of the German Bundestag.

Acknowledgements: David Weik is thanked for helpful comments and valuable discussions.

References

[1] D. Bleiwas, “Estimated water requirements for the conventional flotation of copper ores,”U.S. Geological SurveyOpen-File Report, 201

[2] M. Vera, A. Saint-Jalmes, and D. Durian, “Scattering optics of foam,” Applied optics, vol. 40, pp. 4210–4, 09 2001.

[3] R. Nauber, L. Büttner, K. Eckert, J. Fröhlich, J. Czarske, and S. Heitkam, “Ultrasonic measurements of the bulk flow field in foams,” Phys. Rev. E, vol. 97, p. 013113, Jan 2018.

[4] S. Heitkam and K. Eckert, “Convective instability in sheared foam,” Journal of Fluid Mechanics, vol. 911, p. A54, 2021.

[5] K. Mäder, R. Nauber, V. Galindo, H. Beyer, L. Büttner, S. Eckert, and J. Czarske, “Phased array ultrasound system for planar flow mapping in liquid metals,” IEEE Transactions on Ultrasonics, Ferroelectrics, and Frequency Control, vol. 64, no. 9, pp. 1327–1335, 2017.

[6] K. Feitosa, S. Marze, A. Saint-Jalmes, and D. J. Durian,“Electrical conductivity of dispersions: From dry foams todilute suspensions,”Journal of Physics Condensed Matter,vol. 17, no. 41, pp. 6301–6305, 2005.

[7] I. Ben Salem, R.-M. Guillermic, C. Sample, V. Leroy, A. Saint-Jalmes, and B. Dollet, “Propagation of ultrasound in aqueous foams: Bubble size dependence and resonance effects,” Soft Matter, vol. 9, pp. 1194–1202, 12 2012.

[8] “Evaluation of measurement data — Guide to the expression of uncertainty in measurement”, Working Group 1 of the Joint Committee for Guides in Metrology (JCGM/WG 1), JCGM 100:2008, GUM 1995 with minor corrections

[9] S. Heitkam, M. Rudolph, T. Lappan, M. Sarma, S. Eckert,P. Trtik, E. Lehmann, P. Vontobel, and K. Eckert, “Neutronimaging of froth structure and particle motion,”MineralsEngineering, vol. 119, pp. 126–129, 2

5 Investigation and comparison of fluid dynamics in a hydrocyclone using ultrasonic doppler velocity profile

13th International Symposium on Ultrasonic Doppler Methods for Fluid Mechanics and Fluid Engineering
Zürich, Switzerland (13.-15. June 2021)

Investigation and comparison of fluid dynamics in a hydrocyclone using ultrasonic doppler velocity profiler

Lucas Grob, Eileen Ott, Liridon Zeneli, Yasushi Takeda, and Erich J. Windhab[1]

[1] Dep. of Health Science and Technology, ETH Zürich, Zürich, Switzerland

Hydrocyclones are widely used in multiple industries for different separation and pre-concentration tasks. Nevertheless the flow within a hydrocyclone remains complex and depending on the throughput and design several different flow regimes can occur. Understanding and measuring the velocity distribution of the flow regimes, without disturbing it, is key to design the process accordingly. In the presented study, a pilot scale hydrocyclone, in bottom-up flow, was investigated for throughput range of 21.3 to 33.8 L/min of deionised water using the ultrasonic doppler method and air bubbles as tracer particles. The radial average velocity and frequency profiles were analysed, mapped and compared to CFD simulations. Additionally, different angles of the ultrasonic transducers positioned within the hydrocyclone were tested. The results of the average velocity indicated alternating motion of the tracer bubbles away and towards the measurement line and agreed well with the simulation. Investigation of the frequency profile further showed that an inner motion at 1.5 Hz and an outer motion at 2.5 Hz were dominant. Decomposition of the spatiotemporal velocity field of vertical measurements revealed a major steady wave of the hydrocyclone and hydrodynamic instabilities at low Re-Numbers. The ultrasonic doppler method proved to be a valuable tool to investigate and characterize the different flow regimes in a hydrocyclone. These findings allow a more precise design and process control of new generation hydrocyclone processes.

Keywords: Hydrocyclone, flow mapping, air bubbles, spatiotemporal velocity field

1. Introduction

Hydrocyclones are a common method to separate solids by size from a liquid phase. The suspension, particles to be separated in a liquid, are tangentially streamed into a cylindrical or conical body. The resulting particle classification is assumed to be from an opposing centrifugal and drag force balance with radial drag of small particles towards the core, throughout the conical section, and centrifugal drift of large particles towards the wall [1]. Therefore, it is recognized that tangential velocity (v) and fluctuations are necessary to know and can occur due to process parameters and design aspects. With increasing throughput, the suspension is further accelerated and observed tangential velocity increases. Similar behavior was reported with a transition from a cylindrical to a conical hydrocyclone body. Moreover, design aspects, such as height to diameter ratio and symmetrical inlets, have been thoroughly researched [2-4] in order to achieve maximized separation efficiency. The flow behavior within remains complex and advanced knowledge of the hydrodynamics are necessary for process efficiency and stability. Early studies [5] have already estimated the flow pattern, using die injection and the mean tangential and axial velocity using laser doppler anemometry. Another proposed method is ultrasound velocity profiling [6]. This method has already been tested as a valuable tool to estimate the tangential flow within a hydrocyclone [7].

Nevertheless, accessing the complex flow field, without disturbing it, in hydrocyclones remains difficult. In this work, an ultrasonic doppler method is presented to determine the complex flow field within a hydrocyclone using bubbles as tracer particles. In a second stage, the results obtained were then compared to simulations. These findings are key for a new separation process design.

2. Materials and Methods

2.1 Hydrocyclone design

A hydrocyclone (HC) was designed according to the design aspects (see Figure 1) and the dimension stated in Table 1. Throughput $\dot{Q}$ was set at 22.1, 23.5, 33.2 and 33.7 L/min. Additionally, an air inlet with a membrane (max. pore size p= 15 µm, d_m= 20 mm) built into the hydrocyclone at a distance of 5.0 cm from the center and a height of 7.0 cm from the bottom. Airflow was set ranging from 0.07 to 150 mL/min.

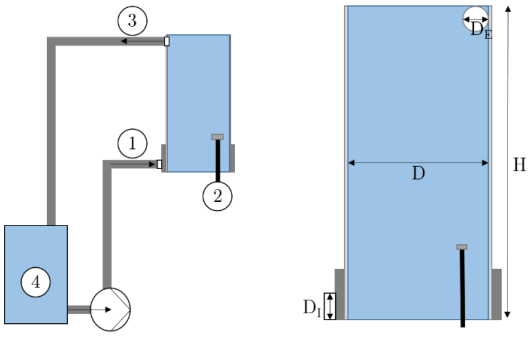

Figure 1: Hydrocyclone design. 1. Inlet, 2. Air inlet, 3. Outlet, and 4. Storage container.

Table 1: Dimensions of hydrocyclone.

D	0.15 m
H	0.895 m
D_I	0.025 m
D_E	0.04 m

2.2 Ultrasonic velocity profiling (UVP) of the hydrocyclone

Ultrasonic velocity profile measurements were carried out with doppler, immersion type 4 MHz, 5 mm active element ultrasonic transducers (TN and TX-line, Imasonic, Bensancon, France) and the UVP-DUO profiler (Met-flow SA, Lausanne, Switzerland). The sound speed was 1480 m/s as the medium was deionized water. For radial measurements, the transducers were positioned every 5 cm starting at 125 mm from the bottom at centerline and 1 cm offset to the centerline of the hydrocyclone (see Fig. 2A). Measurements were performed with a maximal distance of 160 mm and 39 µs. First channel was at 5 mm and a resolution of 0.56 mm/channel. The number of emission/profile was 1024. For angular measurements, the transducer was positioned inside the hydrocyclone at angle α=0°, -30°, -45°and -60°. The sensors were positioned along the x-axis at a height of z=720 mm (Fig. 2B). At last, for vertical measurements, the transducer was positioned inside the center of the hydrocyclone at a height of z=720 mm (Fig. 2C).

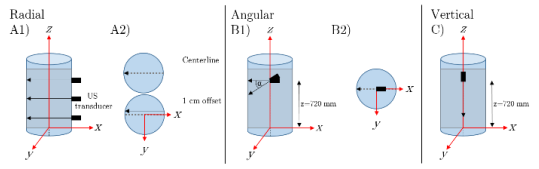

Figure 2: UVP measurement setup for radial, angular, and vertical measurements. A1) side view of HC and attached US transducers. A2) top view centerline and 1 cm offset measurement. B1) side view of HC and US transducer positioned at an angleαand at a height of 720 mm. B2) top view: transducer placed along x-axis. C) side view of vertical placement of sensor at a height of 720 mm.

2.3 Modelling of hydrocyclone

The hydrocyclone was simulated with COMSOL Multiphysics® (Comsol Inc., Burlington MA, USA) simulation software version 5.3. The hydrocyclone was designed according to Table 1. The turbulent flow model with a turbulence intensity of 5% and a turbulence length scale of 1.75 mm were used. A throughput of 33.7 L/min resulting in a normal inlet velocity of 1.14 m/s was set. The walls were treated with a no-slip condition. A maximum mesh size of 0.012 m was applied.

3. Results

3.1 General observations

The hydrocyclone (HC) was operated at different throughput from 22 to 32.7 L/min corresponding to Re-Number from 10^6 to $1.58 \cdot 10^6$ with the inlet diameter D_I as characteristic length. Further, the HC was operated with a bottom-up flow. In contrast to the common hydrocyclone design, where a top down flow is applied and the diameter is decreased, this design purely consists of a cylindrical body. The medium inlet was injected tangentially to the cylindrical body, this led to an upward swirling motion.

Figure 3 shows the motion of bubbles within the presented HC at various throughputs.

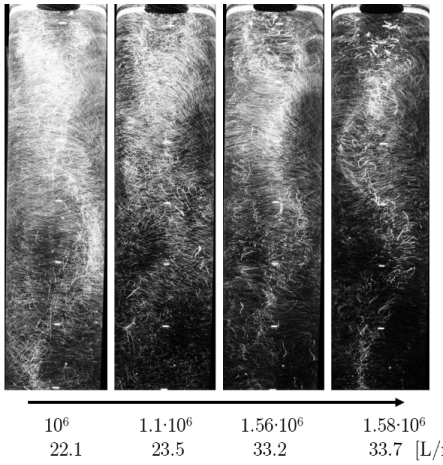

Figure 3: Representative long exposure picture of hydrocyclone operated at different Re-Number/throughput with an air flow set at 150 mL/min.

3.2 Radial velocity distribution

To extract velocity field x-component u, UVP measurements were carried out with the addition of micronized bubbles as tracer particles. The transducers were placed horizontally outside the HC. In Fig.4a), regimes with high velocities $\bar{u}$ (up to 165 mm/s) and low/negative velocities (up to -165 mm/s) showed to be alternating from top to bottom. This suggests that in negative velocity regimes, the bubbles move towards the transducers and to the center. At high velocities the bubbles move away and towards the outer wall. When comparing the UVP data to the simulation, the obtained average velocities $\bar{u}$ from UVP agreed reasonably well with the simulated data (see Fig. 4b)). As the root mean square error was large, further refinement of the data could be carried out in order to achieve a higher degree of validation of the simulation. Further experimental data (not shown here) showed, that the velocity distribution in the x-z plane is independent of the bubble flow for a range of 0.07-150 mL/min of air.

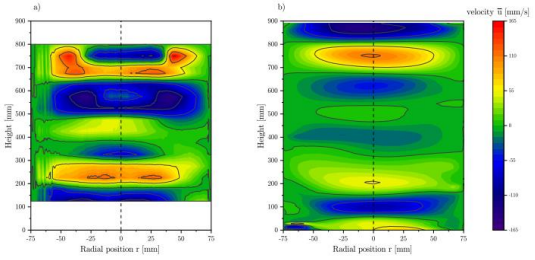

Figure 4: Comparison of average radial velocity a) measured with UVP and b) computed over the height of the hydrocyclone.

3.3 Assessment of the swirling motion

To determine the major swirling motion and frequency, measurements at different angle inclinations from 0° to -

60° were carried out. The obtained frequency spectra were then plotted along the measurement lines in Fig. 5. Two prominent clusters of frequencies could be highlighted. Oscillations at frequencies of 1.5 and 2.5 Hz were clearly visible for all measurement angles. A clear second harmonic oscillation could not be distinguished. When the measurement angles were successively decreased to -60°, oscillations of 1.5 Hz became more prominent, thus this frequency corresponds to an inner rotation. Whereas the higher frequency corresponds to the outer major swirl motion.

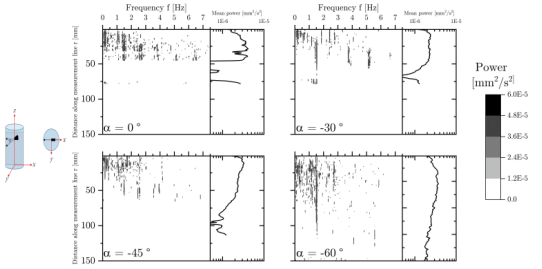

Figure 5: Frequency profiles along the measurement line summarized in a contour plot for angles 0°, -30°, -45° and -60°. Including the measured mean power

3.4 Hydrocyclone core characteristics

To assess the major characteristics of the swirl motion as seen in Figure 3, the spatiotemporal velocity field was obtained vertically for different Re-Numbers. Further, the velocity fields were decomposed into spatial and temporal modes by means of two separate fast Fourier transform (FFT) for space and time. Figure 6 shows the wavenumber over the measurement time of 127 s. High amplitudes at low wavenumbers <0.1 cm^{-1} and wavenumbers larger than 0.6 cm^{-1} were found. Averaging the amplitudes over time (Fig. 6b)) revealed amplitude peaks at 0.072 cm^{-1} and 0.042 cm^{-1} as indicated by the red lines. This indicates periods from 1.38 for small Re and 2.38 for larger Re. These findings correspond to the global motion of the steady wave of the hydrocyclone and are in good agreement with the pictures obtained (Fig. 3).

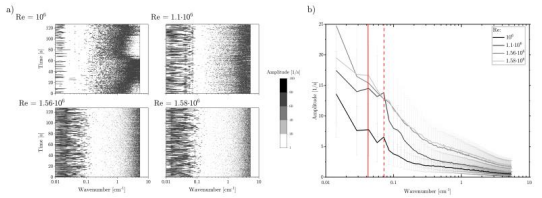

Figure 6: Fast Fourier transformed (FFT(x)) over space for different Re-Numbers. b) Time averaged amplitudes as function of wavenumber. Red lines indicate amplitude peaks at 0.072 cm^{-1} (dashed) and 0.042 cm^{-1} (drawn out).

Similar to the spatial findings, the performed temporal FFT (see Fig. 7) and averaged over the distance revealed that at low Re two peaks at a frequency of 20 and 17 Hz arise. These peaks could be attributed to the lower Re-Numbers and hydrodynamic instabilities [8]. When inlet velocity is further increased these characteristic peaks decreased and a steadier flow was observed. This unsteadiness could also be due to the bubbles used as tracers.

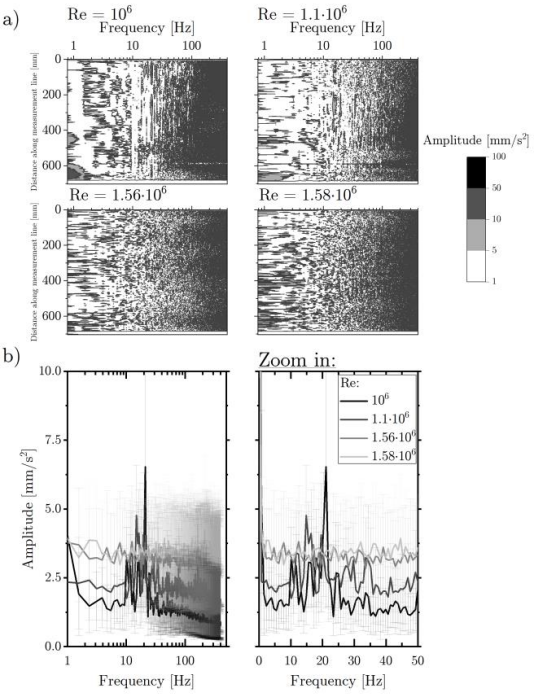

Figure 7: a) Fast Fourier transformed (FFT(t)) over time for different Re-Numbers. b) Distance averaged amplitudes as function of frequency. Zoom in of frequency range from 0 to 50 Hz.

6. Conclusion

The ultrasound doppler method showed to be a valuable tool to access the hydrodynamic characteristics of a hydrocyclone. The presented method used bubbles as tracer particles and used three different transducer positions. The obtained velocity profiles in x-z plane agreed reasonably well with the simulated data showing an alternating movement of the tracer bubbles towards and away from the transducer. When the transducer was placed inside at a range of angles (0 to -60°) an inner and outer motion at 1.5 Hz respectively 2.5 Hz could be distinguished. Further the major vertical steady wave could be accessed with UVP measurements by means of decomposing the spatiotemporal velocity field. Fast Fourier transformation showed to be a valuable tool to find the corresponding global motion and unsteadiness of flow at low Re-Number (Re=10^6).

References

[1] Cullivan, JC *et al.*: Understanding the hydrocyclone separator through computational fluid dynamics, Chemical Engineering Research and Design 2003, 81, 455–466.
[2] Rietema, K: Performance and design of hydrocyclones-IV. Design of hydrocyclones, Chemical Engineering Science 1961, 15, 320–325
[3] Antunes, M *et al.*: In Bradley Hydrocyclones: Design and

Performance Analysis BT - Hydrocyclones: Analysis and Applications; Svarovsky, L., Thew, M. T.,Eds.; Springer Netherlands, 1992; pp 3–13.
[4] Sripriya, R *et al.*: Studies on the performance of a hydrocyclone and modeling for flow characterization in presence and absence of air core. Chemical Engineering Science 2007,62, 6391–6402.
[5] Dabir, B. and Petty, C. Measurements of mean velocity profiles using laser doppler anemometry. Chemical Engineering Communications 1986, 48.
[6] Takeda, Y: Ultrasonic Doppler Velocity Profiler for Fluid Flow; Springer, 2012.
[7] Siangsanun, V *et al.*: Velocity measurement in the hydrocyclone by oil droplet, doppler ultra-sound velocimetry, and CFD modelling. The Canadian Journal of Chemical Engineering 2011,89, 725–733
[8] Takeda, Y *et al.*: Decomposition of the Modulated Waves in a Rotating Couette System. Science 1994, 263, 502–505.

6 Vertical bubbly pipe flow measurement using combined signal of ultrasonic Doppler and echo intensity profiles

13th International Symposium on Ultrasonic Doppler Methods for Fluid Mechanics and Fluid Engineering
Zürich, Switzerland (13.-15. June 2021)

Vertical bubbly pipe flow measurement using combined signal of ultrasonic Doppler and echo intensity profiles

Takumi Hayashi[1], Hyun Jin Park[2], Yuji Tasaka[2] , and Yuichi Murai[2]

[1] Graduate School of Engineering, Hokkaido Univ., N13W8, Kita-ku, Sapporo 060-8628, Japan
[2] Faculty of Engineering, Hokkaido Univ., N13W8, Kita-ku, Sapporo 060-8628, Japan

A method for measuring the void fraction in bubbly two-phase flow rising in a vertical pipe is proposed. The method utilizes both velocity and echo intensity profiles in combination so that liquid phase velocities and gas–liquid interfaces are obtained simultaneously. The velocity profile is processed with Sobel filter to detect peculiar local flow around individual bubbles and it helps to detect bubbles. The echo intensity profile is normalized by background echo of single-phase flow condition to exclude weak signals. This also realizes bubble detection with an appropriate threshold. These two kinds of information for bubble detection are combined into a single scaler field on space-time domain, to which a new threshold is given to accurately find the bubbles dispersed in the pipe. We demonstrate this technique using a vertical bubbly two-phase pipe flow with a diameter of 50 mm using a single ultrasonic transducer at 4 MHz in the basic frequency. A parametric study is conducted changing gas flow rate up to 1% in bulk void fraction. As a result, the error to be about 0.1%.

Keywords: UVP, void fraction, bubbly flow, bubble detection, echo, Doppler

1. Introduction

Airlift pumps utilizing upward force given by air bubbles to transport liquids are currently investigated as a technology for pumping mud containing rare-earth element (REE) from the deep sea. Its transportation cost and efficiency are affected by many factors such as length and diameter of the pipe, amount of the injected air, and the injection location. It is therefore necessary to set these parameters appropriately for keeping sufficient performance. For seeking the appropriate parameters, a real-time measurement of the flow rate of each phase in the pumping pipe is required. Since the pipe is made of metal and the fluid inside is expected to be opaque, the applicable measurement method is limited. In this study, we focused on ultrasonic Doppler velocity profiling (UVP), which can obtain the velocity distribution in the pipe in real-time non-invasively.

Since the airlift pump is applied to a vertical pipe and the particle size of REE mud to be pumped is small[1], we simplify the flow in the pipe as a gas-liquid two-phase flow in a vertical pipe. Since various methods have been proposed for determining the flow pattern of multiphase flows, we adopted a procedure in which the flow regime is determined by some methods[2]-[4], and then the measurement appropriate for each flow regime is performed. In this paper, we propose a measurement method focusing on bubbly flow. One of the main parameters characterizing this flow is the void fraction. In this paper, we propose a method to estimate the void fraction by detecting the bubble position using the instantaneous velocity and echo intensity distributions obtained by UVP. Bubble distributions are then calculated using a statistical method.

2. Methods

Ideally, ultrasonic wave is specularly reflected at the gas-liquid interface for bubble diameters larger than the wavelength of the ultrasonic wave[5]. It is therefore difficult to measure bubbles behind a bubble existing on the measurement line. Murai et al. proposed a statistical method to estimate the bubble distribution in measurement line from detected bubbles located at the closest position on the line from the ultrasonic transducer (TDX)[6]. In this paper, we adopt this method to estimate the void fraction in the vertical bubbly pipe flow.

2.1 Bubble detection

There are two possible ways to detect bubbles using UVP; one is to use the velocity distribution of the liquid phase, and the other is to use the echo intensity distribution. The two methods are processed in the following way and used for bubble detection. To detect bubbles from the velocity distribution, the Sobel filters with three velocity elements in velocity profiles on each of temporal and spatial directions were used to emphasize the sharp velocity gradient existing near the bubble. For the bubble detection using the echo intensity distribution, since it is known that ultrasound pulses are strongly reflected by bubbles[7][8], the normalized echo intensity distribution $I_n(r,t)$ is obtained using Eq. (1) to better emphasize the strong signal. Here, $I_{ave}$is the time-averaged echo intensity distribution and σ is the standard deviation of a single-phase flow with the same liquid-phase velocity. $I(r, t)$ is measured echo intensity distribution at each time t.

$$\begin{cases} I_n(r,t) = \left|\dfrac{I(r,t) - I_{ave}}{\sigma}\right| - 1, & \text{if } \left|\dfrac{I(r,t) - I_{ave}}{\sigma}\right| > 1 \\ I_n(r,t) = 0, & \text{otherwise} \end{cases} \quad (1)$$

After these processes, the sharp velocity gradient and strong echo intensity around the bubble are detected by setting appropriate threshold values, and thus the bubble position is estimated.

In addition to the above methods, we attempted to

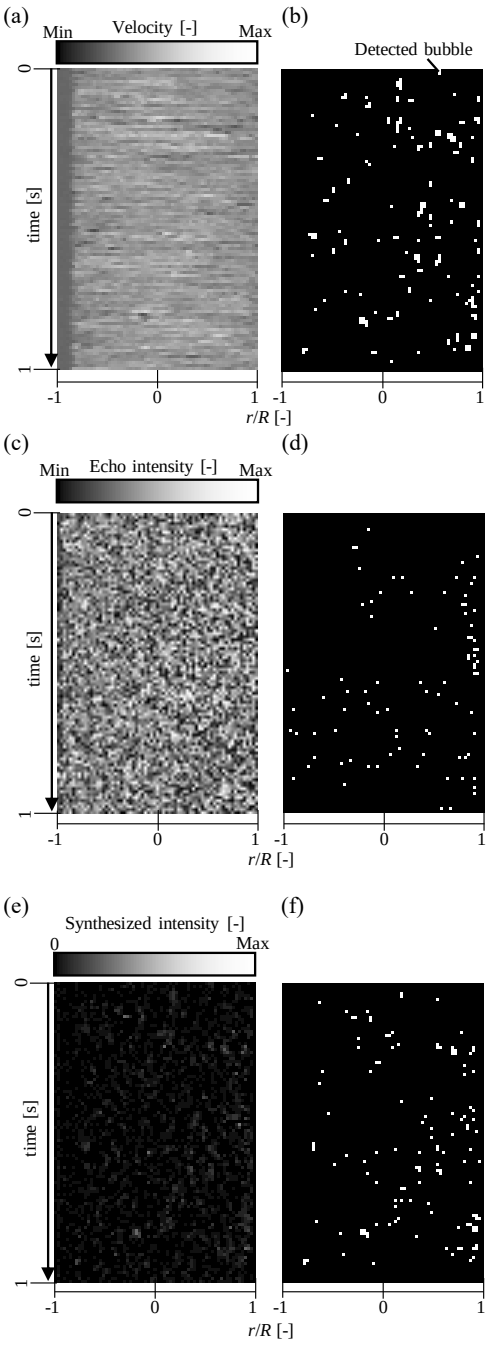

Fig 1: (a) Velocity distribution of the liquid phase, (b) detected bubbles from (a) using the Sobel filter as white points, (c) the echo intensity distribution, (d) detected bubbles from (c) using a threshold as white points, (e) the synthesized distribution D_{blend} ($w = 0.50$), and (f) detected bubbles from (e) using a threshold as white points. r means distance from the center of pipe and R means the radius of pipe. All images are under the condition of $j_L = 1.2\,[\mathrm{m/s}]$.

improve the accuracy of the detection of positions by synthesizing the filtered velocity distribution V_{Sobel} and normalized echo distribution I_n. It is expected that it supplies an improved accuracy comparing with that using only one distribution even if the distribution includes some noises because of the complementary use of two distributions. The synthesized distribution D_{blend} is expressed by Eq. (2).

$$D_{\mathrm{blend}} = (1 - w)V_{Sobel} + wI_n \tag{2}$$

In the equation, the weight coefficient w was varied in 0.01 increments over the range in $0 \le w \le 1$. Figure 1 shows the images of the velocity, echo intensity, and synthesized distributions before and after the processing.

2.2 Evaluation

To evaluate the positional accuracy of the bubble detection, each bubble distribution is compared with simultaneously visualized images. Figure 2 shows two timeline images; one is made by the optical visualization and indicates bubbles as dark areas, and the other is made from D_{blend} and shows the location of the gas–liquid interface closest to the TDX estimated from the UVP data as red points. Since TDX is located on the left side of the figure, ideally, the location of the closest gas–liquid interface is at the left edge of the black areas. Therefore, if the difference between the positions of the red dot and the left edge of black areas is small at each time, it means that the accuracy is high. In order to estimate the accuracy quantitatively, we define an error as shown in Eq. (3).

$$error = \frac{1}{T}\int_0^T \frac{|d_{\mathrm{timeline}}(t) - d_{\mathrm{UVP}}(t)|}{2R}\,\mathrm{d}t \tag{3}$$

In the equation, d_{UVP} is the position of the red dot, $d_{timeline}$ is the leftmost position in the black area, and T is the measurement time. Note that the position in the case of no bubble detected is set as $2R$.

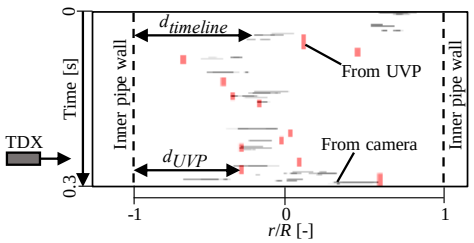

Fig 2: Bubble positions by UVP (red points) and optical visualization (black areas) for $j_L = 1.2\,[\mathrm{m/s}]$.

2.3 Bubble reconstruction

Based on the distribution of bubbles closest to TDX obtained in the previous section, the bubble distribution inside the pipe was estimated by the statistical method

suggested by Murai et al.[6]. There are many measurement points of UVP inside the pipe according to its spatial resolution and, here, we designated these points as from 1 to N in order of proximity to TDX. From the bubble distribution obtained from the UVP, the probability β_n at measurement point n that the bubble closest to TDX exists at each measurement point is calculated. The actual probability α_n at n can be expressed as a function of β_n, Eq. (4), regardless of whether it is closest to TDX or not.

$$\beta_n = \alpha_n \prod_{k=1}^{n-1}(1-\alpha_k) \tag{4}$$

This equation can be rewritten as Eq. (5) by the equation transforming.

$$\alpha_n = \frac{\beta_n}{1-\sum_{k=1}^{n-1}\beta_k} \tag{5}$$

It gives the distribution of bubbles in the pipe along the measurement line. Assuming that this distribution is symmetrical about the central axis of the pipe, the void fraction can be calculated by integrating it over the pipe cross-section.

3. Model experiments

To confirm efficacy of the present method, model experiments were performed. Then, error and void fraction were calculated by the method.

3.1 Experimental setup

Figure 3 shows the overall view of the experimental facility and the enlarged view of the water jacket. An acrylic pipe with $2R$ = 50 mm in the inner diameter, 5 mm in the wall thickness, and 2000 mm in the length was used for the experiment. The TDX was installed in the water jacket to avoid the effect of ultrasonic refraction at the acrylic wall on the UVP measurement. Also it was set at 70 mm from the pipe wall to avoid the low ultrasonic intensity area near the TDX, and the angle of inclination was set at 5° to allow for the velocity measurement range. The ultrasonic basic frequency was 4 MHz. Velocity and echo intensity distributions were measured by an ultrasonic velocity profiler (UVP-DUO, Met-Flow). For comparison with the ultrasonic measurement, a high-speed video camera (FASTCAM Mini AX50, PHOTRON) and a sheet red laser (DPRLu-5W, Japan Laser Co., Ltd.) were used to visualize the flow on the measurement line of UVP. During the experiment, water containing tracer particles (HP20SS, Mitsubishi Chemical Corporation) was raised in an acrylic pipe and the air was injected from near the bottom of the pipe. The apparent flow velocity j_L in the liquid phase was set as two conditions (1.2 and 2.0 m/s), and the apparent flow velocity j_G in the gas phase was fixed at 0.010 m/s. Void fractions estimated from j_L and j_G were 0.83% and 0.50% respectively. Single-phase flow was also measured at each liquid-phase velocity condition to be used for normalization of the echo intensity described in Section 2.1.

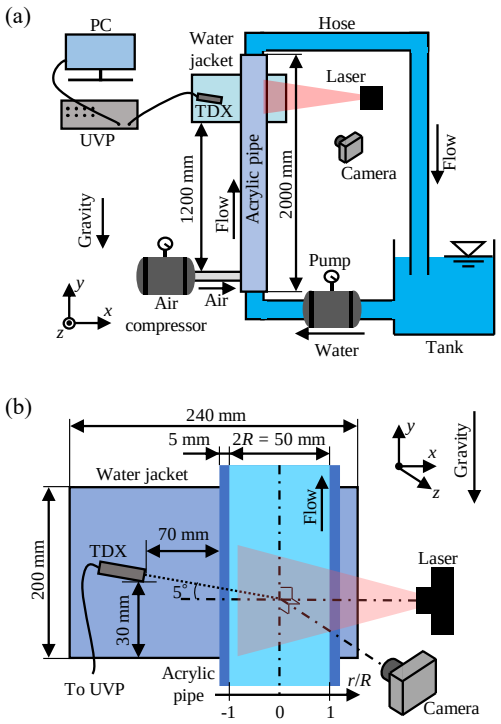

Fig 3: (a) Schematic overview of experimental setup, and (b) enlarged image around the water jacket.

3.2 Results

First, the accuracy of bubble detection using the two distributions is compared with that using the synthesized distribution in terms of the value of error. Figure 4 shows the error values of the velocity distribution alone, the echo intensity distribution alone, and the synthesized distribution under two liquid velocity conditions, j_L = 1.2 and 2.0 m/s. w in the synthesis is set so that error takes the minimum value: w = 0.50 at j_L = 1.2 m/s, and w = 0.25 at j_L = 2.0 m/s. If the value of error is smaller when the distributions are synthesized, it can be said that the bubble detection accuracy is improved by the synthesis. When void fraction was high, the value of error was reduced by the synthesis. In the other case, however, there was no noticeable difference between the synthesis and the velocity distribution alone. This means that when the void fraction is very low, bubbles can be identified accurately by the velocity profile alone, but when the void fraction is relatively high, the accuracy decreases relatively. In addition, the accuracy of synthesis increases to use the echo intensity auxiliary. The reason for this is as follows. As the void fraction increases, the distance between bubbles narrows and the flow around the bubbles interferes with each other, and therefore the accuracy of bubble detection by the velocity distribution becomes lower. On the other hand, since the internal processing process of the

echo intensity output by the UVP-duo used in this paper is unknown, the accuracy of bubble detection based on echo intensity alone is low. However, as can be seen from the figure, the change in accuracy with the change in void fraction is small. Therefore, as the void fraction increases, the detection accuracy by the synthesis is considered to increase relatively. The bubble distribution with the smallest error in each condition was used to restore the bubble distribution. Assuming that the restored bubble distribution was axial in the pipe, the void fraction was estimated. The estimated void fraction is shown in Fig. 5. The error in the estimated void fraction was about −0.1% for both velocity conditions. The small value of the estimated void fraction indicates that there were many undetected bubbles and that the bubble detection position by the UVP was farther from the center of the pipe than the actual bubble position.

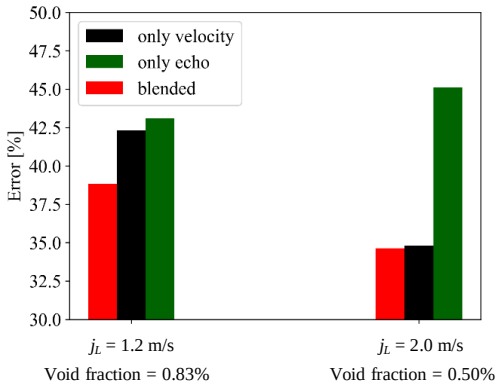

Fig 4: Change in error due to different methods of acquiring bubble distribution under two conditions. (High void fraction: j_L =1.2 m/s, void fraction is 0.83 %, Low void fraction: j_L =2.0 m/s, void fraction is 0.50 %) Red bar shows the error values of blended distribution, black shows that of the velocity distribution alone, green shows that of the echo intensity distribution alone.

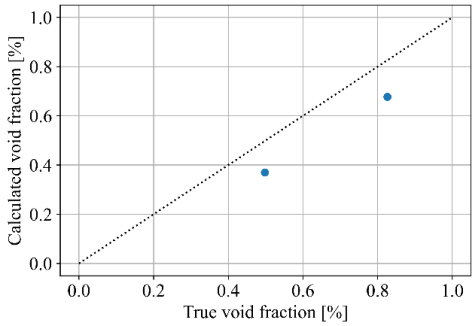

Fig 5: Calculated void fraction of both condition as blue dots. Closing to dotted line, decreasing calculation error.

4. Summary

In this paper, we developed a method to estimate the void fraction of bubbly flows in a vertical pipe by acquiring the bubble distribution using velocity and echo profiles obtained from UVP and a weighted coefficient. Its accuracy of detected bubble position was evaluated by comparing with simultaneous images taken by the optical visualization. As a result, accuracy of the present method was improved about 5% in a bubbly flow with a high void fraction, 0.83%. In the condition with a low void fraction, 0.50%, the accuracy was almost similar to that using only velocity profiles without echo information. In all measurements, the accuracy of void fraction estimated using the acquired bubble distributions was within 0.1%. The present method has some problems to solve as future works; one is a high error rate of bubble location detected by the ultrasonic measurement and the other one is how to judge the weighted coefficient. The former can be solved by measuring with higher time resolution, and the latter can be solved by finding some law for the value of w.

Acknowledgment

This research is financially supported by New Energy Develop Organization (NEDO), Japan (C.N. 19101191-0). The authors thank to Mr. T.Sampo and Mr. D. Yoon for their technical supprots.

References

[1] Simizu, Y., Hatakeyama, N., and Masuyama, T., Numerical analysis on air-lift pumping system for mining rare-earth rich mud, *Journal of MMIJ* (Mining and Material processing Institute of Japan), Vol. 134, No.10 (2018), pp.142-150

[2] Zhang, Y., Azman, A.N., Xu, K.-W., Kang, C., Kim, H.-B., Two‐phase flow regime identification based on the liquid‐phase velocity information and machine learning, *Exp. Fluids*, Vol.61, No.212 (2020)

[3] Wang, S.-Q., Xu, K.-W., Kim, H.-B., Continuous Wave Ultrasonic Doppler Modeling for Oil-Gas-Water Three-Phase Flow Velocity Measurement, *International Journal of Heat and Mass Transfer*, Vol.148 (2020)

[4] Tan, C., Dong, X.X., Dong, F., Development of an ultrasonic void fraction profiler, *IEEE Sensors Journal*, Vol.18, No.9 (2018)

[5] Murai, Y., Tasaka, Y., Nambu, Y., Takeda, Y., Tasaka, Y., and S. Roberto, Conzalez, A., Ultrasonic detection of moving interfaces in gas-liquid two-phase flow, *Flow Measurement and instrumentation*, Vol.21 (2010), pp.356-366

[6] Murai, Y., Ohta, S., Shigetomi, A., Tasaka, Y., and Takeda, Y., Development of an ultrasonic void fraction profiler, *Measurement Science and Technology*, Vol.20, No.11 (2009)

[7] Wongsaroj, W., Owen, J.T., Takahashi, H., Thong-Un, N., Kikura, H., 2D velocity vector profile measurement on bubbly flow using ultrasonic technique, *Mechanical Engineering Journal*, Vol.7, No.3 (2020)

[8] Murakawa, H., Kikura, H., Aritomi, M., Application of ultrasonic multi-wave method for two-phase bubbly and slug flows, *Flow Measurement and instrumentation*, Vol.19 (2008), pp.205-213

7 Effects of inhomogeneous fluid field on UVP measurement

13th International Symposium on Ultrasonic Doppler Methods for Fluid Mechanics and Fluid Engineering
Zürich, Switzerland (13.-15. June 2021)

Effects of Inhomogeneous Fluid Field on UVP Measurement

Tomonori Ihara, and Tatsuya Hazuku

Dep. of Marine Electronics and Mechanical Engineering, Tokyo University of Marine Science and Technology, 2-1-6 Etchujima, Koto-ku, Tokyo 135-8533, Japan

The ultrasonic velocity profile method relies on acoustic propagation in the media, which is the measurement field of interest. Some applications such as the mixing region of a jet have steep gradients of acoustic properties especially acoustic speeds due to their inhomogeneous fluid field. Practical issues related to this are ultrasonic beam bending and velocity estimation error. Ocean acoustics have treated this phenomenon whereas their interest is a rather larger area than the typical UVP measurement. This study investigates theoretical considerations of ultrasonic wave behavior as well as numerical simulations focusing on the hydrothermal vent flow. A simple laboratory-scale experimental is also conducted to assess the effects of an inhomogeneous fluid field on UVP measurement.

Keywords: Inhomogeneous fluid field, Acoustic simulation, Measurement accuracy

1. Introduction

A hydrothermal vent discharges geothermally heated water on the seafloor and forms mineral deposits, which can be exploited as mineral resources. The vent fluid transports dissolved minerals, mass, and heat to the seafloor since heated water is a supercritical fluid before discharge and dissolves chemicals from the crust. Minerals precipitate quickly when the fluid is cooled down by surrounding seawater. The vent typically is, therefore, observed as the emission of smoke from the seabed and often forms vent chimneys. This phenomenon is treated as a buoyant axisymmetric jet with chemical deposition from a fluid mechanics point of view. Clarification of flow structure is important to understand deep-sea mass transport as well as chimney formation. Some research (for example, [1]) has been done in this field, however, many of them focus on macroscale transport (scale of few ten meters), where deposits can be considered plume, and flow characterization just after the vent was not fully investigated. Hydrothermal vent flow is a challenging target for experimental fluid dynamics tools due to its high pressure, high temperature/gradient, and deployment constraints.

We have applied UVP which is deployed with a remotely operated vehicle at the Okinawa Trough. A practical issue in measuring the vent is inhomogeneous acoustic property along the ultrasonic measurement line. Figure 1 shows the temperature dependency of sound speed at the pressure of 10 MPa, which is the surrounding pressure at the aforementioned hydrothermal vent field in our study. Note that two curves are not continuous since one is the plot of the hydrothermal seawater [2] and the other is that of the standard seawater [3]. As mentioned above, hydrothermal fluid has a steep temperature gradient; the center of the jet is as high as 310 °C and the ambient temperature is 4 °C. It results in twice as large as sound speed difference along the ultrasonic measurement line. Ultrasound could be bent following Snell's law. There is, needless to say, also temperature dependences on density and acoustic impedance. Our preliminary measurement results suggest amplitude increases around the edge of the jet-mixing region, which might be attributed to the acoustic impedance difference over temperature.

The purpose of this study is to investigate ultrasonic behavior along an inhomogeneous fluid field in order to understand the effects of that especially for the measurement of hydrothermal vent fluid. Two-dimensional numerical simulation is firstly conducted to evaluate beam bending and echo amplitude. A simulated experiment was then performed in the laboratory using an ethanol-water mixture.

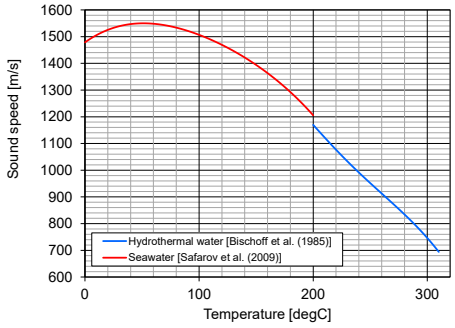

Figure 1: Sound speed of hydrothermal/sea water at 10 MPa.

2. Numerical simulation

2.1 Method

UVP utilizes the Doppler effect of propagating elastic waves. Its propagation behavior is determined by the properties of media in the measurement field. Sound speed determines the wavelength and the beam axis will be bent according to Snell's law if it varies on a boundary. Acoustic impedance, which is a product of density and sound speed determines reflection/transmission through the boundary which has different impedances. In this section, those effects were evaluated with a numerical simulation. We have employed a commercial two-dimensional FDTD software (Wave 2000, Cyberlogic Inc.) in this study. The simulation region is 50×200 mm with infinite boundary conditions. Acoustic properties were set at the pitch of 0.5 mm to model a jet profile. Previous reports suggest that hydrothermal jet has a

Gaussian profile. Thus, the profile is set with the Gaussian profile (σ= 20 mm) and the peak temperature of 310 °C. Properties from Ref. [2] and [3] are not continuous at 200 °C due to the difference in seawater. Actual measured properties are of course demanded detailed discussion. On the other hand, for a qualitative discussion, we have decided to just interpolate those data smoothly in the simulation so that the calculation converges. An ultrasonic transducer is set at the left-top position with an angle of 14°. The frequency is 3.6 MHz and the effective diameter is 10 mm. The mesh size is 10 μm and the time step is decided so that a courant number becomes 0.8. The sound speed profile is shown in Figure 2 together with the beam angle profile. The beam angle is iteratively estimated from the sound speed profile with a ray-tracing approach according to Snell's law at the resolution of 0.5 mm. Acoustic impedance also draws a similar profile.

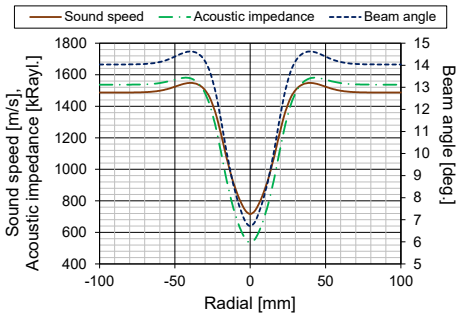

Figure 2: Sound speed, acoustic impedance, and beam angle profiles.

2.2 Results

Figure 3 shows the snapshot of the simulation. The ultrasonic wave propagates from the left-top to the right-bottom. A certain fraction of wave is reflected back to the transducer due to the difference in acoustic properties. As can be seen in the figure, there is a numerical error arising at those boundaries. This is due to the limited material property input on the simulation software and property difference is not smooth enough. In addition to that, the boundary condition is not fully working as intended despite many other trials. Reflected echo observed at emission transducer also suffers from those erroneous parasite echoes. These echoes are somewhat uncorrelated with the original excitation pulse frequency by nature as it comes from a numerical error. Thus, the actual echo due to property changes can be filtered out. In this study, a band-pass filter, heterodyne demodulation, and low-pass filter were applied in this order. Figure 4 shows extracted amplitude by this procedure in the decibel scale. A centerline of the jet corresponds to 160 μs. Amplitude increases at the latter half of the echo since some numerical error could not be fully filtered out. Observing the acoustic impedance profile on Figure 2, inflection points before the centerline. Echo amplitude has two peaks on the left-hand side. Considering the reflection at the interface of two media described by Eq. (1) where Z is an acoustic impedance, reflection occurs somewhat as a derivative of acoustic impedances at the interface.

$$R = \frac{|Z_1 - Z_0|}{Z_0 + Z_1} \tag{1}$$

This interpretation explains well the simulated echo amplitude profile. Regarding the propagation axis, it followed the angle which is estimated in Figure 1 while the beam spreads more than the original beam divergence angle. (Detailed propagation movie is going to be presented at the symposium.) It suggests that the simple ray approach cannot be applicable where the sound speed varies extensively.

Figure 3: Snapshot of numerical simulation (65 μs).

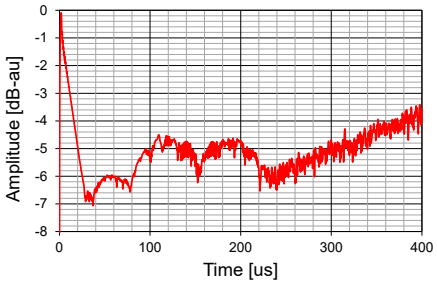

Figure 4: Filtered echo amplitude from numerical simulation.

3. Laboratory experiment

3.1 Experimental setup

A laboratory-scale experiment is prepared to confirm the discussion upon the simulation in the previous section. One of the practical issues due to the UVP method is beam alignment. This issue is critical when it comes to jet measurement. As a solution to this, we have employed an optical fiber-installed ultrasonic transducer. The basic frequency is 4 MHz and the efficient diameter is 5 mm. At the center of the transducer, there is a thin stainless tube (outer diameter of 0.8 mm and inner diameter of 0.6 mm) where a fiber laser can be installed. Acoustic fields are simulated in Figure 5 based on the method in Ref. [4]. The optical hole does not affect other than the near field and there is practically no difference with a normal transducer.

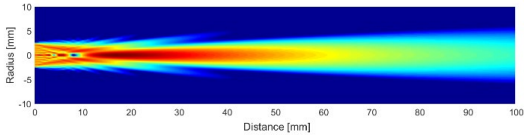

(a) Normal planner transducer.

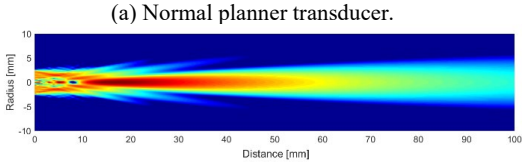

(b) With optical fiber hole.

Figure 5: Calculated acoustic fields without/with a fiber hole.

The main point of the laboratory-scale experiment here is to confirm the effects of inhomogeneous acoustic properties along the ultrasonic measurement line. Therefore, the simulant fluids shall present a large sound speed difference or density difference. In addition to that, they can be diluted well when mixed and should be safely handled during the experiment. Considering the above, ethanol jet into the water is chosen in this study.

An injection nozzle (diameter of 8 mm) is mounted in a water tank filled with deionized water so that jet develops vertically. A flow conditioner is installed behind the nozzle. Red dyed ethanol is fed with the gear pump (GPU-3, As One Corporation) and the flow rate is measured by the flowmeter (OF10ZZWN, Aichi Tokei Denki Co., Ltd.). Water in the tank is firstly circulated so that the flow develops well and then the flow is switched to the ethanol. Flowrate is 0.5 liter/min. The transducer is mounted in the water tank from the nozzle level so that the beam axis meets the jet centerline at 10.5 mm above the nozzle with an angle of 10 degrees upward. Note that the beam angle is opposite from the simulation in the previous section. Two-cycle tone burst ultrasound pulse is emitted at the repetition frequency of 1 kHz with the pulser/receiver (JPR-10B, Japan Probe Co., ltd.) and digitized at 50 MS/s (APX-5040, Aval Data Corp.). The receiver gain was +40dB. The velocity profile is estimated with an in-house code. The number of repetitions is 100. Backlit video is recorded by the USB-3 machine vision camera (STC-MBS510U3V, Omron Sentech Co., Ltd. and HF50XA-5M, Fujifilm Corp.) at the frame rate of 100.

Buoyant jet is characterized by Reynolds number and densimetric Froude number.

$$\mathrm{Re} = \frac{\hat{u} \cdot D}{\nu} \tag{2}$$

$$\mathrm{Fr} = \frac{\hat{u}}{\sqrt{\Delta\rho/\rho_{\mathrm{amb}} \cdot gD}} \tag{3}$$

Typical hydrothermal fluid is fully turbulent (Re > 104) and Fr ~ 10. Because of the limited size of the experimental setup, the Reynolds number of the experiment was 500 and the Froude number was 1.6. Therefore, the jet is laminar to the turbulent transient regime and differs from the actual hydrothermal vent. However, inhomogeneous effects should be observed since acoustic phenomena are not related to fluid flow structure.

3.2 Results

When red-dyed ethanol is discharged into the water, the jet region is colored according to its concentration. As the video is taken with the monochrome camera, the brightness drops where the jet develops. Assuming the brightness is proportional to the concentration, it can be estimated by the procedure: subtract the background and scale by the minimum brightness. Background subtracted snapshot of the experiment is shown in Figure 6 (a). and averaged image over 5 seconds is shown in (b). The potential core region and jet development region can be clearly seen. As the flow is a transient regime and the Froude number is low, the buoyant region is limited and the jet diameter along the ultrasonic beam is around 8 mm.

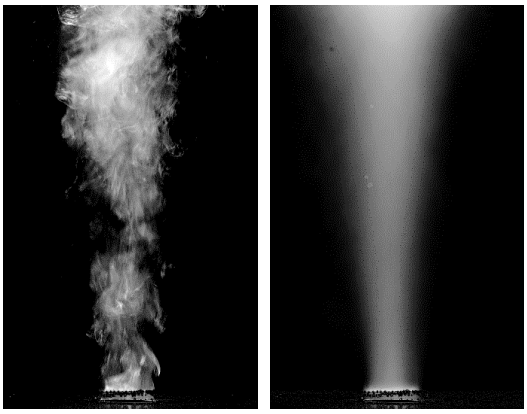

(a) Snapshot image. (b) Averaged image.

Figure 6: Processed image of the jet.

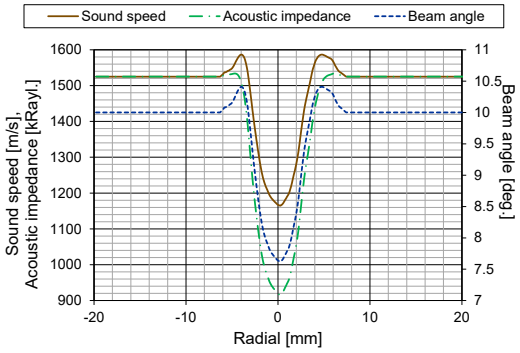

Figure 7: Estimated acoustic property profiles from image brightness.

Ethanol concentration is estimated by the aforementioned procedure. Sound speed, acoustic impedance, and beam angle are calculated using equations from Refs. [5-6] as shown in Figure 7. Property profiles draw similar curves with those in Figure 2 while increasing inflection points of acoustic impedance are rather smaller.

Amplitude profiles of UVP measurement are shown in Figure 8. Profiles are average over 15 seconds (150 profiles). No tracer particle was added and therefore profile of water comes from microbubbles in the fluid. The flow has a typical parabolic profile which suggests the flow conditioner works well. The profile of the ethanol jet deviates from that of the water jet. The difference in magnitude could be due to the suspended particle of dye, however, the horn-shaped amplitude jump is obviously due to the impedance difference as seen in Figure 4. The simulant ethanol-water mixture does not have a steep impedance difference compared with the hydrothermal seawater. Therefore, two inflection points before the jet centerline could not be observed. Amplitude drops slowly compared with the water jet profile. This could be attributed to the dilution of ethanol. While the ethanol concentration is estimated from the video footage brightness, actual concentration can differ due to the

limitation of dynamic range and moreover the simple assumption; the brightness is proportional to the concentration. Ultrasound is reflected at an anomaly in the fluid. Ethanol can dilute quicker and spreads outside of the jet mixing region. It could be the reason that the amplitude profile is extended during the ethanol jet. As a matter of the fact, the amplitude increases rapidly when the fluid is switched from water to ethanol, and it drops again the fluid is switched back to the water.

Velocity profiles are shown in Figure 9. The theoretical velocity profile of a non-buoyant jet can be described by the following equations [7].

$$u_r = \frac{3}{8\pi}\frac{K_a}{\nu x}\frac{1}{(1+\eta^2)^2} \tag{4}$$

$$u_x = \frac{1}{2}\sqrt{\frac{3K_a}{\pi}}\frac{\eta}{x}\frac{1-\eta^2}{(1+\eta^2)^2} \tag{5}$$

$$\eta = \frac{1}{8}\sqrt{\frac{3K_a}{\pi}}\frac{1}{\nu}\frac{r}{x} \tag{6}$$

where K_a is the kinematic momentum of jet. Ultrasonic beam diameter (5 mm) is relatively wide compared to the jet diameter. Thus, a space-averaged profile is drawn in the green solid line in the figure. Since UVP detects axial velocity component along the measurement line, the plotted line is a converted averaged velocity from Eq. (4)–(6). The foreside velocity profile of the water well matches with the theoretical curve while that of the ethanol jet shifted to the front. The distance was calculated using the constant sound speed of the water. It suggests that ethanol concentration is higher than the estimated data shown in Figure 7, which supports the discussion regarding the amplitude above. As a whole, the distance shall be corrected using the actual sound speed. Velocity profiles after -4 mm differ from the theoretical curve. It can be due to a rather big beam diameter and small misalignment of the ultrasonic beam. Velocity profile has also been analyzed with the optical flow method. The calculated profile has a typical jet profile where flow is divided into the entrainment and jet development regions while the image is not taken with a sheet light configuration. It implies that the velocity profile of the jet itself does not deviates from what can be found in the textbook. Entrainment can be seen after the potential core region while ethanol spreads strongly in addition to the beam broadening due to a rather small beam diameter in the experiment.

4. Summary

Ultrasonic behavior along the inhomogeneous fluid field is investigated both numerically and experimentally. The hydrothermal vent fluid is modeled on two-dimensional FDTD simulation. It is observed that echo amplitude changes according to the gradient of acoustic impedance. The beam path can be estimated by a simple ray-tracing approach. The laboratory-scale experiment was conducted using ethanol as a simulant hydrothermal fluid. The fiber laser installed ultrasonic transducer was used for the alignment. Measured amplitude profile supports the numerical result and the amplitude increases where acoustic impedance changes drastically. Distance is shifted due to the different sound speed in ethanol mixture from that in water. A proper correction would be, consequently, required to reconstruct an accurate profile, which requires apriori information about the temperature distribution or its assumption. It is observed that ultrasound is reflected at an acoustic anomaly such as the mixing region of water and ethanol.

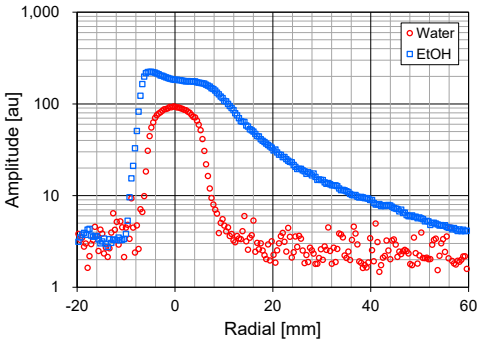

Figure 8: Measured amplitude profiles with water and ethanol jet.

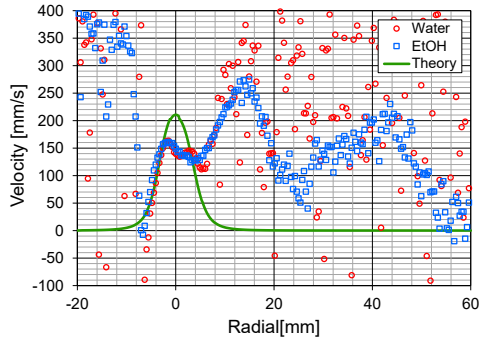

Figure 9: Measured velocity profiles with water and ethanol jet with theoretical velocity profile.

References

[1] Bemis KG, *et al.*: The path to COVIS: A review of acoustic imaging of hydrothermal flow regimes, Deep-Sea Res. II. 121 (2015), 159-176.

[2] Bischoff JL, *et al.*: An empirical equation of state or hydrothermal seawater (3.2 percent NaCl), Am. J. Sci., 285 (1985), 725-763.

[3] Safarov J, *et al.*: Thermodynamic properties of standard seawater: extensions to high temperatures and pressures, Ocean Sci., 5 (2009), 235-246.

[4] Stepanishen PR: Transient radiation from pistons in an infinite planar baffle, J. Acoust. Soc. Am., 49 (1971), 1629-1638.

[5] Tanaka Y, *et al.*: Specific volume and viscosity of ethanol-water mixtures under high pressure, Rev. Phys. Chem. J., 47 (1977), 12-24.

[6] Vatandas M, *et al.*: Ultrasonic velocity measurements in ethanol-water and methanol-water mixtures, Eur.Food Res. Technol., 225 (2007), 525-532.

[7] Schlichting H: Boundary-Layer Theory (Ninth Ed.), Springer-Verlag, Berlin (2017).

9 Determining minimum number of transects for accurate flow measurements using moving vessel ADCPs

13th International Symposium on Ultrasonic Doppler Methods for Fluid Mechanics and Fluid Engineering
Zürich, Switzerland (13.-15. June 2021)

Determining minimum numbers of transects for accurate flow measurements using moving-vessel ADCPs

Mohammad Reza Maddahi[1], Majid Rahimpour[1], Robert M. Boes[2] and Ismail Albayrak[2]

[1] Dep. of Water Engineering, Shahid Bahonar University of Kerman, Kerman, Iran
[2] Laboratory of Hydraulics, Hydrology and Glaciology (VAW), ETH Zurich, Hönggerbergring 26, CH-8093 Zurich, Switzerland

Acoustic Doppler Current Profilers (ADCPs) are widely used for flow measurements in field. A moving-vessel ADCP application decreases the measurement duration compared to stationary measurements. The minimum number of required transects at each cross section for accurate velocity and discharge measurements under different flow conditions is a fundamental question. This study addresses this question by conducting ADCP measurements in different field sites with 2D/3D fast and 2D slow flow conditions. The results show that for discharge measurements, averaging four and eight transects results in average errors of less than ±2% at 2D and 3D fast flow conditions with a streamwise velocity higher than $U > 10$ cm/s, respectively. The error increases to ±5% at 2D slow flow conditions despite averaging of nine transects. For accurate streamwise velocity profiles, a minimum number of four and eight transects is needed for fast and slow flow conditions, respectively. To determine secondary currents, averaging a minimum of eight and ten transects with ±10% error is required for 2D and 3D fast flow conditions, respectively. For 2D slow flow conditions, averaging of nine transects results in ±10% error for secondary currents. Overall, the flow conditions strongly affect the quality of the measurements.

Keywords: Acoustic Doppler Current Profiler, discharge measurements, secondary currents, velocity profile, 2D and 3D flows

1. Introduction

Acoustic Doppler current profilers (ADCP) measure three-dimensional (3D) velocities simultaneously through a vertical profile in a water column. Such velocity profiles are used to calculate discharge in waterways, rivers, lakes and estuaries. They are particularly useful for large flow regions where the measurements are affected by time limitation and study costs, and unsteady flow. There are several studies reporting a boat-mounted application of ADCPs (moving-vessel) for discharge measurements [1] and mapping of velocity fields in river reaches including primary and secondary flow structures in meandering bends [2], confluences [3] and around hydraulic structures [4]. ADCPs are also used to investigate turbulent flow structures [5] and tidal flow assessments [6].

Despite the wide range of application, ADCP velocity measurements are subject to large velocity fluctuations of around 76% of the mean velocity [7,8], which is not related to turbulent flow structures and hence reduces the accuracy of final results in terms of velocity profiles, discharge and primary and secondary flow structures. Averaging multiple transects is a way to smooth the velocity fluctuations and reduce the errors [9]. Many studies recommend from 1 to 16 transects at each cross-section to obtain accurate discharge measurements [2-4, 7].

ADCPs on a moving platform have more applications than discharge measurements, such as determination of secondary flow structures, flow field components and in-depth velocity profiles for the calculation of shear velocity. Szupiany *et al.* [8] studied these in the Parana River, Argentina, by conducting fixed and moving boat flow measurements with an ADCP. They found out that the results of horizontal flow velocities averaged from 5 moving boat transects compared well with those from 10 minutes fixed boat measurements. Furthermore, they recommended an average of five transects to study finer details of secondary currents.

Although past studies cover a wide range of ADCP applications for both fixed and moving-vessel ADCP under various flow conditions in relation to the discharge measurements, there is still a lack of knowledge and clear-cut criteria on the required number of transects for both discharge and velocity measurements under 2D and 3D flow conditions as well as for very low to high flow velocities. Accurate measurements of velocity fields are of prime importance to advance in the understanding of 3D large-scale turbulent flow structures, sediment transport, deposition processes and to address other hydraulic problems. Therefore, we aimed at determining the adequate number of transects for accurate measurements of (i) discharge, (ii) vertical velocity profile distribution, and (iii) secondary flow pattern for different flow and site conditions. To this end, we conducted 28 cross sectional ADCP measurements at four field sites in Switzerland by covering low flow velocities in a reservoir, highly turbulent and 3D flow structures at the inlet and outlet of turbines as well as 3D narrow channel and 2D flow in a straight wide channel. Herein, we focus on the results of three measurement campaigns at two study sites.

2. Study Sites and Methodology

In the following, the two selected study sites, methodology, instrumentation and data processing are described.

2.1 Study sites

Solis Reservoir

The first study site is Solis reservoir, located on the Albula River in the eastern Swiss Alps and commissioned in 1986 (Figure 1a). Further information is available in Müller-Hagmann [10]. At Solis, ADCP measurements with 10 transects were conducted at two cross-sections. The cross-section A was located at the inlet of the reservoir with elevated flow velocities, while section B was further downstream inside the reservoir with low flow velocities (Figure 1, Table 1). In addition, at the center of each cross-section, a stationary velocity measurement was conducted with a duration between 5 and 10 min at a sampling frequency of 1.5 Hz. During stationary measurements, it was difficult to keep the boat carrying the ADCP at a steady state and hence it shifted inside a circle with radius of less than 5 m.

Stroppel Hydropower Plant

The second case study is the hydropower plant Stroppel located on River Limmat 36 km downstream of Lake Zurich. The measured rectangular cross section is located upstream of the turbine intake with an aspect ratio of around 5 representing 3D narrow open channel flow conditions [11,12].

Table 1 lists the hydraulic conditions at the measured cross-sections. In this table, b and h are channel width and cross-sectionally averaged water depth, respectively. Q and U are discharge averaged over the number of transects and cross-sectionally averaged streamwise velocity, respectively. SF and FF stand for 'Slow Flow' with $U \leq 0.10$ m/s and 'Fast flow' with $U > 0.10$ m/s, respectively, characterizing the flow conditions at the corresponding study site. This threshold value was determined based on the velocity measurements from 28 cross-sections.

Table 1: Cross sections and flow characteristics at presented case study sites

Cross section	Solis A	Solis B	Stroppel A
Number of transects	10	10	12
h (m)	2.50	3.44	2.90
U (m/s)	0.32	0.06	0.61
Q (m^3/s)	25.52	14.25	26.8
b/h	12.70	18.88	5.49
Flow des.	2D/FF	2D/SF	3D/FF

2.2 Instruments, data collection and processing methods

The ADCP used in this study is River Pro 1200 kHz including a piston style four-beam transducer oriented at 20° to the vertical with a 5th, independent 600 kHz vertical beam mounted on a Q-Boat supplied by Teledyne Marine, USA. The sampling configuration for all measurements is: blanking distance 0.25 m; automatic water mode; ADCP depth from the water surface 0.12 m. Q-Boat positioning and velocity were obtained using RTK-GPS, which was interfaced with the ADCP. The Q-Boat velocity and track position were held as constant as possible along predetermined cross sections. During all measurements, the Q-Boat velocity was less than the flow velocity and maximum lateral deviations from the cross section lines were ±5 m. Velocity data were collected with the WinRiver II software. Data were processed with MATLAB based toolbox VMT [13]. Due to the beam angle separation, the flow velocities within individual profiles are spatially averaged to different degrees with depth. This spatial averaging therefore implies an assumption of temporal and spatial flow homogeneity both across and through the measured volumes, which becomes particularly large at greater distances from the ADCP head [8].

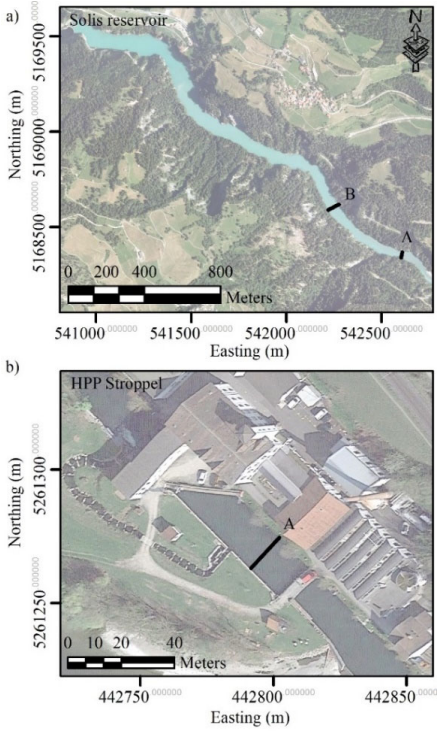

Figure 1: The measurement locations (cross sections) at a) Solis reservoir and b) hydropower plant Stroppel

3. Results and Discussion

Discharge measurements

Velocity measurement were conducted under different flow conditions. The real discharge is assumed to be the average of all transects' discharges [14]. Figure 2 illustrates the discharge measurement error as a function of the number of averaged transects for each cross-section. The errors, N_e are calculated as:

$$N_e = 100 * \frac{Q_i - Q}{Q} \quad (1)$$

Where index i represents the number of averaged transects and Q is the real discharge.

The results show that for 2D FF conditions at Solis A (Figure 2a), averaging 4 numbers of transects reduces the error to less than 2%. At Solis A, averaging more transects does not have a significant effect on the error reduction

since the error remains in the range of ±1-2%. Red dots in Figure 2 show the measurements with a duration of more than 720 seconds, while black dots represent the measurement with a duration less than 720 seconds. Figure 2a also shows that for 2D and high flow conditions, the number of averaged transects is more important than the duration of the measurements. For 3D FF conditions at Stroppel A (Figure 2b), averaging 4 numbers of transects involves errors of around ±3% while by increasing the numbers of transects to 8, the error reduces to less than 2%. At this cross section, it takes 720 seconds to measure 7 transects, but this number of transects features an error of more than 2%. Once again, the number of transects at this site is more important than the measurement duration (Figure 2b). Finally, at the 2D SF conditions occurring at Solis B, increasing the number of transects significantly reduces the error to around 10% at 6 transects, while a further increase of the transects only slightly reduces the error down to less than 5% at 9 transects (Figure 2c). The present results from three study locations reveal that the mean flow velocity has a stronger impact than the flow complexity, i.e. 2D or 3D flow conditions, on discharge measurement errors. The higher error at the slow flow conditions at Solis B possible stems from the wind effect and noise caused by the boat engine and movement and the instrument noise. Accurate discharge measurements under such flow conditions with $U \leq 10$ cm/s requires considerably more averaging than under 2D/3D FF conditions. These findings are in a good agreement with previous studies [15]. Huang [15] divided the data into the groups of low flow velocity and high flow velocity with the threshold of 35 cm/s, while in this study the threshold is even lower with less than 10 cm/s.

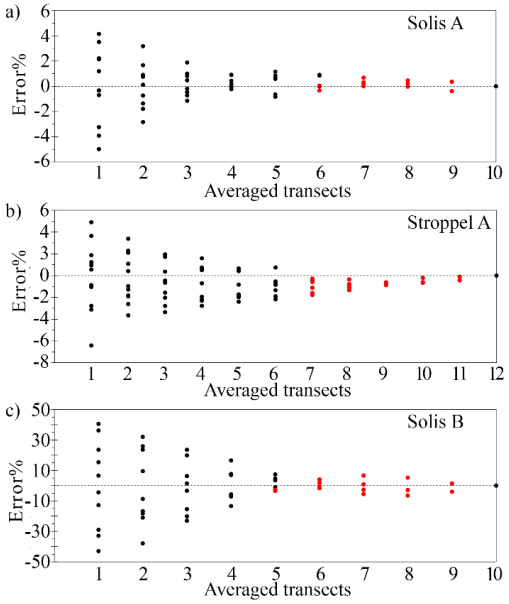

Figure 2: Discharge measurement error at each cross section for a) 2D FF, b) 3D FF and c) 2D SF conditions.

Vertical velocity profile

Streamwise velocity profiles are required in many studies such as for monitoring purposes, estimation of sediment transport, scouring processes, eco-habitat restoration, energy dissipation and for validating numerical simulations [7]. Instantaneous velocity measurements over an extended time span at a single point using a fixed ADCP clearly show that there is a good agreement between measurements and theoretical fluid mechanics velocity profiles [7]. Stationary measurements are time consuming and require great efforts, especially in wide channels. Therefore, we investigate how many transects from moving-vessel measurements are required for accurate mean velocity profiles under different flow conditions. Figure 3 compares the velocity profiles derived from different numbers of transects with the profiles obtained from fixed ADCP measurements.

Figures 3a and b show that for 2D and 3D FF conditions, one transect results in an error of ±15%. By increasing the number of averaged transects to four, the resulting velocity profile matches with stationary measurements. Further increasing the number of transects does not have a significant effect on the error reduction. For 2D SF conditions, the velocity profile extracted from averaging different numbers of transects fluctuates in the range of ±60% from stationary measurements (Figure 3c). Although increasing the averaged transects to 8 makes the velocity profile closer to the stationary measurement, it still features an error of around ±10%.

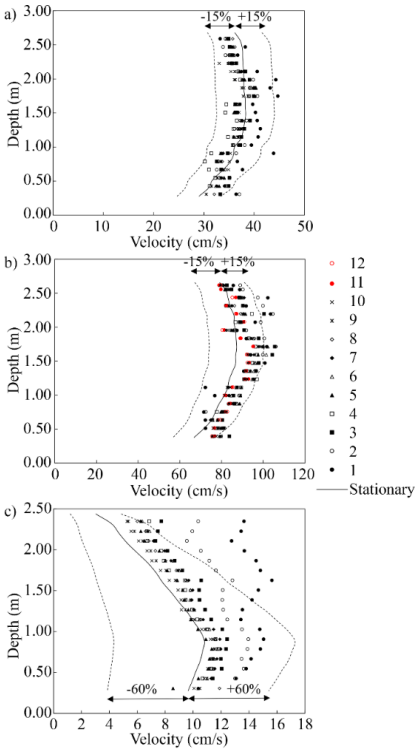

Figure 3. Effects of different number of transects on velocity profiles in a) 2D FF, b) 3D FF and c) 2D SF conditions.

Secondary flow pattern

For secondary flow patterns, accurate measurement of transverse and vertical velocities is important. Herein, it is assumed that the pattern obtained from averaging the maximum number of the measured transects is real and the difference between this pattern and the pattern obtained from lower number of transects is the measurement error. To this end, the direction of secondary flows was interpolated for the measured areas (bin size) of the cross sections and a Digital Elevation Model (DEM) was created for each averaging the numbers of transects. The created DEMs are categorized in 2 groups with negative and positive values, representing secondary flow direction to the left or right bank (group I) and to down and up (group II), respectively. The ratio of different DEMs to the real pattern of secondary flow for transverse and vertical directions is calculated. The areas with negative values in the resulting map show that the direction of the secondary flow, in transverse or vertical direction, is opposite to the real direction. Therefore, the fewer the areas with negative values, the smaller the error is. To calculate the error for each set of averaging transects, the percentage of the area with negative values is calculated. Figure 4 shows the error for transverse and vertical direction in the measured cross sections. For 2D and 3D FF conditions, increasing the number of transects sharply reduces the error, whereas for 2D SF condition the error reduces more mildly. The results indicate that the minimum required number of transects for secondary flow measurements with an error of ± 10%, are 8 and 10 for 2D and 3D FF conditions, receptively, and at least 10 for 2D SF conditions.

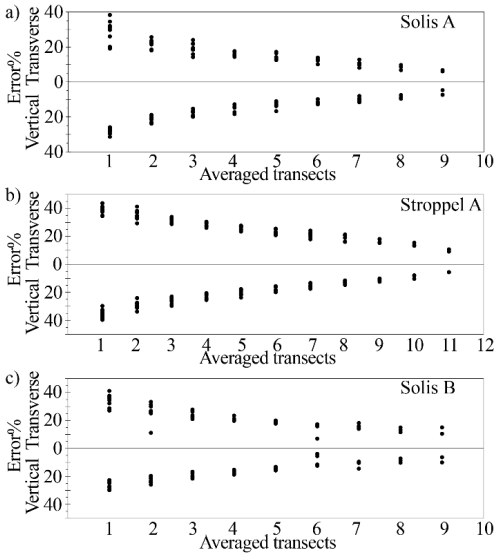

Figure 4. Effects of different number of transects on secondary currents in a) 2D FF, b) 3D FF and c) 2D SF conditions.

6. Summary

The present findings indicate that the moving-vessel ADCP application is capable to measure different parameters under different flow conditions. Flow velocity is the dominant parameter to determine the required numbers of transects for discharge measurement and velocity profiles. For slow flow conditions, a minimum number of 6 and 9 transects are recommended with errors of 10% and 5%, respectively. Accurate streamwise velocity profiles require minimum numbers of 4 and 8 transects for fast and slow flow conditions, respectively. To determine secondary flow patterns accurately, it is recommended to measure at least 8 transcets.

Acknowledgement

The authors gratefully acknowledge the support of the research project by the Swiss Federal Office of Energy SFOE (grant numbers SI/501785-01), the electric utility of Zurich ewz and Axpo Power AG.

References

[1] Mueller DS, *et al.*: Measuring discharge with acoustic Doppler current profilers from a moving boat, U.S. Geological Survey (2013).
[2] Petrie J, *et al.*: Combining fixed- and moving-vessel acoustic Doppler current profiler measurements for improved characterization of the mean flow in a natural river, Water Resour. Res., 49 (2013), 5600-5614.
[3] Tsubaki R, *et al.*: New 3-D flow interpolation method on moving ADCP data, Water Resour. Res., 48 (2012), 1-15.
[4] Jamieson EC, *et al.*: Evaluation of ADCP bed velocity in a large sand bed river: Moving versus stationary boat conditions, J. Hydraul. Eng., 137 (2011), 1064-1071.
[5] Le TB, *et al.*: Large-eddy simulation of the Mississippi River under base-flow condition: hydrodynamics of a natural diffluence-confluence region, J. Hydraul. Res., (2018).
[6] Hale R, *et al.*: Observations and scaling of tidal mass transport across the lower Ganges-Brahmaputra delta plain: implications for delta management and sustainability, Earth Surface Dynamics, 7 (2019), 231-245.
[7] Muste M, *et al.*: Practical aspects of ADCP data use for quantification of mean river flow characteristics. Part I: Moving-vessel measurements, Flow Meas. Instrum., 15 (2004), 1-16.
[8] Szupiany RN, *et al.*: Comparison of fixed- and moving-vessel flow measurements with an aDp in a large river, J. Hydraul. Eng., 133 (2007), 1299-1309.
[9] Gunawan B, *et al.*: Comparing fixed-vessel and moving-vessel ADCP measurements in a large laboratory flume, J. Hydraul. Eng., 143 (2017).
[10] Müller-Hagmann M: Hydroabrasion in high-speed flow at sediment bypass tunnels, VAW-Mitteilung 239 (R. Boes, ed.), ETH Zurich (2017).
[11] Nezu I & Nakagawa H: Turbulence in open-channel flows, IAHR monograph series, Balkema, Netherlands (1989).
[12] Auel C, *et al.*: Turbulence characteristics in supercritical open channel flows: Effects of Froude number and aspect ratio, J. Hydraul. Eng., 140 (2014), 04014004.
[13] Parsons DR, *et al.*: Velocity mapping toolbox (VMT): A processing and visualization suite for moving-vessel ADCP measurements, Earth Surf. Processes Landforms, 38 (2012), 1244-1260.
[14] García C, *et al.*: Variance of discharge estimates sampled using acoustic Doppler current profilers from moving platforms, J. Hydraul. Eng., 138 (2012), 684-694.
[15] Huang H: Estimating bias limit of moving-boat ADCP streamflow measurements, J. Hydraul. Eng., 144 (2018), 04018024.

10 Yield stress determination in thixotropic crystal-melt suspensions

13th International Symposium on Ultrasonic Doppler Methods for Fluid Mechanics and Fluid Engineering
Zürich, Switzerland (13.-15. June 2021)

Yield stress determination in thixotropic crystal-melt suspensions

Kim Mishra[1], Damien Dufour[1], Silas Ehrengruber[1], Julia Merkel[1], and Erich J. Windhab[1]

[1]Institute of Food Nutrition and Health, ETH Zürich, Schmelzbergstrasse 9, 8092 Zürich

Crystal-melt suspensions (CMS) are yield stress shear thinning fluids in which crystal network formation is responsible for the appearance of a yield stress. This study investigates the influence of crystal concentration and morphology on the yield stress of CMS made from anhydrous milk fat (AMF), cocoa butter (CB), and palm kernel oil (PKO). Ultrasound veolocity profiling – pressure difference is applied to determine the yield stress directly after crystallization. Crystallization in laminar flow depends on shear, thus different shear rates are applied to produce CMS. For AMF and CB the yield stress decreases with increasing shear rate, whereas for PKO the opposite is the case. Polarized light microscopy (PLM) reveals that the change in crystal morphology as function of shear rate is responsible for the different behavior of AMF and CB compared to PKO. For AMF and CB, spherical (AMF) and needle (CB) like crystal aggregates are disaggregated with increasing shear rate leading to a weaker network. In the case of PKO, spherical are disaggregated into needle like crystal aggregates with increasing shear rate leading to an increased network formation.

Keywords: UVP-PD, rheology, crystal-melt suspension, yield stress, lipids and fats

1. Introduction

The flow behavior and material characterization of yield stress fluids containing crystals plays a major role in lipid (fat/oil), polymer, metal or magma melts as well as in concentrated solution/dispersion systems.[1]–[4] They have in common that a liquid (melt or solution) and solid (crystal) may coexist under given temperature conditions. From a rheological perspective, cooling a melt below its crystallization temperature or a solution below a temperature at which supersaturation reaches a critical value, crystal formation transforms the fluid system from a Newtonian fluid to a non-Newtonian suspension or even a semi-solid body. Rheology-structure relationships of crystallizing fluid systems are mostly quite complex since the crystal structure and formation kinetics can be altered by shear stress and related viscous friction-based energy dissipation acting in shear flow fields. Accordingly, thixotropy or rheopexy can be superimposed with related characteristic time scales depending on shear stress and energy dissipation rates as well as on the generated crystal shape and morphology. Such complex relationships are often poorly understood despite their relevance in applications of lipid, polymer, metal, or magma melt flow. Theoretical and experimental studies investigating lipid and magma melt rheology were found to reassemble each other.[4]–[6] Models proposed to describe lipid melts and magma systems do not contradict but rather complement each other in their different rheological description approaches. Lipid melts are characterized as weakly aggregated particle networks in the non-Newtonian shear flow regime, whereas magmas are treated as crystal-melt suspensions (CMS), with crystals interpenetrating each other described by the soft-core continuum percolation model.[4], [6], [7] The main difference between the two models is the derivation of a scaling factor α for the yield stress as a function of solids volume fraction and the presence/absence of a percolation threshold denoted as critical crystal fraction. For lipids, the fractal nature of the crystals is used to calculate such scaling factor α whereas for magmas the excluded volume of a given shape is used as calculation basis for α.[4], [6] The critical crystal fraction is calculated as function of crystal shape and defines the onset of a yield stress.[6]

In this paper, we investigated the rheological properties of CMS. Therefore, anhydrous milk fat (AMF), cocoa butter (CB), and palm kernel oil (PKO) were used as CMS model system. The liquid AMF, CB and PKO were transformed into a CMS with a scraped surface heat exchanger. Ultrasound velocity profiling - pressure difference (UVP-PD), polarized light microscopy, and pulsed nuclear magnetic resonance spectroscopy were employed to analyze and relate crystal volume fraction, crystal shape and crystal polymorphic form to the yield stress and viscosity of the CMS.

2. Material and Methods

PKO (RSPO-SG) was purchased from Florin AG (Muttenz, Switzerland). The PKO was fully molten overnight at 40 °C using a blade stirrer (RW 28W, IKA Werke GmbH, Staufen, Germany) before being used for trials.

Cocoa butter (CB) was kindly donated by Chocolat Frey AG (Buchs AG, Switzerland). Countries of origin are Nigeria, Cameroon, Ivory Coast and Ghana. The fatty acids were 61.5 wt\% saturated, 35 wt\% monounsaturated and 3.5 wt\% polyunsaturated. The CB was fully molten overnight at 45 °C using a blade stirrer (RW 28W, IKA Werke GmbH, Staufen, Germany) before being used for trials.

AMF was donated by Mibelle AG (Buchs, Switzerland). The AMF was fully molten overnight at 40 °C using a blade stirrer (RW 28W, IKA Werke GmbH, Staufen, Germany) before being used for trials.

Crystallization was performed with a scraped surface heat exchanger (SSHE) (Schröder GmbH & Co KG, Lübeck, Germany). The stator diameter $2R_o$ was 60 mm with a length of 400 mm. Using a MS25-HT/P water bath (Julabo Labortechnik GmbH, Seelbach, Germany) with 3.2 kW cooling capacity the double mantled stator was tempered within a temperature range of 5 – 18 °C. The rotor with two blades had a diameter $2R_i$ of 57 mm and was tempered at 27 - 32 °C with a Julabo F32 water bath (Julabo Labortechnik GmbH, Seelbach, Germany). The rotational speed of the rotor was adjusted by using a V-belt transmission. Since Reynolds numbers were calculated to be larger than 10 during crystallization, the shear rate $\dot{\gamma}_{SSHE}$ was calculated by solely considering the velocity field between rotor and stator as described previously:[8]–[10]

$$\dot{\gamma}_{SSHE} = \pi \frac{n_{SSHE}}{15} \frac{R_o^2}{R_o^2 - R_i^2}$$

where n_{SSHE} is the rotational speed, R_o the stator radius and R_i the rotor radius. An eccentric worm-drive pump (Allweiler GmbH, Radolfzell, Germany) pumped the liquid AMF, CB, and PKO from the double mantled stainless-steel vessel through double mantled and tempered 25 mm pipes into the gap between stator and rotor.

Solid fat content was measured by pulsed nuclear magnetic resonance spectroscopy using a 20 MHz (0.47 T) minispec mq20 (Bruker Biospin, Fällanden, Switzerland) in the direct mode. The device was calibrated using paraffin–acrylic standards. Tempered glass tubes with an inner diameter of 1 cm, a wall thickness of 0.06 cm and a height of 18 cm were filled with 3-4 cm of sample and immediately analyzed as described previously.[11] For highly viscous samples a tempered syringe with a plastic tube was used to fill the glass tubes. Analyses were performed in triplicate.

The UVP-PD measurements were done directly after crystallization. Double mantled 15 mm pipes held at 27 – 32 °C were used to convey the crystal-melt suspension. The pressure difference was measured in a 3.29 m pipe section. A diaphragm pressure sensor (CC1020, Labom GmbH, Hude, Germany) with a measurement range of 1.0 – 1.4 bar absolute pressure was used at the beginning of the pipe segment in order to calculate the pressure difference against atmospheric pressure at the pipe exit. In between the pressure sensor and the end of the pipe segment a custom-built polyvinyl chloride cell with inserted ultrasonic transducers was used to record the flow profile. Two 4 MHz transducers (Imasonic SAS, Voray-sur-L'Ognon, France) with an active diameter of 5 mm were placed at 60° and 90° angle with respect to the flow axis in order to determine the velocity profile across the pipe diameter and the speed of sound consecutively. The transducers were preferably operated at 3.75 MHz with a pulse repetition frequency of 750 Hz and 128 repetitions. The signals of the transducers were recorded with the UB-Lab device (Ubertone, Schiltigheim, France). During approximately 60 s a total of six averaged profiles were recorded for one process setting. This procedure was repeated three times for each process setting. Subsequently the profiles were deconvoluted[12]–[14] and fitted with the Herschel-Bulkley model. Fitting the Herschel-Bulkley model onto the measured velocity profile requires the plug radius R_p, flow index n and consistency factor K as fitting parameters:

$$\nu_x(r) = \begin{cases} \frac{n}{n+1} \frac{\Delta P}{2L_{pi}K}^{\frac{1}{n}} \left[(R_{pi} - R_{pl})^{1+\frac{1}{n}} - (r - R_{pl})^{1+\frac{1}{n}} \right], & \text{if } r \geq R_{pl} \\ \nu_x(R_{pl}), & \text{if } r < R_{pl} \end{cases}$$

The fitted plug radius R_p is related to the yield stress of the CMS as follows:

$$R_p = \frac{2\tau_0 L_p}{\Delta P}$$

Consequently, the larger R_p and ΔP the higher the yield stress τ_0 of the CMS. The illustration of the UVP-PD measurement track is

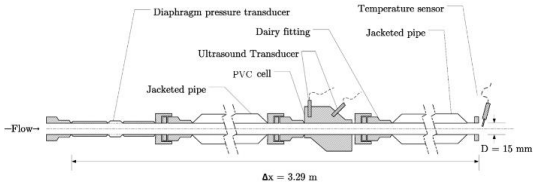

Figure 1: Schematic illustration of the UVP-PD measurement track

3. Results and Discussion

Figure 2 shows exemplarily pipe flow velocity profiles and back scattering amplitudes of CB CMS crystallized at $\dot{\gamma}_{SSHE} = 2150\ s^{-1}$ for varying crystal volume fractions Φ_{SFC}. It is evident that at low Φ_{SFC} an almost parabolic velocity profile is apparent as predicted by Newton's law. Already at $\Phi_{SFC} = 2.66\%$ a slight plug is evident indicating the onset of a yield stress. With further increasing Φ_{SFC} the plug extends to the pipe wall. At $\Phi_{SFC} = 8.80\%$, the plug extends almost the whole pipe radius denoting the upper yield stress limit at the given measurement conditions. At Φ_{SFC} of 1.73 and 2.66% the back scattering amplitude is small before increasing at intermediate Φ_{SFC} of 3.62 and 6.66%. At $\Phi_{SFC} = 8.80\%$ the backscattering amplitude rapidly decreases. For all crystal volume fractions, the far side of the transducer (positive r-coordinate) shows inaccurate velocity readings close to the pipe wall.

The small backscattering amplitude at low Φ_{SFC} is caused by insufficient number of particles for scattering. Contrary at high Φ_{SFC}, the crystals in the plug are not oriented in the flow field and are therefore increasing the attenuation coefficient leading to small backscattering amplitudes. The inaccurate velocity readings in the far side of the transducer were overcome by only considering the data from the near side of the transducer to calculate the viscosity data.

Figure 3 (A-C) shows the yield stress τ_0 as function of crystal volume fraction Φ_{SFC} for AMF, CB and PKO

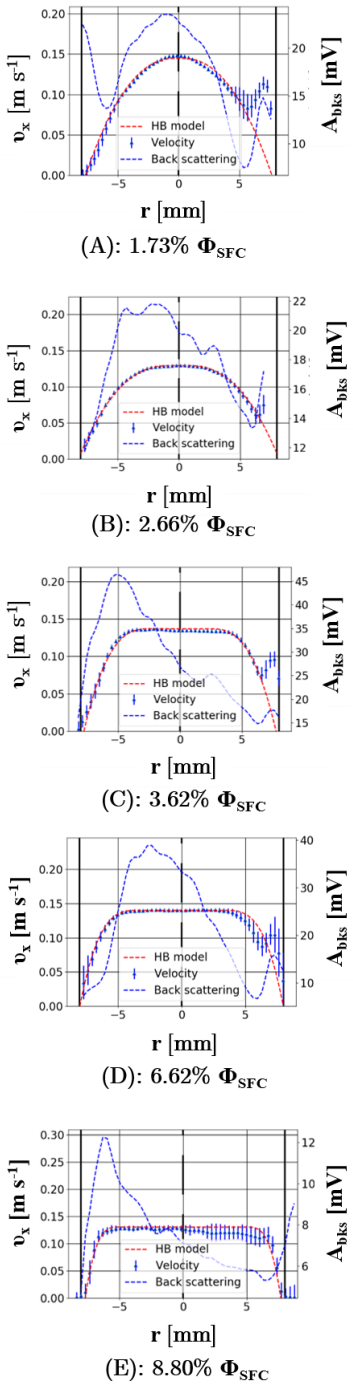

Figure 2: The fluid velocity in x-direction v_x on the left y-axis and the back scattering amplitude A_{bks} on the right y-axis as function of the pipe radius r for CB CMS crystallized at $\dot{\gamma}_{SSHE} = 2150\ s^{-1}$ for various crystal volume fractions Φ_{SFC}. The lines emerging from the velocity profile points indicate the magnitude of uncertainty. The dotted red line indicates the fitted velocity profile according to the model proposed by Herschel and Bulkley.

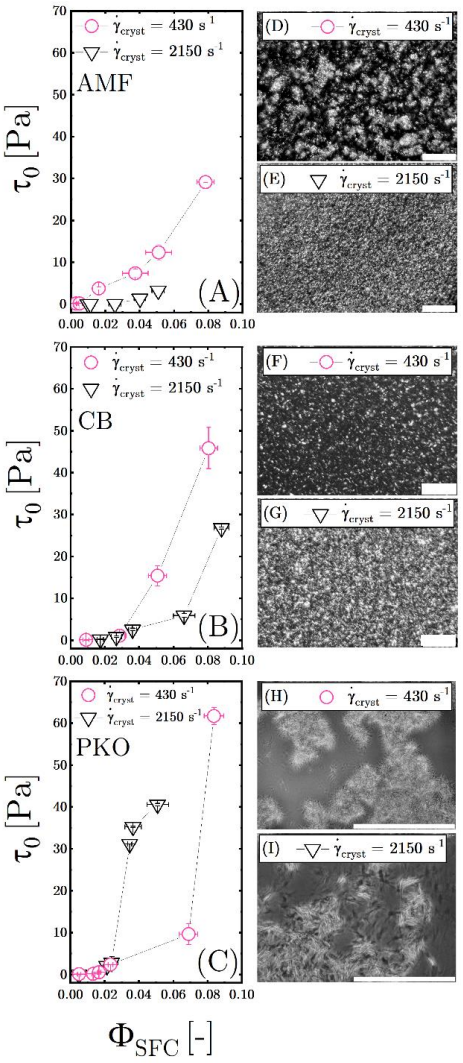

Figure 3: The yield stress τ_0 as function of the crystal volume fraction Φ_{SFC} for (A) AMF, (B) CB, and (C) PKO crystallized at $\dot{\gamma}_{SSHE} = 430\ s^{-1}$ and $\dot{\gamma}_{SSHE} = 2150\ s^{-1}$. (E-F) display polarized light microscopy images of the respective CMS for both crystallization shear rates. Bar represents 100 µm.

crystallized at $\dot{\gamma}_{SSHE} = 430\ s^{-1}$ and $\dot{\gamma}_{SSHE} = 2150\ s^{-1}$. For AMF and CB, the CMS crystallized at 430 s^{-1} shows a steeper τ_0 increase compared to the CMS crystallized at 2150 s^{-1}. For PKO, the opposite is the case. Furthermore, it is evident that AMF has lower absolute yield stresses compared to CB and PKO.

Figure 3 (E-J) show the corresponding polarized light microscopy images for AMF, CB, and PKO CMS crystallized at 430 and 2150 s^{-1}. At 430 s^{-1}, AMF shows spherical, large and loosely connected aggregates. At the same shear rate, CB shows small, isolated, and needle-like crystals. PKO shows spherulitic crystal aggregates at 430 s^{-1}, which are characterized by their spherical shape and brush-like surface. Increasing the shear rate to 2150 s^{-1},

AMF and CB crystals become smaller and less aggregated. For PKO however, the crystals change their shape from spherulitic to needle-like.

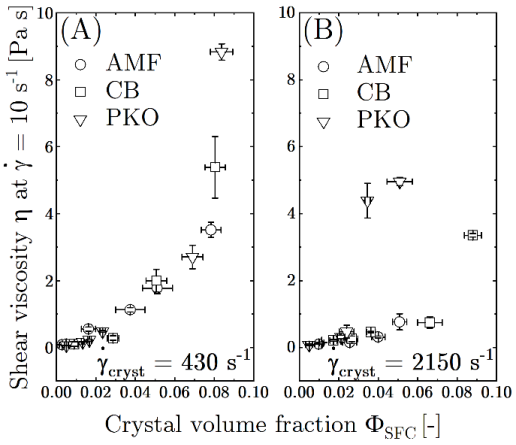

Figure 4: The shear viscosity measured at 10 s^{-1} $\eta_{\dot{\gamma}=10\,s^{-1}}$ as function of crystal volume fraction Φ_{SFC} for AMF, CB, and PKO crystallized at (A) 430 s^{-1}, and (B) 2150 s^{-1}.

Combining the information on the yield stress with the morphological insights from the polarized light microscopy images shows that AMF and CB CMS undergo a crystal deaggregation with increasing shear rates. Crystal morphology remains the same, however smaller crystals with fewer crystal-crystal bridges are present. For PKO a morphology change takes place with increasing shear rates. Spherical crystals turn into needle-like crystals. The needle-like crystals have a higher aspect ratio and therefore a decreased percolation threshold. Consequently, for PKO CMS crystallized at 2150 s^{-1} show a steeper increase of τ_0 as function of Φ_{SFC}.

Figure 4 shows the shear viscosity at 10 s^{-1} $\eta_{\dot{\gamma}=10\,s^{-1}}$ as function of crystal volume fraction Φ_{SFC} for AMF, CB, and PKO crystallized at (A) 430 s^{-1}, and (B) 2150 s^{-1}. Figure 4 (A) shows a mastercurve for the CMS viscosities crystallized at 430 s^{-1}. Below 3% Φ_{SFC}, a linear dependency between $\eta_{\dot{\gamma}=10\,s^{-1}}$ and Φ_{SFC} is apparent. Above 3% Φ_{SFC}, a non-linear increase characterizes the dependency of $\eta_{\dot{\gamma}=10\,s^{-1}}$ with Φ_{SFC} more accurately. Figure 4 (B) shows that AMF and CB crystallized at 2150 s^{-1} show decreased viscosities compared to 430 s^{-1} and a linear dependency of of $\eta_{\dot{\gamma}=10\,s^{-1}}$ with Φ_{SFC} up to 3% Φ_{SFC}. By contrast, PKO crystallized at 2150 s^{-1} shows an increased viscosity compared to 430 s^{-1}.

Figure 4 (A) shows that for CMS crystallized at 430 s^{-1}, crystal morphology does not affect the viscosity greatly. This can be explained by the increased importance of the crystal-crystal interactions due to aggregation. Figure 4 (B) shows that at 2150 s^{-1} crystal morphology affects the viscosity due to the deaggregation that takes place at such high shear rates. Consequently, the needle-like high-aspect ratio crystals of the PKO CMS result in higher viscosities compared to the lower aspect ratio AMF and CB crystals.

4. Conclusion

Measuring the rheological properties of crystal-melt suspensions (CMS) assists in understanding the flow and structure formation characteristics of liquid to semi solid polymer, metal, magma and lipid systems under crystallization conditions. The UVP-PD method was successfully employed to measure the influence of crystallization shear rate on the rheology of AMF, CB and PKO. Crystal volume fractions Φ_{SFC} up to 8.80% were measured accurately. This offers new possibilities to devise process control loops, which control for in-line real time data.

5. References

[1] A. R. McBirney and T. Murase, "Rheological properties of magmas," *Annu. Rev. Earth Planet. Sci.*, vol. 12, no. 1, pp. 337–357, 1984.

[2] O. Darras and R. Séguéla, "Tensile yield of polyethylene in relation to crystal thickness," *J. Polym. Sci. Part B Polym. Phys.*, vol. 31, no. 7, pp. 759–766, 1993.

[3] J. Banhart, H. Stanzick, L. Helfen, and T. Baumbach, "Metal foam evolution studied by synchrotron radioscopy," *Appl. Phys. Lett.*, vol. 78, no. 8, pp. 1152–1154, Feb. 2001.

[4] A. G. Marangoni and M. A. Rogers, "Structural basis for the yield stress in plastic disperse systems," *Appl. Phys. Lett.*, vol. 82, no. 19, pp. 3239–3241, 2003.

[5] S. R. Hoover, K. V. Cashman, and M. Manga, "The yield strength of subliquidus basalts - Experimental results," *J. Volcanol. Geotherm. Res.*, vol. 107, no. 1–3, pp. 1–18, 2001.

[6] M. O. Saar, M. Manga, K. V. Cashman, and S. Fremouw, "Numerical models of the onset of yield strength in crystal-melt suspensions," *Earth Planet. Sci. Lett.*, vol. 187, no. 3–4, pp. 367–379, 2001.

[7] M. O. Saar and M. Manga, "Continuum percolation for randomly oriented soft-core prisms," *Phys. Rev. E*, vol. 65, no. 5, p. 056131, May 2002.

[8] B. Breitschuh and E. J. Windhab, "Parameters influencing cocrystallization and polymorphism in milk fat," *J. Am. Oil Chem. Soc.*, 1998.

[9] E. Dumont, F. Fayolle, and J. Legrand, "Flow regimes and wall shear rates determination within a scraped surface heat exchanger," *J. Food Eng.*, vol. 45, no. 4, pp. 195–207, 2000.

[10] M. Stranzinger, A. Bieder, K. Feigl, and E. Windhab, "Effects of flow incidence and secondary mass flow rate on flow structuring contributions in scraped surface heat exchangers," *J. Food Process Eng.*, vol. 25, no. 3, pp. 159–187, Jul. 2002.

[11] B. Breitschuh and E. J. Windhab, "Direct measurement of thermal fat crystal properties for milk-fat fractionation," *J. Am. Oil Chem. Soc.*, vol. 73, no. 11, pp. 1603–1610, Nov. 1996.

[12] J. E. Jorgensen and J. L. Garbini, "An analytical procedure of calibration for the pulsed ultrasonic Doppler flow meter," *J. Fluids Eng.*, vol. 96, no. 2, pp. 158–167, Jun. 1974.

[13] P. Flaud, A. Bensalah, and P. Peronneau, "Deconvolution process in measurement of arterial velocity profiles via an ultrasonic pulsed Doppler velocimeter for evaluation of the wall shear rate," *Ultrasound Med. Biol.*, vol. 23, no. 3, pp. 425–436, Jan. 1997.

[14] M. Kagiyama, Y. Ogasawara, S. Tadaoka, and F. Kajiya, "Measurement accuracy of the flow velocity in pulsed ultrasound Doppler velocimeter," *Ultrasound Med. Biol.*, vol. 25, no. 8, pp. 1265–1274, Oct. 1999.

11 Basic study on ultrasonic remote leakage position estimation method for underwater exploration

13th International Symposium on Ultrasonic Doppler Methods for Fluid Mechanics and Fluid Engineering
Zürich, Switzerland (13.-15. June 2021)

Basic study on ultrasonic remote leakage position estimation method for underwater exploration

Takeshi Moriya[1], Hiroshige Kikura[2], and Hideharu Takahashi[2]

[1] Dep. of Mechanical Engineering, Tokyo Institute of Technology, 2-12-1 Ookayama, Meguro-ku, Tokyo 152-8550, Japan
[2] Lab. for Advanced Nuclear Energy, Tokyo Institute of Technology, 2-12-1 Ookayama, Meguro-ku, Tokyo 152-8550, Japan

Leakage from the reactor containment vessel has become an issue related to the decommissioning of TEPCO HD Fukushima Daiichi Nuclear Power Station, and it is required to investigate the leak location from inside the containment vessel. The performance of CCD cameras used for in-core exploration deteriorates in muddy water environments. Also, long arm robots and underwater robots, which are expected to be used for exploration, have a problem of low positioning accuracy. Therefore, as a survey method, we focused on ultrasonic measurement, which has radiation resistance and applies to turbid water and made it an issue to investigate leak points and estimate self-position. Therefore, we have developed a sensor self-position estimation method using ultrasonic distance measurement. Also, flow mapping measurement was performed using the ultrasonic flow velocity distribution measurement (UVP) method to grasp the position of the leak location. We proposed a method to estimate the rough location of leakage points by weighting the intersection points of the obtained two-dimensional flow velocity vectors and creating a weighted histogram. We conducted a mock test using a robot to verify the validity and adaptability of the proposed method. From the experimental results, it was confirmed that the leak location can be estimated.

Keywords: Localization, UVP, Decommissioning, ultrasonic measurement, detecting locating

1. Introduction

The decommissioning of all units from Unit 1 to Unit 6 of TEPCO's Fukushima Daiichi Nuclear Power Station has been decided due to the damage caused by the massive tsunami following the March 11, 2011 earthquake in the Tohoku region. In Units 1-3, where core damage has occurred, decommissioning is underway in accordance with the medium- to a long-term roadmap published by TEPCO HD. The main decommissioning tasks are fuel removal from the spent fuel pools, fuel debris removal, and dismantling of the facilities. In fuel debris removal, emphasis is placed on the in-air method, and it is necessary to investigate and repair the leaking points of the containment vessel cooling water in order to remove the fuel debris.

In order to identify the location of the leak, it is still impossible to enter the reactor building 10 years after the accident because of the high radiation environment. Therefore, remote measurements using robots and engineering endoscopes are being conducted. Outside the containment vessel, several leaks have already been found by the leak location survey. However, it is difficult to detect all the leaks only from the outside. In order to detect and repair all the leaks, it is necessary to identify the leaks from inside the containment vessel.

Conventional methods of leak detection have been proposed, such as investigation of cracks on the wall surface by image analysis using CCD cameras [1], and investigation of suspected leaks by spraying tracer particles around the area and detecting the movement of the particles [2]. However, image analysis using a camera is insufficient because the target is in a dark and turbid water environment. In addition, the CCD camera is not radiation-resistant, so it is not possible to investigate the inside of the containment vessel for a long time.

On the other hand, remote measurement technology using ultrasonic waves has been attracting attention. Ultrasonic devices have been used to survey the distribution of fuel debris under high radiation conditions during the accident at the Three Mile Island Nuclear Power Plant Unit 2 [3], and are characterized by their high radiation resistance. In addition, it has been demonstrated that it can be used in turbid water environments. The Ultrasonic Velocity Profiler (UVP) [4] has been developed to measure the flow of tracer particles in a liquid by using ultrasonic echo signals. The UVP method can be used to measure the flow inside a containment vessel and to estimate the location of leaks from the flow pattern.

The position and orientation of the ultrasonic sensor in the measurement environment are important factors for estimating the location of the leak from the flow direction. However, the positioning accuracy of long arm robots and underwater robots, which are expected to be used for the survey, is low. In normal environments, posture recognition using cameras and laser surveyors is used, but as mentioned earlier, the inside of the containment vessel is a turbid water environment and a high radiation environment, so it is expected to be difficult to use conventional posture estimation mechanisms. In this study, we focused on SLAM (Simultaneous Localization and Mapping), which can simultaneously estimate the self-position and generate an environmental map, because the environment inside the reactor is unknown. The purpose of this paper is to

explore the technical possibilities of self-localization and remote flow mapping measurement by applying ultrasonic sensors to SLAM technology.

2. Algorithm of leak detection method using ultrasound.

2.1 Development of location estimation technology

The objective of this study is to use ultrasonic sensors for self-positioning estimation to compensate for the amount of movement measured inside the robot. ICP [5] is an intuitive method that performs scan matching between two measurement results by alternating the mapping of measurement points and position estimation.

Initially, at a certain sensor position x_t^k, the distance of the surrounding horizontal surface is measured by TOF (Time of flight) using an ultrasonic sensor, and the measurement result is converted into measurement data. In this study, we use a stage to move a single−element ultrasonic sensor from the initial rotation position ϕ_0 to $\phi_0 + 2\pi - d\phi$ by $d\phi$, and measure the distance at each position. n is the number of sampling in the rotation direction.

The measured distance d_k in k steps is obtained as shown in Equation 1.

$$d_k = [d_k^1 \quad \cdots \quad d_k^i \quad \cdots \quad d_k^n] \tag{1}$$

By using the rotation matrix R^k and the translation vector t^k of x_t^k, we can obtain the position matrix p_i^k of the scan point in the sensor coordinate system from Equation 2.

$$p_i^k = R^k d_k + t^k \tag{2}$$

Next, find the point $q_{j_i}^k$ in the reference scan s_{t-1} that is closest to p_i^k for mapping. That is, find the point where the Euclidean distance from p_i^k is the smallest as shown in Equation 3, and make it $q_{j_i}^k$. Here, denote the point number j of s_{t-1} corresponding to the point number i of of s_t.

$$q_{j_i}^k = argmin\left\|p_i^k - q_j^k\right\| \tag{3}$$

To evaluate the position estimation, the mean square of the distance between each point is calculated from Equation 4 according to the obtained correspondence.

$$G_1(x_t^k) = \frac{1}{N}\sum_{i=1}^{N}\left\|(R^k p_i + t^k) - q_{j_i}^{k-1}\right\|^2 \tag{4}$$

To estimate the robot position, we use the steepest descent method to find x_t^k where the evaluation function $G_1(x_t^k)$ is minimized.

To determine the end of the ICP iteration, the difference between the minimum value of $G_1(x_t^k)$ and the minimum value of $G_1(x_t^{k-1})$ is less than a threshold value according to Equation 4.

2.2 Ultrasonic velocity distribution measurement method

Ultrasonic Velocity Profiler (UVP) is a measurement technique that uses ultrasonic waves to measure the velocity distribution of a liquid. When small particles are dispersed in a liquid and ultrasonic pulses are transmitted from a sensor along a measurement line, echo signals are reflected from the small particles moving in the liquid. This reflected wave is continuously acquired by the sensor. The acquired echo signal is affected by the Doppler effect caused by the velocity of the reflector. The Doppler frequency can be obtained from the continuously acquired echo signals. The Doppler frequency $f_D(i)$ is related to the velocity of the particle, and the velocity $V(i)$ of the particle at a certain position i can be calculated from Equation 5.

$$V(i) = \frac{cf_D(i)}{2f_0} \tag{5}$$

f_0 is the fundamental frequency of the ultrasonic wave, α is the angle of incidence, and c is the speed of sound in the liquid. The distance $x(i)$ from the ultrasonic sensor is calculated using Equation 6.

$$x(i) = \frac{ct(i)}{2} \tag{6}$$

The flow velocity measurement in UVP has a problem of uncertainty of the measured value near the wall. In other words, it is sometimes difficult to measure the flow velocity accurately near the wall because the reflected ultrasonic wave becomes noise. In particular, it is difficult to cope with this problem when measuring the velocity distribution over a wide area such as in the case of in-core exploration. In this study, we propose a method to estimate the rough location of leakage points by using kernel density estimation based on the intersection distribution of the measurement results.

Kernel density estimation [6] is one of the non-parametric methods to estimate the establishment density distribution of a random variable. In the reactor environment, it is difficult to obtain an appropriate parametric model because the number and spacing of leaks are unknown. Therefore, we adopted this estimation method, which has fewer processes for the distribution. Since the accuracy of kernel density estimation decreases with high-dimensional data, we decided to perform the estimation in one dimension in this study.

Suppose that n two−dimensional flow velocity vectors are obtained by measurement. The intersection points $(x_{i,j}, y_{i,j})$ on the extension line of two arbitrary velocity vectors $V_i, V_j (0 \le i, j \le n, i \ne j)$are calculated and the weight $w_{i,j}$ is calculated. This time, the weighting is the product of the magnitudes of each velocity vector. However, if there is no intersection point, the weight is 0.

Since the absolute value of the velocity vector near the leakage point is large and its contribution to the estimation is considered to be high, we assume that $w_{i,j}$ points exist at the intersection points $(x_{i,j}, y_{i,j})$, and create a histogram for each of the x and y axis. This is treated as a weighted histogram $m^w = (m_x^w, m_i^w)$. For the weighted histogram, we estimate the kernel density distribution as in Equation 7.

$$\hat{f}_h(m^w) = \frac{1}{nh}\sum_{i=1}^{n} K\left(\frac{m^w - m_i^w}{h}\right) \tag{7}$$

As the kernel function, we adopted a Gaussian function with 0 mean and 1 variance as shown in Equation 8.

$$K(x) = \frac{1}{\sqrt{2\pi}} e^{-x^2/2} \quad (8)$$

This method is expected to provide a rough estimation of the location of leaks over a wide area.

3. Leakage point investigation experiment

3.1 Equipment and method of leak point investigation experiment

To validate the methods proposed in Section 2.2 for measuring the flow velocity distribution and estimating the location of leaks, an experiment simulating a robotic survey is conducted. A polyvinyl chloride pipe (O.D. 26 mm, I.D. 20 mm) is attached to the wall of the tank as a simulated leak point. A pump was used to draw water from the leakage point, and a discharge outlet was placed on the other side of the tank to circulate the water and construct a flow field. A pulse receiver (JPR-600C, National Instruments) was used to transmit and receive ultrasonic waves, and an A/D converter (NI USB-5133, National Instruments) was used to store the received signals in a PC. A robot was used to control the position of the sensor.

The sensor-transport robot used in this experiment was designed as a mock-up of a long arm robot [7], which is being studied for decommissioning in the Suzumori-Endo Laboratory of the Tokyo Institute of Technology. This robot consists of a body and a robot arm. The payload of this arm robot is 1.94 kg, and the paw is equipped with a rotating stage and an ultrasonic sensor. The payload of the robot arm is 1.94 kg. We used this robot to control the position and direction of the sensors and perform measurements.

3.2 Equipment and method for leak point investigation experiment

Figure 1 shows the results of the position estimation of the arm in the simulated test, and the error between the hand position calculated from the forward kinematics and the actual position based on the encoder values mounted on the robot. The error means, error deviation, and maximum error of each result are shown in Table 1. It was confirmed that the position estimation was much more accurate than the hand position recognized by the robot.

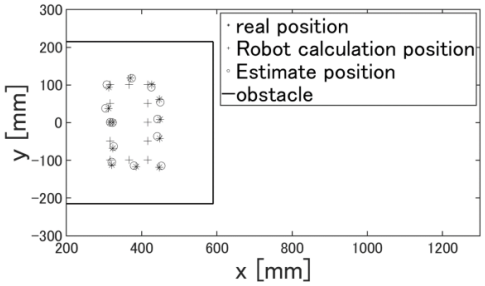

Fig. 1 Results of localization and Robot calculation

Table 1: Localization Result

	Average error[mm]	Standard deviation of error[mm]	Maximum error [mm]
Localization	9.61	10.3	9.89
Robot calculation	17.52	21.7	16.5

Table 2: Parameter configuration of UVP systems

Parameter	Value
Basic frequency	2 MHz
Pulse repetition frequency	0.5 kHz
Number of repetition	256
Spatial resolution	1.5mm

The parameters of the UVP measurements are shown in Table 2. As a result, 1031 two-dimensional velocity vectors were obtained by synthesizing the velocity vectors from the measurement results on the measurement lines of each UVP measurement. The weighted histograms on the x and y axes were obtained by weighting the intersection points of the obtained two-dimensional velocity vectors by the product of the magnitudes of the vectors.

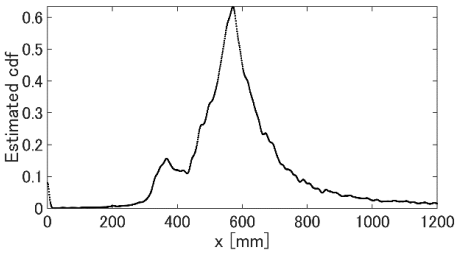

(a) x-axis

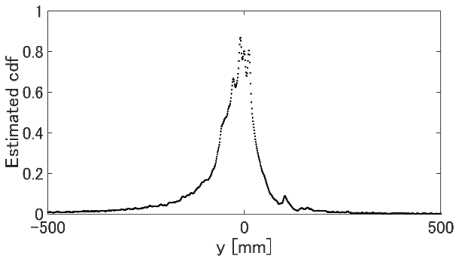

(b) y-axis

Fig. 2 Results of localization and Robot calculation

Kernel density estimation was performed on this histogram. We then normalized the overall probability to obtain the estimated establishment density for each axis. The results are shown in Figure 2. While the actual leakage points were $x = 600$ mm, $y = -13$ mm, the estimated leakage points obtained from the probability density estimation were $x = 570 \pm 20$ mm, $y = -10 \pm 10$ mm.

6. Summary

In this study, a basic study of an underwater ultrasonic exploration system for decommissioning of nuclear reactors was conducted. Long-arm robots and underwater exploration robots used for decommissioning have a problem of low accuracy in position estimation. In addition, because of the high radiation environment in the reactor, the number of sensors that can be used is limited. Therefore, we developed a self-positioning system using a mechanical encoder with high radiation resistance and an ultrasonic sensor. In the experiment, it was confirmed that the self-position can be estimated with higher accuracy by using the ultrasonic distance measurement technique and correcting the error in the amount of movement.

In addition, we combined the results of the above self-position estimation with the flow mapping system using the UVP method and conducted a simulated leak location estimation experiment using an actual device. It is suggested that the rough location of the leak can be estimated by correcting the sensor position by self-position estimation and expressing the flow velocity measurement results as a weighted histogram.

Future work includes the development of a detailed in-vessel survey system by combining multi-dimensional UVP measurement and ultrasonic imaging technologies and a study of its applicability. In particular, since the in-vessel environment requires a three-dimensional measurement rather than a two-dimensional survey, we believe that extending the UVP method to three dimensions will enable fast and reliable measurements.

References

[1] Shi, Pengfei and Fan, Xinnan and Ni, Jianjun and Wang, Gengren, A detection and classification approach for underwater dam cracks, Structural Health Monitoring, 15 (2016), 541-554.

[2] Meinhart, Carl D and Wereley, Steve T and Santiago, Juan G, PIV measurements of a microchannel flow, Experiments in fluids, 27 (1999), 414-419.

[3] Larry S.beller, and Harry L.Brown, "Design and operation of the core topography data acquisition system for TMI-2, " EG and G Idago, Inc, Idaho Falls, USA, GEND-INF-012 (1984).

[4] Yasushi Takeda, "Development of an ultrasound velocity profile monitor", Nuclear Engineering and Design, 126, (1991), 277-284.

[5] P.J.Besl and N.D.Mckay, A Method of Registration of 3-D Shapes, IEEE Trans. On Pattern Analysis and Machine Intelligence(PAMI), 14 (1992), 239-256.

[6] Parzen, Emanuel, On estimation of a probability density function and mode, The annals of mathematical statistics, Vol. 33 (1962), 1065-1076.

[7] Endo, Gen and Horigome, Atsushi and Takata, Atsushi, Super dragon: a 10-m-long-coupled tendon-driven articulated manipulator , IEEE Robotics and Automation Letters,4 (2019), 934-941.

12 UVP applied for Doppler scanning of fruit-internal structures and its working principle

13th International Symposium on Ultrasonic Doppler Methods for Fluid Mechanics and Fluid Engineering
Zürich, Switzerland (13.-15. June 2021)

UVP applied for Doppler scanning of fruit-internal structures and its working principle

Yuichi Murai[1], Taiki Yoshida[2], Hyun Jin Park[1], and Yuji Tasaka[1]

[1] Laboratory for Flow Control, Hokkaido University, N13W8, Sapporo, Hokkaido, 060-8628, Japan
[2]National Institute of Advanced Industrial Science and Technology, Tsukuba Central 3, 1-1-1, Umezono, Tsukuba 305-8563, Japan

The Inner structures of fruits are visualized by UVP instrument, i.e. reflection signals of ultrasound pulse. A target is submerged in a rotating water container so that a single ultrasonic transducer obtains echo intensity and Doppler velocity profiles as a function of rotating angle. By integrating the echo and Doppler signals over several rotations, the inner structures are successfully reconstructed as two-dimensional scanned distributions. While echo intensity measures stiffness of a target surface, Doppler image captures the inner structure with superficial phase shift that occurs due to moving acoustic property. We examine the applicability of the method to a kiwi, an apple, and a tomato, and find that gas cavities, solid-state seeds, and liquid-state portions inside these fruits being visualized.

Keywords: Pulse Doppler method, Doppler imaging, Fruit, Non-destructive diagnosis, Food industry

1. Introduction

Owing to the increasing worldwide consumer demand for high-quality fresh fruit, rapid evaluations of the maturity and quality of fresh fruits require a breakthrough in the development of a nondestructive, reliable, and noninvasive methodology. Sensing the inner structures of fruits together with evaluating the pulp hardness is important to this purpose. In the field of food engineering, sensing techniques have been developed using ultrasonic waves, magnetic resonance imaging (MRI)[1-3], computed tomography (CT)[4-5], optical coherence tomography (OCT) [6-8], and a laser Doppler vibrometer (LDV)[9]. MRI measurement systems require a huge facility to obtain a visualized image, and they may, therefore, not be suited to practical use. For the same reason, CT using X-rays should be disregarded as an option. OCT can realize higher spatial resolution of $O(10\mu m)$ adopting near-infrared radiation; however, the maximum transmitting distance of the radiation is limited to $O(1mm)$ in the application to botanical tissues. The LDV can estimate the hardness of pulps obtained by minute vibrations, and is a point measurement system. Thus, only the local point of the target can be estimated. Mizrach[10-12] reported an evaluation method for determining fruit tissue properties using a high-power and low-frequency ultrasound system. The system, however, determines the properties usually from a single measurement point and increasing the number of measurement points requires additional pairs of an ultrasonic emitter and receiver. Generally, fruit pulps have heterogeneous tissues, such as parenchyma cells, fiber cells, and stone cells, which have different properties owing to differences in fiber orientation and moisture content. In these cells of fruit and vegetables, which have an inhomogeneous microstructure, the depression of ultrasonic propagations is higher than that in homogeneous media. Thus, a one-directional or one-point ultrasonic measurement may have obvious disadvantages. The development of the multidirectional sensing of fruit properties in a simple and convenient way is desirable.

To realize the multidirectional sensing of inner structures of fresh fruit using the UVP, a rotating cylinder system is used on the basis of our understanding of ultrasonic spinning rheometry[13], where the test fruit is rotated by a cylindrical vessel and passes through a single ultrasonic propagation line. This realizes multiple sensing lines for the test fruit without using multiple sensors or rotating a sensor. To recognize inner structures, the Doppler velocity is used in addition to basic echo intensity information. The Doppler velocity is obtained as the velocity of ultrasonic reflection particles dispersed in fluid media, and it reflects local acoustic characteristics. Murai et al.[14] found that there are pseudo-low Doppler velocity regions near the interfaces of bubbles flowing in fluid media because of the interference of ultrasonic waves around the interface. In our previous paper (Yoshida et al.[15]), we we investigated the feasibility of applying the UVP to the visualization of inner structures of fresh fruit, especially O (mm) in size comparable to the wavelength of the ultrasonic wave. This was termed ultrasonic Doppler–echo visualization.

In the present paper, working principle of the ultrasonic visualization is revisited. Points of investigation are (1) how the two-dimensional inner structures can be reconstructed by a single path of ultrasound pulse, (a) what the echo intensity profile means and (2) why Doppler velocity profile corresponds well to the inner structure of a fruit that is mostly in solid state. Namely, we purpose to understand the working principle od the Doppler-echo visualization technique while visualization always works properly for various types of fruits.

2. Measurement Method

2.1 Target of Visualization

As shown in Fig. 1, we chose (a) kiwi, (b) apple, and (c) tomato as a target of visualization. Kiwi is known as a fruit covered by a thick hard skin so that inner condition is hardly imaginable only by touching the surface. Apples involve gas cavities and relatively large seeds in the core. Tomato consists of liquid-state part and hard tissue in the core. In food industry, day-change of the inner structure, which is hardly visible from outside, needs to be monitored

to optimize forwarding time control for consumers. The visualization also helps with effective combination with other food materials such as bread and rice. For instance, tomato of thick skin with less gel parts is demanded for sandwiches producers for long lasting in sell.

(a) Kiwi (b) Apple (c) Tomato

Fig. 2 Target of ultrasonic visualization

2.2 System Configuration

Experiments were conducted in the open-top rotating cylinder made of acrylic resin shown in Fig. 2. The cylinder had an inner diameter of 145 mm (2R), height of 60 mm, and lateral-wall thickness of 2 mm. The cylinder was filled with a gelling suspension, test objects were put into the suspension to ensure incidence of the ultrasonic wave into objects, and the objects were placed at their initial positions.

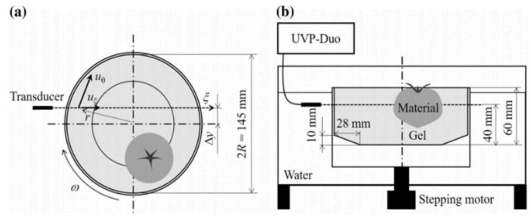

Fig. 2 Schematic diagram of ultrasonic scanning system; (a) top view, and (b) side view

The gelling suspension was made of montmorillonite powder (4.0 wt%) and NaCl solution (1.0 mol/L), and contained resin particles having a diameter of 100 μm to obtain echo information from the suspension. The cylinder was mounted at the center of a 1000 mm x 1000 mm water bath to maintain a uniform temperature at 25 C and to allow ultrasonic waves to propagate from outside the cylinder. Rotations of the cylinder were controlled by a stepping motor set with a given rotation speed X (= 2px/60). After all fluid in the cylinder reached a steady state of rigid rotation, repetitive ultrasonic emitting and receiving were performed using a UVP Duo monitor (Met-Flow S.A., Switzerland), and ultrasonic echo signals from test objects were processed using the same equipment to extract Doppler velocity information (termed the ‘‘Doppler velocity’’ hereafter). The UVP originally provided a spatiotemporal velocity distribution u(x, t) and corresponding echo intensity. To obtain the multidirectional Doppler velocity at inner structures of test objects, an ultrasonic transducer with a resonance frequency of 4 MHz and effective element diameter of 5 mm was mounted in the chamber. The corresponding measurement line was set 40 mm from the cylinder bottom with Δy = 15 mm.

Test objects were located inside the vessel at the off-center position as shown in Fig. 3. The sampling rate and spatial resolution determining the number of scanning lines were set at 66 ms and 0.74 mm during the measurement.

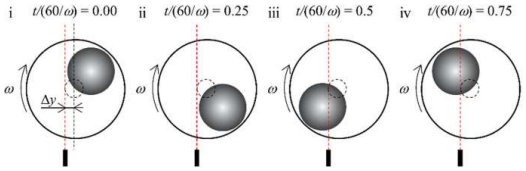

Fig. 3 Instantaneous position of a target object in rotating container relative to the ultrasound path

3. Results and Discussions

3.1 Space-time mapping

Fig. 4 shows the echo intensity distribution of a kiwi. The abscissa indicates the time, where the rotation period is 4.0 sec. The ordinate is the space from the transducer, where 0 stands for the inner wall of the cylindrical container. Red bands are the position of high echo intensity, which corresponds the surface of the kiwi. The other regions are mostly zero in average.

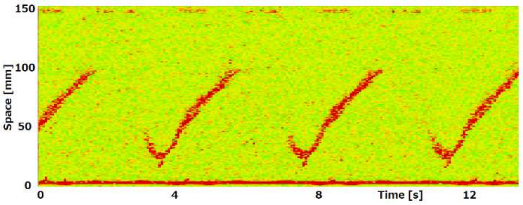

Fig. 4 Space-time map of echo intensity for a kiwi

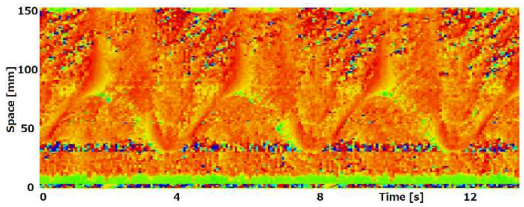

Fig. 5 Space-time map of Doppler velocity for a kiwi

Fig. 5 presents that of Doppler velocity distribution for the same kiwi, which is obtained simultaneously with echo intensity. Since the transducer is set slightly off-axis from the rotational center, Doppler velocity takes positive values inside the container. There can be seen a wavy pattern in the space-time map, which corresponds to the change in acoustic property between the inner and the

outer region of the kiwi.

3.2 Reconstruction of the inner structure

Coordinate conversion of the signal from the space-time map to spatial two-dimensional map is performed. The conversion is realized by replacing the time axis with rotation angle, based on constant angular velocity applied.

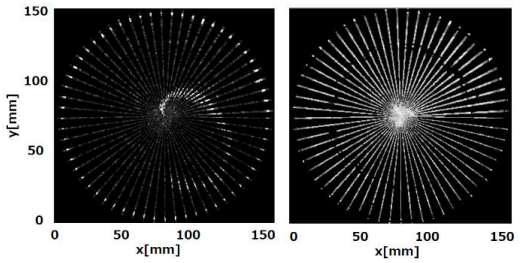

(a) Echo image (b) Doppler image

Fig. 6 One-cycle integration

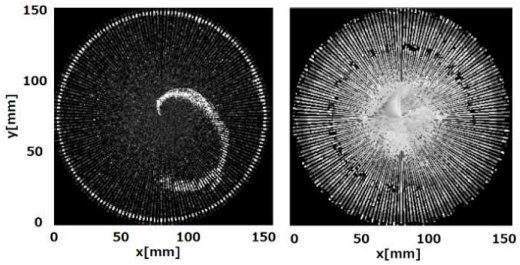

(a) Echo image (b) Doppler image

Fig. 7 Four-cycle integration

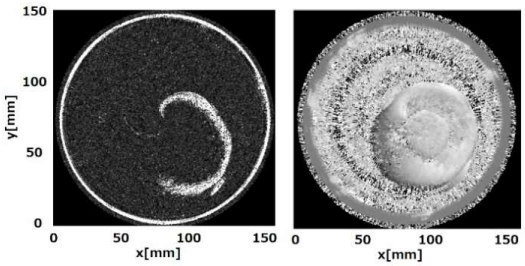

(a) Echo image (b) Doppler image

Fig. 8 Sixteen-cycle integration

Fig. 6 to Fig. 8 depict how the inner structure is reconstructed with increase in the integration of cycle number. In each figure, (a) is echo image and (b) is Doppler image. Echo image clearly indicate the outline of the fruit since the surface reflects the ultrasonic pulses the most. Doppler image has some pattern including the inner region of the fruit, indicating some organized pattern of the acoustic property inside the fruit. We examined how these images are reconstructed with increase in integration cycles as shown in Fig. 9.

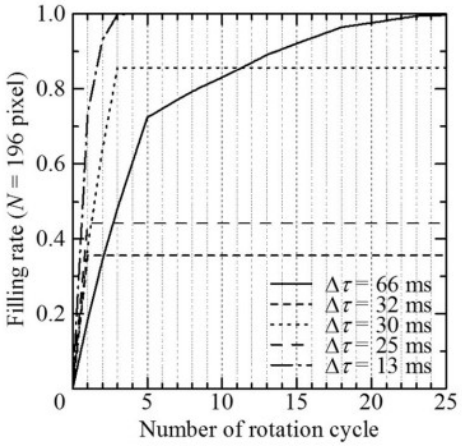

Fig. 9 Filling rate increased by integration cycles

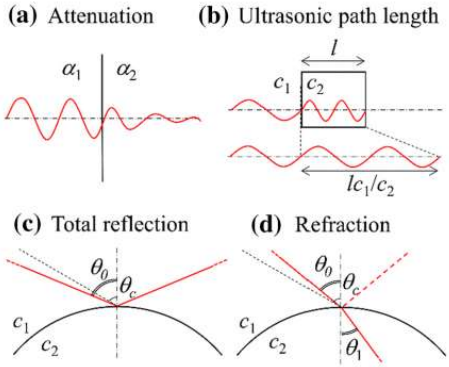

Fig. 10 Four patterns of ultrasonic pulse behavior

Fig. 10 illustrates four different patterns of ultrasonic pulse behavior, which explains the trend found in the echo image and Doppler image. For echo image, (a) attenuation inside the medium and (c) total reflection at the border of acoustic property govern the echo intensity. For Doppler image, (b) ultrasonic pulse length modified at the border and (d) refraction on the interface superficially shift the Doppler velocity, i.e. phase shift of the pulse.

3.3 Applications and interpretations

Fig. 11 compares the Doppler image of a kiwi between fresh and old states. By cutting it 10 days later, the old kiwi became soft containing gel-like part both in the near-skin layer and the core. The Doppler image of the old kiwi seems to have smoothened pattern. This is attributed to lowering of the acoustic impedance of the skin layer, expanding the pulse length.

Fig. 12 shows the case applied for a fresh apple. The echo image clearly figures out the shape of the surface. The Doppler image contains sharp fluctuation in the core region of the apple, which corresponds to the position of seeds and small gas cavity around them. In case of a

tomato, as shown in Fig. 13, gel-like region and the hard-core region are clearly visualized by the Doppler imaging. In fact, we also examined the present technique for pieces of pineapple, dry-fruit tips, and tapioca particles. This will be presented in slide-show presentation in the ISUD.

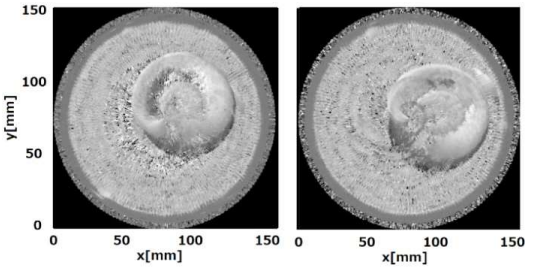

(a) Fresh kiwi (b) Old kiwi (10 days later)

Fig. 11 Comparison of Doppler images for a kiwi

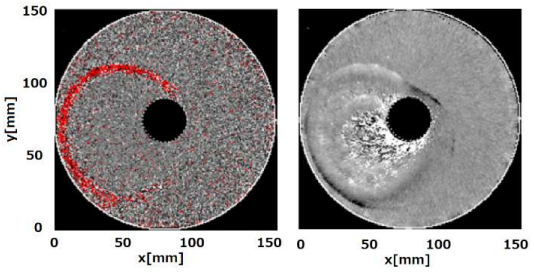

(a) Echo image (b) Doppler image

Fig. 12 Visualization of an apple

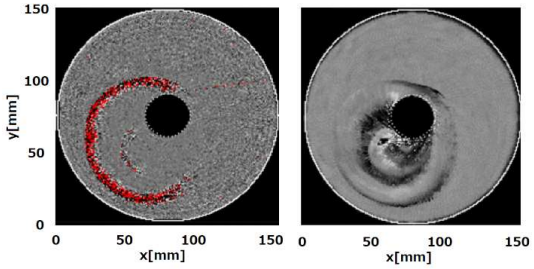

(a) Echo image (b) Doppler image

Fig. 13 Visualization of a tomato

4. Summary

Functions of UVP are applied for visualizing inner structure of fruits. Echo and Doppler information are converted into two-dimensional cross section image by cyclic intergation. Both type of the image well correspond to the real structure of the fruit up to a spatial resolution of *O*(1mm). In particular, Doppler image provides rich information on the innner structure, thanks to the phase shift analysis principle of the UVP system. The feasibility has been well demonstrated, however, this will need further understanding as the technique is used for quantitative visualization in future.

Acknowledgment

This study is financially supported by Robust Agriculture Research Center, Hokkaido University. The authors thank to Prof. Koseki and Mr. Teramura, Food Processing Engineering Laboratory, Faculty of Agriculture, Hokkaido University.

References

[1] Clarka CJ, Hockings PD, Joyce DC, Mazucco RA: Application of magnetic resonance imaging to pre- and post-harvest studies of fruits and vegetables. Postharvest Biol Technol 11(1) (1997), 1–21.

[2] Saltveit ME: Determining tomato fruit maturity with nondestructive in vivo nuclear magnetic resonance imaging. Postharvest Biol Technol 1(2) (1991), 153–159.

[3] Zhang L, Michael JM: Measurement and evaluation of tomato maturity using magnetic resonance imaging. Postharvest Biol Technol 67 (2012), 37–43.

[4] Brodersen CR, Lee EF, Choat B, Jansen S, Phillips RJ, Shackel, KA, McElrone AJ, Matthews MA: Automated analysis of three-dimensional xylem networks using high-resolution computed tomography. New Phytol 191(4) (2011), 1168–1179.

[5] Staedler YM, Masson D, Scho¨nenberger J: Plant tissues in 3D via X-ray tomography: simple contrasting methods allow high resolution imaging. PLoS One 8(9) (2013) e75295.

[6] Lee C, Lee SY, Kim JY, Jung HY, Kim J: Optical sensing method for screening disease in melon seeds by using optical coherence tomography. Sensors 11(10) (2011), 9467–9477.

[7] Oldenburg AL, Chenyang X, Boppart SA: Spectroscopic optical coherence tomography and microscopy. IEEE J Sel Top Quant 13(6) 8 (2007), 1629–1640.

[8] Verboven P, Nemeth A, Abera MK, Bongaers E, Daelemans D, Estrade P, Herremans E, Hertog M, Saeys W, Vanstreels E, Verlinden B, Leitner M, Nicolai B: Optical coherence tomography visualizes microstructure of apple peel. Postharvest Biol Technol 78 (2013), 123–132.

[9] Hosoya N, Mishima M, Kajiwara I, Maeda S: Non-destructive firmness assessment of apples using a non-contact laser excitation system based on a laser-induced plasma shock wave. Postharvest Biol Tec 128 (2017), 1–17.

[10] Mizrach A: Assessing plum fruit quality attributes with an ultrasonic method. Food Res Int 37(6) (2004), 627–631.

[11] Mizrach A: Nondestructive ultrasonic monitoring of tomato quality during shelf-life storage. Postharvest Biol Technol. 46(3) (2007), 271–274.

[12] Mizrach A: Ultrasonic technology for quality evaluation of fresh fruit and vegetables in pre- and postharvest processes. Postharvest Biol Technol 48(3) (2008), 315–330.

[13] Tasaka Y, Kimura T, Murai Y: Estimating the effective viscosity of bubble suspension in oscillatory shear flows by means of ultrasonic spinning rheometry. Exp Fluids 56(1) (2015), 1897.

[14] Murai Y, Fujii H, Tasaka Y, Takeda Y:Turbulent bubbly channel flow investigated by ultrasound velocity profiler. J Fluid Sci Technol 1(1) (2006), 12–23.

[15] Yoshida, T., Tasaka, Y., Park, H.J., Murai, Y.. Teramura, H., Koseki, S: Inner structure visualization of fresh fruits utilizing ultrasonic velocity profiler. Journal of Visualization, 21 (2017), 253-265.

16 Frequency Analysis of Water-Vegetable Oil Emulsion Produced by Taylor-Couette System with Small Aspect Ratio Using Ultrasonic Doppler and Attenuation Method

13th International Symposium on Ultrasonic Doppler Methods for Fluid Mechanics and Fluid Engineering
Zürich, Switzerland (13.-15. June 2021)

Frequency Analysis of Water-Vegetable Oil Emulsion Produced by Taylor-Couette System with Small Aspect Ratio Using Ultrasonic Doppler and Attenuation Method

Yoshihiko Oishi[1], Hideki Kawai[1], Daichi Sasayama[1], and Hiroshige Kikura[2]

[1] Dep. of Production Systems Engineering, Muroran Institute of Technology, 27-1 Mizumoto-cho, Muroran, Hokkaido 050-8585, Japan
[2] Lab. for Advanced Nuclear Energy, Tokyo Institute of Technology, 2-12-1 Ookayama, Meguro-ku, Tokyo 152-8550, Japan

The emulsification method is not only one of the potentially effective techniques to reduce fossil fuel consumption but also exhaust emission from diesel engines. Water-in-Oil (W/O) emulsified fuel is reported to reduce the emissions of NOx, SOx, CO and particulate matter (PM) caused by a decrease in combustion temperature and a micro explosion in combustion. However, the emulsified fuel shows non-Newtonian properties called pseudoplastic flow as water content ratio increases. Since a viscosity of pseudoplastic flow decreases with increasing shear rate, the W/O emulsified fuel causes clogging of fuel injector, decrease of combustion efficiency due to deterioration of fuel spray in high water content ratio. It is important to know a state of flow transition of the emulsified fuel in mixing conditions. In this study, we evaluated W/O emulsified fuels using ultrasonic measurement, produced 10 %, 20 %, 30 % water-vegetable oil emulsion at 300-800 rpm with a Taylor-Couette reactor. We measured velocity profiles and attenuation of echo at every 100 rpm utilizing the ultrasonic Doppler method and echo intensity measurement. As a result, transitions of the velocity profiles and the echo attenuation were different in each water content ratio.

Keywords: Emulsified fuel, Ultrasonic measurement, Taylor-Couette flow

1. Introduction

Emulsified fuel is a type of emulsion in which water and fuel oil are emulsified and mixed, causing a micro explosion when the superheat limit of water is exceeded during combustion. Emulsified fuel is researched mainly as an alternative fuel for diesel engines and marine boilers [1] . Mixing with water not only reduces the fuel consumption rate but also reduces the carbon monoxide (CO) and particulate matter (PM) emissions because the micro explosion causes the contact area between the fuel droplets and air to increase, approaching complete combustion. In addition, there is a report that NO_X emissions are reduced due to a decrease in combustion temperature due to the evaporation of water contained in the fuel [2]. However, if water and fuel oil are used in a phase-separated state, there are problems such as failure of the internal combustion engine and the effect of reducing exhaust gas due to micro explosion cannot be obtained. Therefore, the stabilization of fuel is an important issue for practical use. The stability of emulsified fuel is obtained by preventing creaming, in which water droplets in the dispersed phase settle and separate into layers due to the density difference from fuel oil in the continuous phase, and aggregation and coalescence of droplets adhering to each other. In this study, we focused on measurement using the properties of ultrasonic waves. Ashrafi et al. [3] and Yektapour et al. [4] are studying pseudoplastic fluids in rotating flow and are proceeding with physical elucidation. Ultrasonic has the property of being reflected and attenuated at the interface of media with different acoustic impedances and is used to measure the volume concentration of suspended particles [5]. When these methods are applied to emulsions, the particle diameter does not affect the number revolutions in the case of solids but in the case of droplets, it is expected that the diameter changes because of the shear changes with the number of revolutions. In this study, the droplet diameter of the emulsion was measured by ultrasonic attenuation to evaluate the stability of the emulsified fuel. The challenge for practical use as an emulsion fuel generator is to produce an emulsion that does not separate for a long time. If the TCF stirrer can be mounted directly on the vehicle body, the emulsion can be injected into the internal combustion engine without separation immediately after stirring. However, it is difficult to produce an emulsion with a fine droplet diameter by mechanical stirring such as TCF stirring as compared with the membrane emulsification method. Therefore, we focused on the production of emulsion by a low aspect ratio TCF stirrer that can be mounted directly.

2. Experimental setup and conditions

Figure 1 shows a Taylor-Couette Flow (TCF) generator. The boundary conditions of the equipment were fixed at the upper and lower ends. The dimensions of each part of the coaxial double cylindrical container were as follows: inner cylinder radius R_{in} = 50 mm, outer cylinder radius R_{out} = 75 mm, and height H = 75 mm. From this, the gap between the inner cylinders was set to $d = R_{out} - R_{in}$ = 25 mm and the radius ratio $\eta = R_{in} / R_{out}$ = 0.667. The aspect ratio becomes low when the aspect ratio $\Gamma = H / d$ = 3. The rotation speed can be set in the range between 10 and 800 rpm by a DC servo motor mounted on the inner cylinder and set by the driver. The rotation speed can be changed in 1 rpm increments by turning the driver dial. An ultrasonic

transducer (TDX) that emits ultrasonic waves was installed at a position 12.5 mm from the outer circumference of the inner cylinder at the upper end of the device, and the axial ultrasonic echo intensity obtained from the emulsion was measured. Table 1 shows the experimental conditions of this experiment. In this experiment, an emulsion consisting rapeseed oil and ion exchanged water was used as the working fluid. The water content ratio is 10, 20 and 30 %. The working fluid temperature was controlled at 20 ℃ using a thermostat.

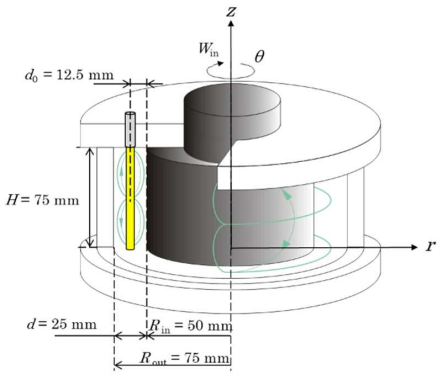

Figure 1: Schematic diagram of Taylor-Couette Flow

Table 1: Experimental conditions

Boundary conditions	Fixed
Water content ratio	10 , 20, 30 Vol. %
Rotation speed	300 – 800 rpm
Rapeseed Oil density	920 kg/m^3
Water density	998 kg/m^3
Rapeseed oil sound velocity	1482 m/s
Water sound velocity	1482 m/s
Temperature	20 ℃
Basic frequency	8 MHz
Gain	40 mV/Div

3. Methods

The working fluid was ion exchanged water and rapeseed oil. After filling in the TCF generator, the emulsion was formed by rotating the initial rotation speed from 300 rpm. The rotation speed is set every 100 rpm from the initial rotation speed, and under each condition, ultrasonic measurement is performed after stirring for 20 minutes. The resulting echo is shown in figure 2(a). The vertical axis shows the echo intensity, and the horizontal axis shows the normalized distance z/H by dividing the distance from TDX by the device height H = 75 mm. The region with a normalized distance z/H = 0.0 to 0.1 shown in figure 2(a) was excluded because it is a near field where the sound pressure is unstable [7]. Also, the normalized distance z/H = 0.5 or later was excluded because it is difficult to confirm the echo due to the effect of diffusion attenuation. Figure 2(b) shows the echo intensity waveform obtained by averaging the measured echo data for 30 times and taking the absolute value. The vertical axis shows the echo intensity, and the horizontal axis shows the normalized distance z/H. Ultrasonic attenuation is defined as a distance-dependent exponential function by Weser et al.[8] as follows,

$$I = \beta e^{-\alpha z/H} \quad (1)$$

where, if the attenuation coefficient is α and the dimensionless distance from TDX is z/H.

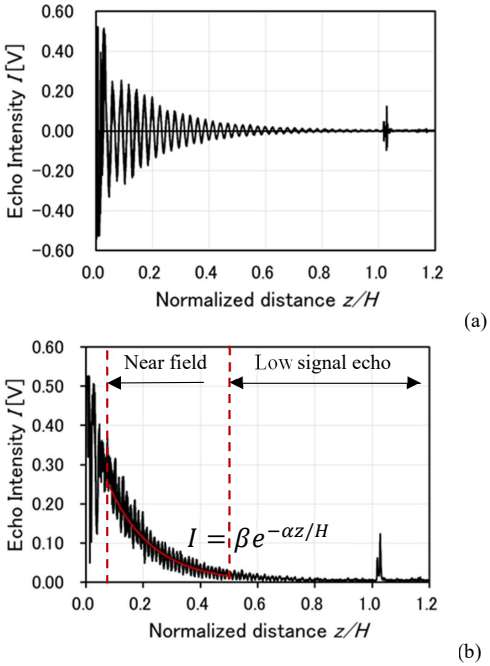

Figure 2: Typical echo from a stirred emulsion (a) raw echo signal, (b) absolute and averaged echo calculated for 30 single measurements

4. Results and discussion

Figure 3(a) shows the measurement results of the ultrasonic decrement coefficient for water content ratio 10%, 20%, and 30% emulsions. From figure 3(a), it is considered that there is no correlation between the water content ratio and the ultrasonic decrement coefficient. However, looking at the decrement coefficient for each rotation speed of inner cylinder, the decrement coefficient increased as the rotation speed increased. Figure 3(b) shows a graph in which the horizontal axis of figure 3(a) is the number of revolutions. As can be seen from figure 3(b), the decrement coefficient increases with increasing rotational speed at any water content ratio. In addition, since the process of increasing the decrement coefficient is different at a water content ratio of 30%, it is expected that the flow state will be different at a water content ratio of 30% than at 10 and 20%. Figure 4, 5 and 6 show the results of color plot display of time-series velocity distribution

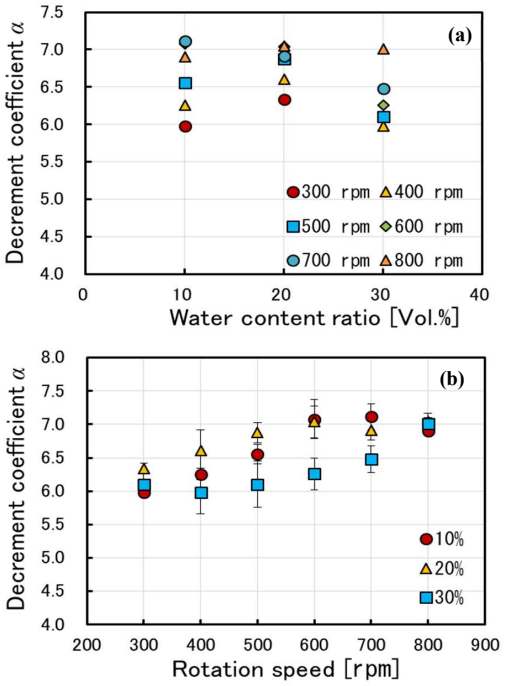

Figure 3: Decrement coefficient in each water content ratio and rotation speed, (a) α versus water content ratio, (b) α versus rotation speed

data obtained by measuring the water content ratio 10, 20 and 30% emulsions using an ultrasonic velocity profiler (UVP). In these figures, the vertical axis is the normalized distance of each measurement position z at the height H of the entire measurement section, and the horizontal axis is the time. z/H = 0.00 indicates the device upper plate (TDX installation position), and z/H = 0.50 indicates the device intermediate position. The figure shows the velocity component in the axial direction, the velocity from the bottom plate to the top plate of the device is positive, and the color plot shows the magnitude of the velocity. Compering figure 4, 5, and 6, the 10 and 20% emulsions have similar flow velocity distribution oscillations at 500 rpm and 600 rpm. In the case of Newtonian fluid, the low aspect ratio flow is TVF below Re = 700 and WVF with one fundamental frequency from Re = 700 to 1000. When Re = 1000 or more, modulated wavy vortex flow (MWVF) has multiple fundamental frequencies. Looking at the velocity distributions from Fig. 4 to 6, there is a flow that oscillates periodically at Re = 900 for 10% emulsion and Re = 700 for 20% emulsion. This is in the region of wavy vortex flow (WVF) under the conditions at this time, but the magnitude and period of the amplitude are qualitatively consistent with Re = 1100 in the Newtonian fluid. Therefore, the flow was the same as in the high viscosity region with a low Reynolds number. The results of frequency analysis are shown Figures 5-7. Figures show water content of 10%, water content of 20%, and water content of 30%. The x-axis is f^*, the y-axis is Re, and the z-axis is the frequency component. The power spectrum

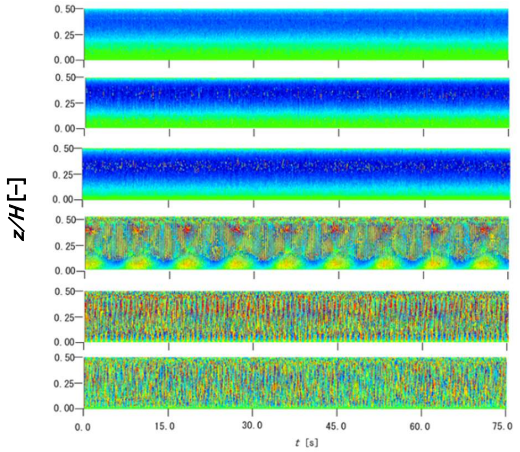

Figure 4: Time development velocity profile at 10% W/O emulsion using UVP

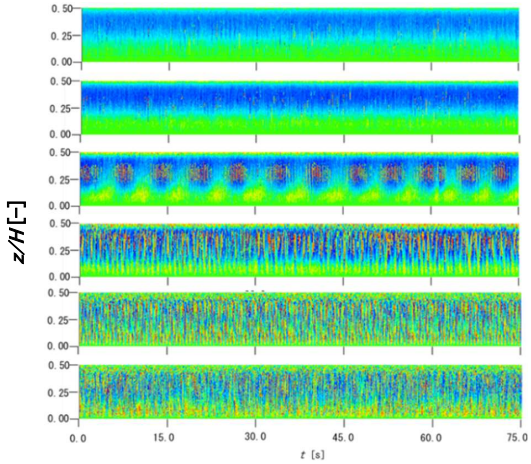

Figure 5: Time development velocity profile at 20% W/O emulsion using UVP

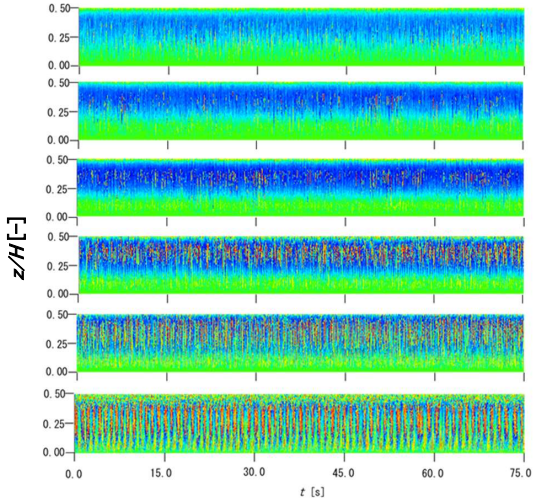

Figure 6: Time development velocity profile at 30% W/O emulsion using UVP

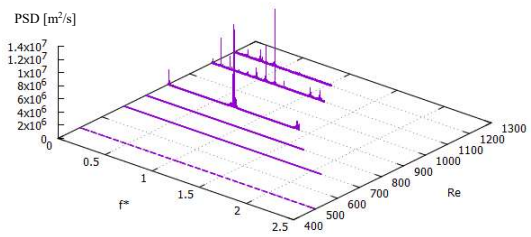

Figure 7: Space-averaged power spectrum density of 10% emulsion

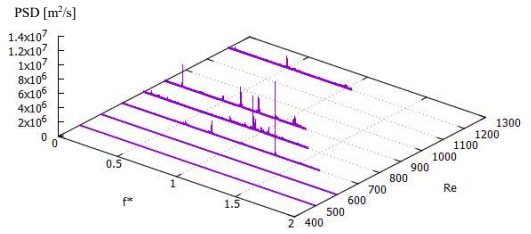

Figure 8: Space-averaged power spectrum density of 20% emulsion

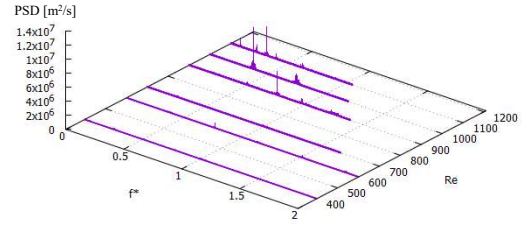

Figure 9: Space-averaged power spectrum density of 30% emulsion

density (PSD) [m^2/s], which indicates the strength of, is shown. As a result of Figure 5, it is said that a wave Taylor vortex flow in which the cell vibrates periodically is generated at any water content [7], and the peak of the spectrum is detected from Re = 700 to 1000. In Figs. 5-7, Re = 900, peaks are detected near f^* = 0.7 at water content of 10 and 30%, but f^* = 0.15 and 0.65 at 20%, 0.8 and multiple peaks were confirmed. Emulsion fuel becomes more viscous as the water content increases and exhibits pseudoplastic flow [8]. In the case of pseudo-plastic flow, the viscosity of the fluid decreases as the shear stress increases. Therefore, in an emulsion with a water content of 20%, the decrease in viscosity due to the pseudoplastic flow state is greater than the increase in viscosity due to the increase in water content. It is considered that the effect was strong, Re was higher than that of the water content of 10 and 30% emulsion, and the fluid state was different. In the low aspect ratio TCF using Newtonian fluid as the working fluid, the spectrum was observed near f^* = 2.0 from Re = 700 to 1000. On the other hand, the spectrum peaks are seen at f^* = 0.70 for the 10% emulsion, f^* = 0.15, 0.65, 0.80, 0.93, 1.30 for the 20% emulsion, and f^* = 0.38 and 0.76 for the 30% emulsion. It has been reported that the vorticity is changed compared to non-Newtonian fluids and Newtonian fluids [9]. From the above, it is considered that when a non-Newtonian fluid such as an emulsion is used as a working fluid, a Taylor vortex vibration different from that of the Newtonian fluid is generated. Comparing the cases of Newtonian fluid and pseudoplastic fluid from these results, it is considered that the pseudoplastic fluid vibrates at a lower frequency even if it is the same WVF. In addition, when comparing the emulsion Re900, a single peak was detected in the 10% emulsion and the 30% emulsion, but multiple peaks were confirmed in 20%. It is considered that the decrease in viscosity during stirring of the 20% emulsion had a stronger effect than the increase in viscosity due to the increase in water content, and the Reynolds number increased because it became a fluid state like MWVF.

5. Summary

As a result of measuring the ultrasonic attenuaion coefficient at the water content ratio of 10, 20 and 30%, the following findings were obtained.

- No change was observed in the ultrasonic decrement coefficient due to the change in water content ratio.
- The ultrasonic decrement coefficient tended to increase as the inner cylinder rotation speed increased.
- According to the velocity distribution, in the 10 and 20% W/O emulsions, the oscillation of the flow velocity distribution occurs at 600 rpm and 500 rpm, and the cycle is similar, but in the 30% W/O emulsion, such oscillation was not appeared.

References

[1] Nadeem M, *et al*.: Diesel engine performance and emission evaluation using emulsified fuels stabilized by conventional and gemini surfactants, Fuel, 85 (2006), 2111-2119.
[2] Alahmer A, *et al*.: Engine performance using emulsified diesel fuel, Energy conversion and management, 51, (2010), 1708-1713.
[3] Ashrafi N & Hazbavi A: Flow pattern and stability of pseudoplastic axial Taylor-Couette flow, International Journal of Non-Liner Mechanics, Vol. 47, (2012), 905-917.
[4] Yektapour M & Ashrafi N: Rotational and axial flow of pseudoplastic fluids, Mech Time-Depend Mater, 23, (2019), 173-192.
[5] Hitomi J, *et al*.: Measurement of the inner structure of turbidity currents by ultrasound velocity profiling, International Journal of Multiphase Flow, 136, (2021), 103540.
[6] Kazys R, *et al*.: Ultrasonic monitoring of variations in dust concentration in a powder classifier, Powder Technology, 381, (2021), 392-400.
[7] Takeda Y: Ultrasonic Doppler Velocity Profiler for Fluid Flow, Springer, (2012), 30-33.
[8] Weser R, *et al*.: Particle Characterization in highly concentrated dispersions using ultrasound backscattering method, Ultrasonics, 53, (2013), 706-716.
[9] Cagney N, & Balabani S: Taylor-Couette flow of shear-thinning fluids, Physics of Fluids, 31, (2019), 053102.

17 Measurement of size and velocity of rising bubbles by a vector UVP

13th International Symposium on Ultrasonic Doppler Methods for Fluid Mechanics and Fluid Engineering
Zürich, Switzerland (13.-15. June 2021)

Measurement of size and velocity of rising bubbles by a vector UVP

Hyun Jin Park, Shintaro Akasaka, Yuji Tasaka, Yuichi Murai
Faculty Engineering, Hokkaido University, N13-W8, Kita-ku, Sapporo 060-8628, Japan

We developed a vector UVP, composed of one emitter and two receivers, to measure the rising speed and the size of bubbles. A traditional UVP having one emitter and one receiver measures just a single velocity component and therefore it cannot exact the motion of rising bubbles moving three-dimensionally in the pipe. For example, to measure their rising velocity from a UVP installed on the outside wall of the pipe, we have to obtain at least two-dimensional velocity vector components of them. Our novel UVP can measure profiles with two-dimensional velocity vectors. As a demonstration, we installed the vector UVP to emit ultrasonic pulses horizontally and measured vertically rising bubbles in the still water. And the shape of bubbles was measured using the echo intensity obtained when calculating the Doppler frequency from echo signals from two receivers. Then, the size of bubbles was estimated from the rising velocity and the shape. From the comparison with optical visualizations, it is confirmed that the velocity was 15% underestimated and the size was corresponded with that of the visualizaiton, respectively.

Keywords: Bubble, Echography, Vector UVP

1. Introduction

Bubbles rising in a pipe flow can modify characteristics of the flow such as heat and momentum transfer coefficients, and therefore monitoring of bubbles' characteristics is required to control fluid machines. In most cases, invasive type measurement methods are not recommended since they give some damages to the pipe when their installation. Therefore, non-invasive type measurement methods are required for the monitoring [1]. Ultrasonic measurement techniques are one of them and several techniques have been developed to suit their targets of the measurement [2–5]. In many targets, especially, we focused on techniques to measure the rising velocity and the size of bubbles in the liquid. They are important parameters for estimating the void fraction and the drift velocity in two-phase flows. The simplest technique to obtain the rising velocity is the use of one transducer (TDX) of an ultrasonic velocity profiler (UVP) installed diagonally to the gravity direction [5]. Since it is assumed that rising bubbles have only one velocity component in this technique, if bubbles float vertically without any zigzag motion, we can measure their rising velocity correctly. However, if they move horizontally a bit, measured velocity includes a lot of errors causing the horizontal motion. In most cases, bubbles float with zigzag motions caused by their wake and the turbulence in a liquid-phase flow around of bubbles. To measure the rising velocity correctly, it is required to distinguish each velocity component by measuring them simultaneously. A vector UVP possible the simultaneous measurement is one of its solutions [7–9]. It is, however, not widely used for the measurement because many types of vector UVP generally use multiple receivers particularly designed for the UVP. TDXs using for the receiver have a small active area to keep highly the precision of angle θ been by ultrasonic waves reflected at the bubble. In this paper, we designed a vector UPV with typical type TDXs, used for a normal UVP and not designed for the vector UVP, by limiting measurable length from the TDX. Also it was estimated characteristics of rising bubbles by the new vector UVP.

2. Experimental method

2.1 Experimental setup

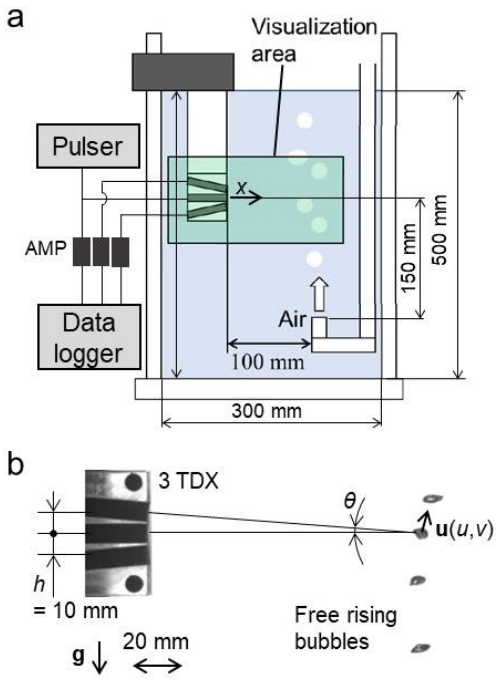

Figure 1: Experimental setup; (a) schematic diagram and (b) a snap picture of the visualization area.

The measurement of bubbles' characteristics by a vector UVP was performed in a water tank with an air tube installed at its bottom to inject bubbles as shown in Fig. 1. Three TDXs (TX4-5-8-40, Met-Flow) connected with three amps (PR-60BP, Japan-probe) and a data logger (PicoScope 3000, Pico Technology) were installed at 100

mm horizontally and 150 mm vertically away from the injector. Only the center TDX was set horizontally and connected with a pulser (JPR-600, Japan-probe) to use as the emitter. The others were set with ± 5° to the horizontal direction and vertically 10 mm away from the center TDX to make be toward a place where bubbles were passing on the measurement line; i.e, the place was 100–120 mm horizontally away from the center TDX in the experiment. The data logger recorded echo signals received from TDXs with a significantly high sampling frequency, 62.5 MHz, to resolve ultrasonic waves with 4 MHz in the basic frequency f_0. Detailed information on the setting parameter of each instrument is listed in Table 1.

Table 1: Parameters for the vector UVP.

Transducer (TX4-5-8-40, Met-Flow)		
basic frequency (f_0)	4	MHz
active diameter	5	mm
divergence half-angle	2.2	°
distance between TDXs	10	mm
angle of receiving TDX	± 5	°
Pulser (JPR-600, Japan-probe)		
cycle of ultrasonic pulse	4	
pulse repetition frequency	5	kHz
emission voltage	150	V
Data logger (PicoScope 3000, Pico Technology)		
sampling frequency	62.5	MHz
recording range of voltage	±0.2	V
resolution of voltage	12	bit

2.2 Conditions of bubbles

To verify the accuracy of rising velocity and size of bubbles obtained by the UVP, the optical visualization was performed simultaneously by a camera (FASTCAM Mini AX-50, Photron) as shown in Fig. 1(b). Results of the visualization are in Table 2, where the bubble size d_0 is the equivalent bubble diameter calculated from its projection area.

Table 2: bubble characteristics obtained by the optical visualization.

	average	standard deviation
Bubble size (d_o) [mm]	5.72	0.36
Rising speed (v_o) [m/s]	0.33	0.03

3. Signal processing

2.1 Detection of bubbles

Figure 2 shows echo signals obtained by a receiver. In the experiment, since there was no object possible to reflect ultrasonic pulses excepting bubbles, if there is a high amplitude in the echo signal, it indicates a bubble. At first, the intensity and the phase of echo pulses was estimated

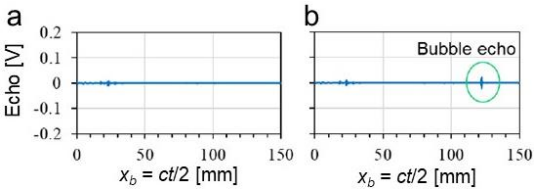

Figure 2: Received echo signals; (a) without bubbles and (b) with bubbles.

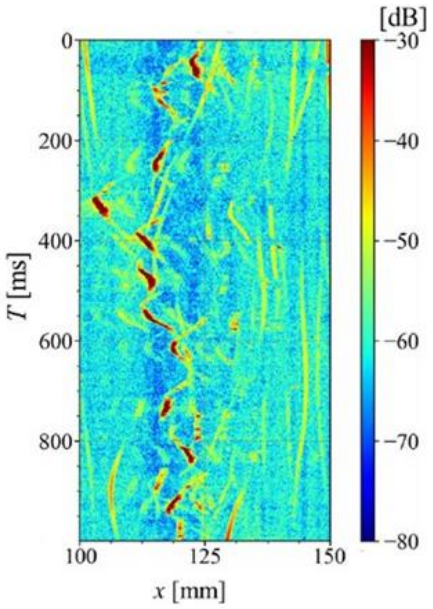

Figure 3: Averaged echo amplitude received by two receivers.

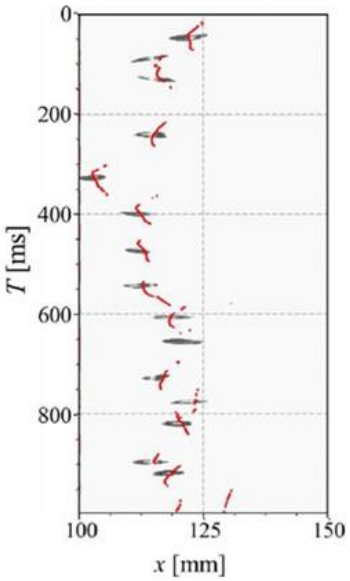

Figure 4: Time-line image at ultrasonic measurement line, where red plots show bubble surface detected by the averaged echo in Fig. 3.

the intensity and the phase of echo pulses was estimated from original echo signals by a demodulation with the Hilbert transform [10]. To detect bubbles from the signal, we decided a threshold value, 99 percentages outside intensity of echo without the bubble condition, and judged as the bubble interface when averaged echo intensities obtained from two receivers is over the threshold. Figures 3 and 4 show time-line images of averaged echo intensity calculated by the demodulation and bubbles visualized optically by the camera. In Fig. 4, positions of the intensity higher than the threshold intensity are expressed as red plots and therefore they mean the left side interface of bubbles. Comparing bubbles and red plots in the figure, it is confirmed that this detection method is working well although acoustically detected bubbles are larger than optically visualized bubbles. The long existence time of bubbles estimated by the vector UVP is caused by a high echo intensity on the gas–liquid interface of bubbles. This high intensity occurs even if they block a part of the ultrasonic beam with a thick diameter, over 5 mm in the experiment, as shown in Fig. 5 and therefore bubbles are detected by the UVP before they reach the center axis of the beam.

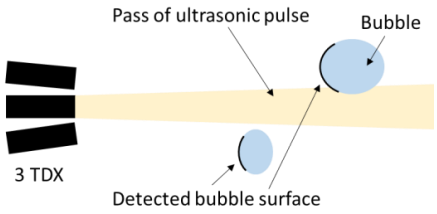

Figure 5: Ultrasonic pulse reflection at bubble surface toward to TDX, where the pulse reached at the surface on upper and bottom side of bubbles cannot return to receiver because of its shallow reflect angle.

2.2 Estimation of rising velocity

To obtain rising velocities of the bubble, at first, the Doppler shift frequency f_D should be estimated from the echo signal. Already many estimation methods were suggested and, here, the Doppler spectra analysis using DFT was employed for the estimation [11]. And then, the rising velocity v was calculated by Eq. (1).

$$v = \frac{c(f_{D1} + f_{D2})}{2 f_0 \sin\theta} = \frac{h(f_{D1} + f_{D2})}{f_0 t_b} \qquad (1)$$

Here, c, h and θ are the speed of sound, the distance between transducers and the angle in the pass of ultrasound as shown in Fig. 1. The result of v is shown in Fig. 6. upper-ward and down-ward velocities exist in the acoustically detected bubble surface, but there are almost zero velocities in the other areas. It is supposed that down-ward velocities in the surface is actually upper-ward velocities faster than the maximum velocity which UVP is possible to measure. In the UVP measurement, plus and minus signs is changed the velocity is higher than the maximum measurable velocity of UVP. The rising velocity of individual bubbles was defined as the average of upper-ward velocities on surface of each bubble.

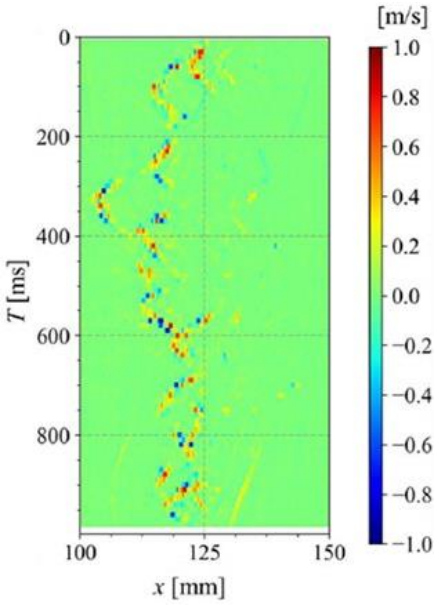

Figure 6: upper-ward velocity component from the vector UVP.

2.3 Estimation of bubble size

We already know the existence time of each bubble passing on the ultrasonic beam and its rising velocity and therefore the simplest method to estimate bubble size is the multiplication of them. But it includes some errors caused by the beam thickness and non-detected surface on upper and bottom area of bubbles as shown in Fig. 5. An error caused by the beam thickness is possible to reduce its effects on the bubble size estimation because the thickness and the rising velocity are knowing values. However, it is hard to reduce the effects caused by the non-detected surface because we do not have information of bubble shape. Therefore, we tried to estimate the bubble size from shape of a part of the interface on its side area by assuming that all bubbles had elliptical shapes. The elliptical shape was fitted on the part of detected interface. In the fitting, unknown parameters were the temporal-spatio center positions, major and minor diameters of the ellipse, and its tilted angle. Because of five unknown parameters, the fitting was performed only when more than four plots of the detected surface existed continuously in the time. Bubbles composed with less than five plots were treated as the error and deleted in the measurement result. The size of each bubble was calculated as the equivalent diameter from the major and minor diameter of its fitted ellipse.

5. Evaluation of the measurement

Averages of the bubble size and the rising velocity measurend are in Table 2. Comparing with results of the optical visualizaiton in Table 1, the bubble size has the

same value and the rising velocity is 0.05 m/s, 15.1%, lower in the vector UVP measurement, respectivley. Although the size estimation by the UVP is well matched with that of the visualization, the standard deviation of size becomes 4.6 times larger. To understand why the gap occurs, probability density funtions (PDF) of the bubble size are shown in Fig. 7. Although the bubble size is actually in 5–6.5 mm, the size estimation by vector UVP shows it is in 3–9.5 mm. It is supposed that the large standard deviation is caused by the shape of bubbles. In the estimation, we assumed that the shape of bubbles was elliptical. As shown in Fig. 1(b), however, bubbles did not have elliptical shapes, because their size was significantly large and bubbles did not maintain elliptical shapes by the surface tension.

Table 2: bubble characteristics obtained by the vector UVP.

	average	standard deviation
Bubble size (d_u) [mm]	5.72	1.67
Rising speed (v_u) [m/s]	0.28	0.40

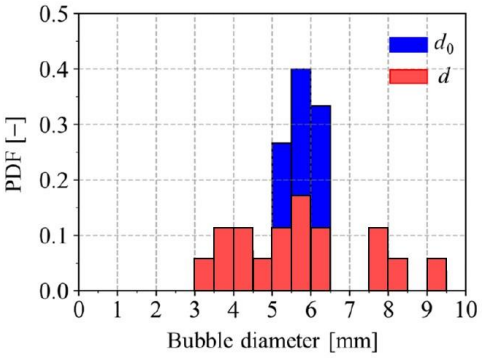

Figure 7: Probability density funtions of the bubble size.

5. Summary

We tried to estimate the size and rising velocity of floating bubbles in water by a vector UVP composed with three typical transducers using a normal UVP ; one transder was working only as emitter and the others were wokinig as recivers. This vector UVP allows use of typical transducers as a reciver by giving a limitaion of measuremnt area and an angle to transducers to face the measurement area. The bubble surface was detected using strong echo from the surface. And the rising velocity of a bubble was defined as an average value of vertical velocities located in the detected bubble surface. This rising velocity was about 15% underestimated compring with the actual rising velocity. The bubble size was estimated using a fitting of ellipse defined from a shape of the detected surface and the rising velocity. An average of bubble size obtined from the UVP was well matched with that of their actual sizes although the standard deviation of sizes were 4.6 times overestimated by this measutement because the shape of bubbles were not keeping elliptical shapes in the experiment. It is supposed that our size estimation method provies better results in a case with small bubbles keeping elliptical shapes. In a case with large bubbles like as this experiment, however, it is required to develop a different method to estimate the bubble size.

References

[1] Hitomi J, et al.: Ultrasound Flow-Monitoring and Flow-Metering of Air – Oil – Water Three-Layer Pipe Flows, IEEE Access, 5 (2017), 15021–15029.
[2] Murakawa H, et al.: Application of ultrasonic multi-wave method for two-phase bubbly and slug flows, Flow Meas. Instrum. 19 (2008), 205–213.
[3] Murai Y, et al., Development of an ultrasonic void fraction profiler, Meas. Sci. Technol., 20 (2009), 114003.
[4] Park HJ, et al.: Ultrasonic pulse echography for bubbles traveling in the proximity of a wall, Meas. Sci. Technol., 26 (2015), 125301.
[5] Park HJ, et al.: Monitoring of Void Fraction and Bubble Size in Narrow-channel Bubbly-flows using Ultrasonic Pulses with A Super Bubble-resonant Frequency, IEEE Sensors J., 21 (2021), 273–283.
[6] Aritomi M, et al., Measurement System of Bubbly Flow Using Ultrasonic Velocity Profile Monitor and Video Data Processing Unit, J. Nucl. Sci. Techol., 33 (1996), 915–923.
[7] Hunther D and Lemmin U, A constant-beam-width transducer for 3D acoustic Doppler profile 48 measurements in open channel flows, Meas. Sci. Technol., 9 (1998), 1706–1714.
[8] Batsaikhan M, et al., isualisation of air–water bubbly column flow using array Ultrasonic Velocity Profiler, Theor. Appl. Mech. Lett., 6 (2017), 379–385.
[9] Wongsaroj W, et al.: 2D velocity vector profile measurement on bubbly flow using ultrasonic technique, Mech. Eng. J., 7 (2020), 19-00519.
[10]Benitez P, et al.: The use of the Hilbert transform in ECG signal analysis, Comput. Biol. Med. 31 (2001), 399–406.
[11]Murakawa H, et al.: Effects of the number of pulse repetitions and noise on the velocity data from the ultrasonic pulsed Doppler method with different algorithms, Flow Meas. Instrum., 40 (2014), 9–18.

18 Eco-morphological and bedload transport assessment on a physical model of a large river widening using ultrasonic Doppler velocity measurements

13th International Symposium on Ultrasonic Doppler Methods for Fluid Mechanics and Fluid Engineering
Zürich, Switzerland (13.-15. June 2021)

Bedload transport assessment on a physical model of a large river widening using ultrasonic Doppler velocity measurements

Saugy Jean-Noël[1], Amini Azin[1] and De Cesare Giovanni[1]

[1] Platform of Hydraulic Constructions, Ecole Polytechnique Fédérale de Lausanne (EPFL), GC A3 504, Station 18, 1015 Lausanne, Switzerland

The 3rd correction of the Rhône River is the largest flood protection project in Switzerland so far. Covering a length of 162 km, it aims to protect some 100,000 people and prevent flood damages, which could raise up to 10 billion Swiss francs for major events. It also intends to revitalize the river and its surrounding area. A natural or revitalized river presents a dynamic morphology that can be assessed using bathymetric survey, bedload transport and hydrodynamic flow behavior. The present case study aims to investigate the behavior of the bedload transport for the future Rhône at the Verney widening using physical model. A valid bedload assessment requires distributed water depths and velocities. The used dataset consists of Lidar scans and recorded streamwise and crosswise velocity profiles. The analysis is performed at two selected cross sections based on the ultrasound Doppler velocity profile method. The velocity profiles allow assessing the local shear stress on the mobile river bed. The different velocity profiles are compared, and the results discussed.

Keywords: Physical modelling, Bedload transport, Ultrasonic Doppler velocimetry, River revitalization

1. Introduction

Local river widening becomes a common approach in river restoration and flood protection. Such projects have become very common in Switzerland in recent years [1]. In the context of the 3rd correction of the Rhône River, several local widenings are planned [2].

Studies have already been carried out for a better understanding of hydraulic, morphological, and ecological phenomena occurring in the local widening [3,4]. The studies conclude that sediment transit must be guaranteed in long term in order to avoid the filling of the widened part and assure the project success.

The bed shear stress must be thus high enough to keep grains in motion. A widely used method for determining local bed shear stress is to fit a logarithmic curve to velocity profile data [5]. Indeed, for subcritical flow, the shear velocity is related logarithmically to the variation of velocity with depth as shown in Eq.1 [6]. Then the shear stress is computed based on the shear velocity (Eq.2). By comparing the computed shear stress for a certain grain size with the critical one according to Shields diagram [7] (Eq.3), its chance of being transported can be assessed.

The Ultrasound Doppler Velocity Profile method (UVP) has been applied in the present project. Since 1995, this method has recurrently been used at the Platform of Hydraulic Construction (PL-LCH) in several hydraulic research projects [8].

$$u = \frac{u_*}{\kappa} * ln\left(\frac{z}{z_0}\right) \quad (1)$$

$$\tau = \rho * u_* \quad (2)$$

$$\tau_{cr} = \theta_{cr} * \rho * g * (s-1) * d \quad (3)$$

where z is height above the bed, z_0 is the characteristic roughness length, u is velocity, $u*$ is shear velocity, s is the ratio between the sand and the water densities, and θ_{cr} is dimensionless critical shear stress.

2. Methodology

2.1 Study area

The 3rd Rhône River correction is divided in various priority levels based on the potential flood risk. The Martigny bend section is set as a priority measure due to potential damages of over 600 million Swiss francs for a 100-year flood event. Upstream of the bend, a local widening (bed widening factor: > 2, length: > 500 m, width: ~180 m) is planned at the Verney section (Figures 1-2).

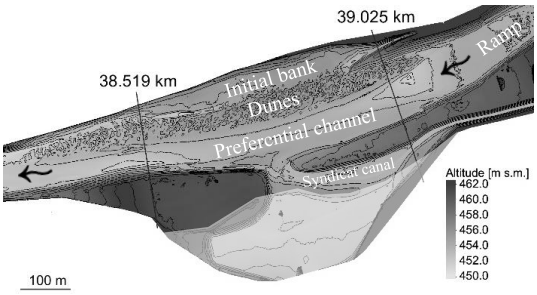

Figure 1: Bathymetry of the Verney widening at the end of the 100-year flood test (Lidar survey) and its configuration.

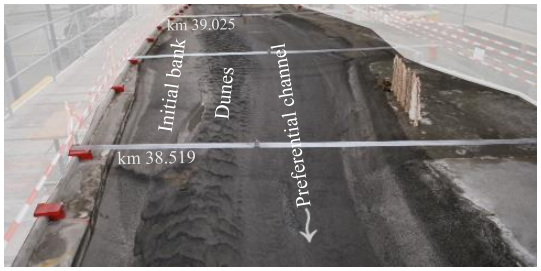

Figure 2: Verney widening at the end of 100-year flood test run (upstream view).

2.2 Models

The PL-LCH team exploited two models: a physical and a 2D numerical one. The latter computes only the depth averaged streamwise velocities. Therefore, the current paper focus only on the physical model results. The model respects the similarities of Froude (conservation of the ratio between inertia and gravity forces) and bed load transport. The scales factors are shown in Table 1 for the geometrical scale λ.

Table 1: Scale factors of the physical model

Parameter	Scale factor
Length	$\lambda = 52$
Velocity	$\lambda^{1/2} = 7.21$
Discharge	$\lambda^{5/2} = 19'499$

As a preliminary step, morphodynamic tests (bed erosion and sediment transport) have been performed to obtain the initial bathymetry (Figures 1-2). A steady-state flood scenario with a return period of 100 years (Table 2) has been run in order to measure velocity profiles.

Table 2: Scenario characteristics

Return period [yr]	Q [m^3/s]	Qsed [m^3/s]
100	1'174	156

The granulometry data are scaled down using the Shields diagram (Table 3). The critical shear stress has been computed for d_m and d_{90}.

Table 3: Grain size and critical shear stress

	Prototype scale [mm]	Model scale [mm]	Critical shear stress (prototype scale) [Pa]
d_m	42.7	0.8	32.2
d_{90}	85.5	1.6	72.5

2.3 Instrumentation

Two UVP (Ultrasonic Velocity Profiler) transducers of 2 MHz were fixed on a manual mobile support moving along pre-existing rails (Figures 2-3). The 1st transducer was oriented in the main flow direction while the 2nd one was set perpendicular to it. Measurements were done along the profiles km 39.025 and 38.519 (Figure 1).

Table 4: UVP transducer configuration

Parameter	Value	Unit
Start point	4.07	mm
Channel distance	2.96	mm
End point	149.11	mm
Maximum depth	456.58	mm
Maximum velocity	+/- 297.5	mm/s
Velocity resolution	2.342	mm/s
Frequency	2188	Hz

In general, the distance between two velocity profile measurements was set to 10 cm. Each measurement station consisted in 100 profiles per transducer and was manually activated. Table 4 shows the used parameters.

A P20 ScanStation from Leica Company was used for Lidar surveys before and after each test in order to interpolate velocities along the whole profile. The P20 theoretical precision is announced to be less than 1 mm. However, only a 3 mm precision (15.6 cm in prototype scale) could be reached. Moreover, thanks to the laser wavelength (808 nm), it is possible to scan the bathymetry while the model is still filled with clear water. However, because of too high turbidity in the water, the Lidar surveys were done without water. In consequence, it is assumed that the bathymetry at the time of the UVP measurements corresponds to the one during Lidar scanning.

The Water Surface Elevation (WSE) was measured using ultrasonic probes at different points. Its value has then been extrapolated for the entire cross section (theoretically flat-water surface).

Table 5 shows the different instruments used and their precision while Figure 3 presents the experimental set-up.

Table 5: Details and precision in situ of the instruments

Instruments	Company	Precision
Doppler effect Ultrasonic Velocity Profiler (UVP)	Met-flow SA	1 mm/s
ScanStation P20	Leica Geosystems	3 mm
Ultrasonic probes		1 mm

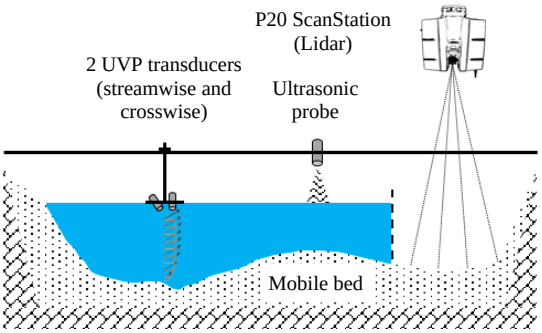

Figure 3: Experimental set-up

2.5 Data processing

For UVP measurements, the whole processing has been done with a MATLAB script fully developed by PL-LCH team [9]. After detecting the river bed using the echo signal, only the measuring channels recorded above the ground were kept. Moreover, the first measuring channels were removed because of their proximity to the transducer. Velocities from the top measuring channel were extended to WSE (given by US probe) in order to estimate the discharge passing through the section, and thus, verify the

UVP measurements. At the same time, velocities were scaled and adjusted regarding the ultrasonic wave incidence angle to normal ($\theta \approx 15.5° \pm 3°$). The two transducers had the same incidence angle.

Lidar data have been georeferenced and meshed (reducing points). Then the elevation of the riverbed measuring channel detected with the echo signal is matched with the bathymetry at the end of the test.

Velocity magnitude and standard deviations are then interpolated (linear interpolation method) and extrapolated (nearest neighbor extrapolation) on a grid of 10 cm x 12 cm. The grid delimitations are WSE and the river bed. For standard deviation, the results were not extended to WSE.

The shear stresses are only computed based on the UVP velocity profiles and for the velocity magnitude. As mentioned before and shown in Figure 4, a linear regression is done in a semi-logarithmic graph. The coefficient of determination (R^2) is computed for validating the log profile. Its value must be over 0.9 otherwise the shear stress is not calculated.

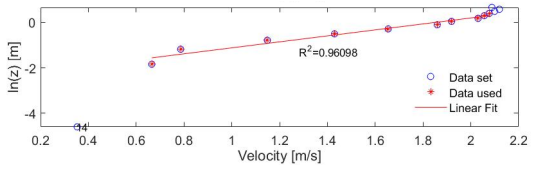

Figure 4: Example of a linear fitting on the velocity magnitude profile on a semi-log graph (profile km 38.519)

4. Results

The velocity magnitudes on both extracted sections show similar structures, despite their different locations (Figures 5-6). High velocities can be observed in a specific area. Velocities are higher at the Verney end (< 4 m/s against < 3.5 m/s) but the area is narrower (~40 m against ~60 m). This area where bed load is in majority transported is labelled as preferential channel or "Super Channel" On its right, the velocities are progressively lowering.

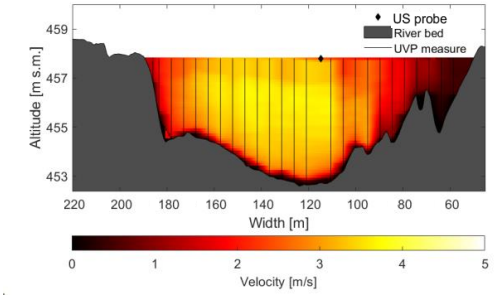

Figure 5: Velocity magnitude for the section km 39.025

The crosswise velocity component is negligible for both sections. Figure 7 illustrates the variation rate for section km 38.519. The variation rate between the magnitude and the flow direction component is less than 5 %. This confirms the initial assumption of a non-complex flow occurring in the widened area. However, some UVP measures show a variation rate higher than 10 %. These points are located where the streamwise velocities are low, i.e. on top of the dunes where bed form roughness is highest. As such, the river flow deviates from logarithmic velocity profiles [10].

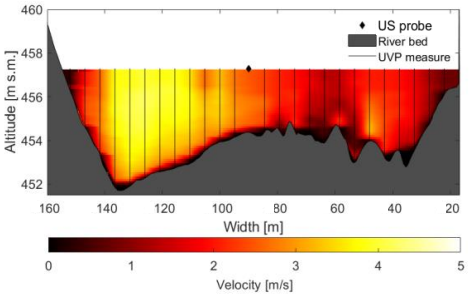

Figure 6: Velocity magnitude for the section km 38.519

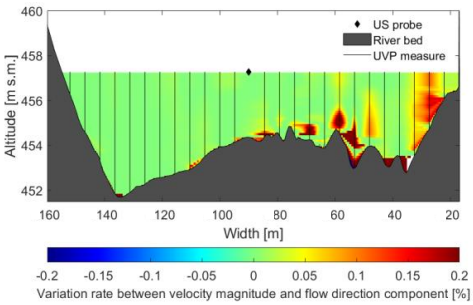

Figure 7: Variation rate between velocity magnitude and flow direction component

Standard deviation results show a similar pattern as the crosswise velocities (Figure 8). The values are low (< 0.4 m/s) for the preferential channel but are high above the dunes (> 0.6 m/s). The flow is more disturbed because of theses macro shapes. The disturbance is even more significant for the standard deviation of the crosswise velocities (Figure 9).

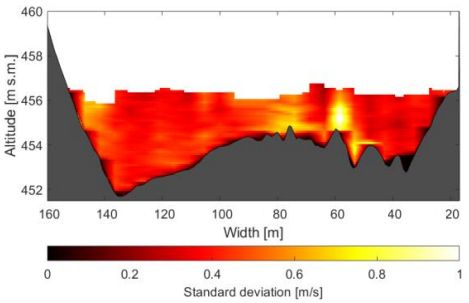

Figure 8: Standard deviation of the flow direction velocities for the profile km 38.519

Standard deviations at section km 38.519 are lower than the ones at the section km 39.025. The velocities are less dispersed at the downstream section part of Verney than

upstream. This is due to the proximity of the ramp and the flow adaptation to the widened bed (Figure 1).

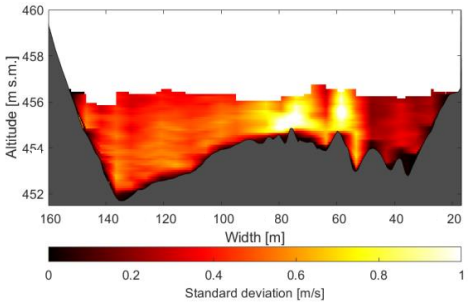

Figure 9: Standard deviation of the crosswise velocities for the profile km 38.519

Regarding the shear stress distribution (Figures 10-11), the results show the same trend. Indeed, shear stresses higher than the critical shear stress for d_m and even d_{90} have been computed in the "Super Channel". It is not the case for the riverbanks except locally for the dunes located at a distance of 40 m to 90 m on the section km 38.519. These points perfectly match the ones with high crosswise velocities and standard deviation. For reminder, the shear stress is only computed for velocity profiles with R^2 higher than 0.9.

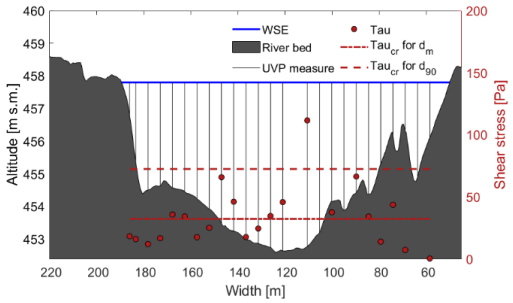

Figure 10: Shear stresses computed for the profile km 39.025

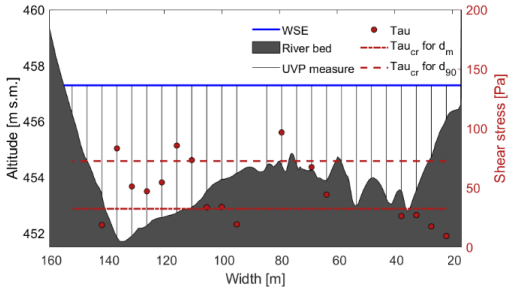

Figure 11: Shear stresses for the profile km 38.519

5. Conlusions

In conclusion, this paper brings up the existence of a preferential channel or "Super Channel" where velocities are high and shear stresses are greater than the critical values for d_{90}. This guarantees bed load transit along the Verney Widening and prevents its filling with sediment over time.

Moreover, there is a clear distinction between the flow structure in this preferential channel and the banks. Flow over initiated sediment deposits and dunes show different velocity profiles. In classical steady state uniform open channel flow, a logarithmic velocity profile establishes naturally [11], whereas outside the main channel flow velocity distributions tend to be less structured. The cross flow component is more significant. Therefore, computed shear stress based on the log profile is less accurate. Nevertheless, grain motion could be identified along the dunes even for large grain sizes.

References

[1] Eidgenössische Forschungsanstalt für Wald, Schnee und Landschaft (WSL): Local river widening (wsl.ch) -selected examples from Switzerland (04.04.2008).

[2] Canton du Valais: Plan d'aménagement (PA-R3) – Rapport de synthèse, published in 2014, updated 2015.

[3] Schirmer, M., Luster, J., Linde, N., Perona, P., Mitchell, E. A. D., Barry, D. A., Hollender, J., Cirpka, O. A., Schneider, P., Vogt, T., Radny, D., and Durisch-Kaiser, E.: Morphological, hydrological, biogeochemical and ecological changes and challenges in river restoration – the Thur River case study, Hydrol. Earth Syst. Sci., 18, 2449–2462 (2014).

[4] Martín, E.J., Ryo, M., Doering, M., Robinson, C.T.: Evaluation of restoration and flow interactions on river structure and function: Channel widening of the Thur River, Switzerland (2018)

[5] Biron, P., Robson, C., Lapointe, M., & Gaskin, S.: Comparing different methods of bed shear stress estimates in simple and complex flow fields. Earth Surface Processes Landforms, 29(11), 1403–1415 (2004).

[6] Schlichting H.: Boundary Layer Theory, 7th edition, McGraw-Hill, New York (1987).

[7] Shields, A.: Anwendung der Aehnlichkeitsmechanik und der Turbulenzforschung auf die Geschiebebewegung. Mitteilung der Preussischen Versuchsanstalt fur Wasserbau und Schiffbau, Heft 26, Berlin. Belin (1936).

[8] Nilipour N., De Cesare G. & Boillat J.-L.: Application of UVP transducers to measure bed geometry and velocity profiles in a hydraulic scale model with gravel pit, 4th International Symposium on Ultrasonic Doppler Method for Fluid Mechanics and Fluid Engineering (2004)

[9] Saugy J.-N.: Post-processing data from UVP, Lidar survey and US probe for computing velocity profiles and shear stress, version 7.1 (created in Jan. 2020, updated in Feb. 2021)

[10] Best, J.: The fluid dynamics of river dunes: A review and some future research directions, J. Geophys. Res., 110, F04S02 (2005).

[11] Meile, T., De Cesare G., Blanckaert K. & Schleiss A. J.: Improvement of Acoustic Doppler Velocimetry in steady and unsteady turbulent open-channel flows by means of seeding with hydrogen bubbles, Flow Measurement and Instrumentation, Volume 19, Issues 3–4, pp. 215–221, https://doi.org/10.1016/j.flowmeasinst.2007.08.009 (2008)

Acknowledgments

The present study was financially supported by the Canton of Valais, Service de la protection contre les crues du Rhône. Our gratitude also goes to Met-Flow in Lausanne for their support on the use of the UVP instrument.

19 Ultrasonic Doppler flow velocity measurements as a co-indicator for the eco-morphological assessment in a residual flow reach

13th International Symposium on Ultrasonic Doppler Methods for Fluid Mechanics and Fluid Engineering
Zürich, Switzerland (13.-15. June 2021)

Ultrasonic Doppler flow velocity measurements as a co-indicator for the eco-morphological assessment in a residual flow reach

Robin Schroff[1], Christian Mörtl[1], Giovanni De Cesare[1]

[1] Platform of Hydraulic Constructions (PL-LCH), Ecole Polytechnique Fédérale de Lausanne (EPFL), Station 18, 1015 Lausanne, Switzerland

It is a complex task to evaluate the effects of a river rehabilitation measure on the riverscape's habitat mosaic. This study investigated the medium term effects of a rehabilitation measure in a residual flow reach downstream of a hydroelectric dam. The rehabilitation measure consisted of an artificial flood coupled with a sediment augmentation measure. The evaluation was based on the indicator set of habitat diversity, published by the Swiss Federal Office for the Environment (FOEN) for the outcome evaluation of restoration projects. It is composed of six eco-morphological indicators, among which 1.3 and 1.4 assess the variability of water depth and flow velocity, respectively. In each study reach, the measurements were taken along hydro-morphologically representative cross sections for at least eleven points per cross section. A handheld Acoustic Doppler Velocimeter (ADV) was used to measure flow velocity. Digital, GNSS-supported surveying with a mobile GIS application significantly enhanced the assessment workflow. The study results suggest that neither the single artificial flood nor its coupling with the 2016 sediment augmentation were sufficient to restore a functional habitat mosaic in the medium or long term.

Keywords: Eco-morphological assessment, River rehabilitation, Residual flow reach, Sediment augmentation, Ultrasonic Doppler velocimetry

1. Introduction

Medium and high-head hydropower storage plants produce electricity by conveying water from the reservoir via the pressurized waterway to the powerhouse. The river segment bypassed by the waterway is referred to as residual flow reach. Residual flow reaches are often characterized by a minimum residual flow discharge and little to no upstream bedload supply, due to the trapping of sediments inside the reservoir [1]. These hydro-morphological disturbances reduce morphodynamics in the residual flow reach to a minimum, resulting in eco-morphological degradation [2]. In a natural riverscape, the patchy distribution of eco-morphological characteristics, such as water depth and flow velocity, forms a dynamic mosaic of habitats [3]. To improve the quality of a residual flow reach's habitat mosaic, artificial floods [4], and their coupling with artificial sediment augmentation [5, 6], can be an effective rehabilitation measure.

In the residual flow reach of the Sarine river in Switzerland, downstream of the Rossens dam (Figure 1), an artificial flood was combined with an artificial sediment augmentation in 2016. The bed material (1000 m^3) was excavated from the adjacent alluvial forest and arranged in four alternated deposits along both banks, 9 km downstream of the dam. During the flood, the constant residual discharge (summer 3.5 m^3/s, winter 2.5 m^3/s) was increased to a peak flow of approximately 190 m^3/s. Immediate follow-up studies found the eco-morphological effects to be positive [5], but questioned their persistence in the absence of repetitive rehabilitation measures [6].

This study evaluates the measure's medium-term effects by using and extending the indicator set 1 "habitat diversity" of the guideline for the outcome evaluation of river restoration projects (Monitoring and Evaluation, M&E) [7]. It was published by Switzerland's Federal Office for the Environment (FOEN) in 2019 and includes the assessment of the coefficient of variation (CV) of flow velocity and water depth measurements. Both are important indicators for the eco-morphological assessment of a river reach [7]. In this study, flow velocity was measured with Ultrasonic Doppler velocimetry using a handheld Acoustic Doppler Velocimeter (ADV).

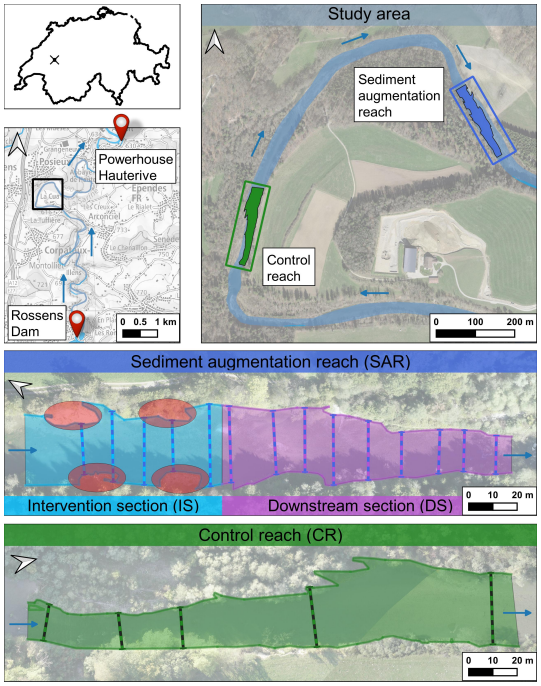

Figure 1: Study reach definition. Positions of the sediment deposits (red ellipses) and of flow velocity measurement cross sections (dashed lines). Maps and study area background © swisstopo; Sediment augmentation reach and control reach background © Research Group for Ecohydrology, ZHAW

2. Materials and Methods

2.1 Study area

The Sarine river is a heavily regulated stream that has its source at Sanetsch (2252 m a.s.l.). In the study area, the Sarine is described as a flat, large watercourse of the colline, carbonatic midlands [8]. At Rossens, it is dammed by a 83 m high arch dam, forming the Lac de la Gruyère, one of Switzerland's five biggest reservoirs (V= 200 million m^3, A=10 km^2). The 13 km long residual flow reach up to the powerhouse Hauterive has an average slope of 0.3 % and is characterized by a channel-riffle-rapids sequence.

The 200 m long study reach around the four sediment augmentation deposits (sediment augmentation reach, SAR) and a suitable upstream control reach (CR) of the same length were defined in accordance with the M&E guideline [9]. As illustrated in Figure 1, the sediment augmentation reach is subdivided into the 80 m long intervention section (IS) and the subsequent, 120 m long downstream section (DS).

2.2 M&E indicator set 1 "habitat diversity"

The indicator set 1 "habitat diversity" consists of six indicators. Each indicator is named after an eco-morphological characteristic and can score a standardized value between 0 (degraded or artificial) and 1 (near-natural). To compensate for the still missing calculation procedure for indicator 1.6 A1 "Substrate composition", the indicator set was extended by the "Indicator of Reproduction suitability based on Substrate degradation" (IRS) [10]. Table 1 provides an overview of the indicators that were applied and their calculation criteria.

Table 1: M&E indicator set 1 "habitat diversity", extended by the "Indicator of Reproduction suitability based on Substrate degradation" (IRS)

Indicator		Indicator calculation with
1.1	River bed structures	Number of bed structures
1.2	River bank structures	Number of structures and non-obstructed length
1.3	Water depth	Coefficient of variation
1.4	Flow velocity	Coefficient of variation
1.5	Presence of cover	Area of cover relative to a reference state
1.6 A1	Substrate composition	*Currently not available*
1.6 A2	Substrate mobilisability	Relative presence of bed load and other mobilisability types
IRS / 1.6 A3	Reproduction suitability based on Substrate degradation	Fraction of suitable, non-consolidated and non-embedded substrate

The calculation of the hydraulic indicators 1.3 and 1.4 is based on measurements along of up to 15 cross sections per study reach. All other indicators require the reach-wide mapping of homogeneous sections and patches. The calculation of indicators 1.1 and 1.2 is based on the number of homogeneous bed and bank structures. The calculation of indicator 1.5 is based on the comparison of the current presence of cover with a natural reference state. For the present study, two independent estimates (P. Vonlanthen, Aquabios Sàrl; C. Weber, Eawag) were averaged. The IRS (indicator 1.6 A3) assesses substrate quality based on brown trout's substrate requirements for reproduction. It makes direct use of and extends the existing mapping procedure for the M&E indicators 1.6 A1 and 1.6 A2.

In the sediment augmentation reach, 14 cross sections (263 points) were sampled. Due to limited capacity, only five cross sections (77 points) were sampled in the control reach. These cross sections were distributed, at the discretion of the authors, to best represent the reach's hydro-morphological characteristics.

From all measurements of a reach, the coefficients of variation (CV) are calculated according to Eq. 1 and Eq. 2 from the sample standard deviation (σ) and the sample mean (μ) for water depth and flow velocity.

$$CV_{max.\ water\ depth} = \frac{\sigma_{max.\ water\ d.}}{\mu_{max.\ water\ d.}} \times 100\ \% \qquad (1)$$

$$CV_{flow\ velocity} = \frac{\sigma_{flow\ velocity}}{\mu_{flow\ velocity}} \times 100\ \% \qquad (2)$$

In the sediment augmentation reach, CV values were additionally calculated separately for the intervention section (5 cross sections, 99 samples) and the downstream section (9 cross sections, 164 samples). To obtain indicator values between 0 and 1, the CV values are linearly standardized as described by the M&E guideline [7].

2.3 Ultrasonic Doppler velocimetry

Flow velocity was measured using the handheld ADV FlowTracker by SonTek. The FlowTracker's acoustic transmitter is located in between two laterally protruding receivers (Figure 2), allowing to perform pointwise 2D velocity measurements.

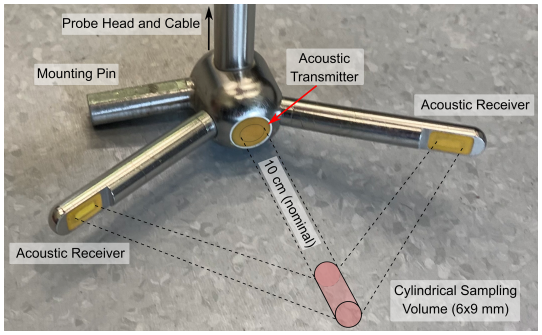

Figure 2: SonTek FlowTracker Probe and Sampling Volume, description according to the FlowTracker Technical Manual

Handheld ADVs offer several advantages. They quickly deliver results of high accuracy, do not require on-site calibration, and do not depend on mechanical parts. Table 2 presents the details of the applied methodology.

Table 2: ADV equipment and sampling methodology

Handheld ADV	FlowTracker by SonTek
Ping rate	10 Hz
Sampling rate	1 Hz
Averaging time	10 s
Measurement error	Typically < 0.01 m/s
Sampling volume distance	10 cm from the probe
Measurement depth	60 % water depth from surface
Distance between samples	1.4 m

2.4 Further equipment and field work

For the field work, a digital mapping environment was set up. It consisted of a field tablet (Trimble T10), a survey-grade GNSS antenna (Trimble R2) and a comprehensive project for the mobile GIS application QField [11]. This set-up allowed for GNSS and orthophoto based mapping and provided decision support for the placement of cross sections. The field equipment is shown in Figure 3. Field work took place in summer 2020 and lasted two weeks. Sunny conditions and moderate turbidity provided for good visibility of the streambed substrate.

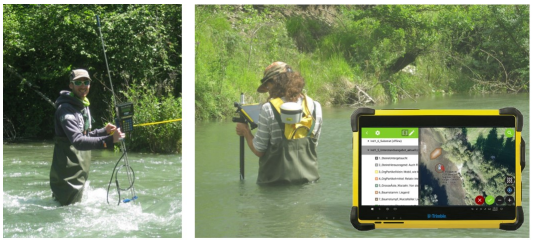

Figure 3: Field equipment used for surveying: The handheld Acoustic Doppler Velocimeter FlowTracker by SonTek (left), field tablet Trimble T10 and GNSS antenna Trimble R2 (right)

3. Results

The evaluation of the surveying results was based on the procedure described in the M&E guideline [7]. In the control reach, seven bed structures were identified. The sediment augmentation reach counted 24 structures. Most of its bed structures were concentrated in the intervention section (18 structures). There were eight structures in the downstream section, and two structures extended across the section boundary. The ratio of the areas covered by the dominant bed structures channel, riffle, rapids, and shallow water varied significantly among the study reaches and sections. The highest number of bank structures was identified in the control reach, the highest density in the intervention section.

On average, the sediment augmentation reach had shallower water depths and higher flow velocities than the control reach. In the downstream section, shallow water depths smaller than 0.6 m were dominant. In the intervention section as well as in the control reach, water depths greater than 1.4 m were measured. All CV values of water depth measurements stayed within the range from 0 to 1 and directly translate to indicator scores.

Figure 4 shows the histograms of flow velocity measurements. The flow velocity histogram of the intervention section is dominated by relatively slow flow velocities (v_{max} (IS) = 0,54 m/s). In the rapids zones of the downstream section and the control reach, flow velocities up to v_{max} (DS) = 1.33 m/s and v_{max} (CR) = 1.48 m/s were measured. The smaller number of cross sections and measurement points in the intervention section is the reason for the smaller size of its attributed area in the stacked histogram, compared to the downstream section. The coefficients of variation of water depth and flow velocity in the intervention section and downstream section were significantly lower than the CV values for the entire sediment augmentation reach (Table 3).

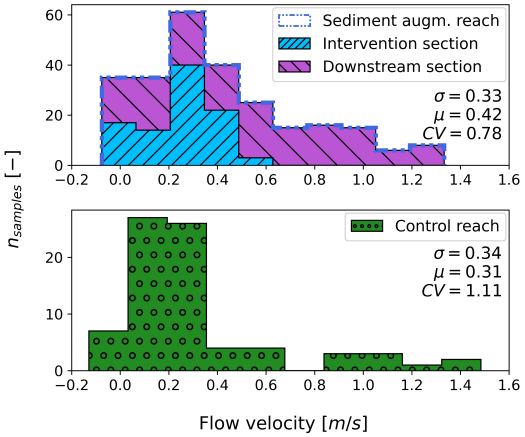

Figure 4: Histograms of flow velocity samples in the sediment augmentation reach (top) and the control reach (bottom). The intervention section and downstream section samples are stacked to form the sediment augmentation reach histogram

The streambed of both study reaches was predominantly stabilized by a coarse-grained top layer (armor layer). Only 3.9 % of streambed area was dominated by bedload. In the sediment augmentation reach, 6 % of the area was dominated by substrate considered as potentially suitable for reproduction in brown trout (gravel and stones) versus 12 % in the control reach. In both study reaches, around 70 % of potentially suitable area for trout reproduction was qualified as non-suitable due to degradation.

Table 3 provides an overview of the final indicator results. Neither the sediment augmentation reach nor the control reach has a global tendency to score higher than the other. All four study reaches and sections obtain higher scores for indicators 1.1 to 1.4 than for indicators 1.5, 1.6 A2 and the IRS. The sediment augmentation reach scores higher than the control reach for two indicators (river bed structures, water depth), obtains equal scores for two other indicators (presence of cover, substrate mobilisability) and a lower score for three indicators (river bank structures, flow velocity, reproduction suitability). Compared to the entire sediment augmentation reach, the intervention section and the downstream section obtain lower scores for both hydraulic indicators (water depth, flow velocity).

Table 3: Indicator results and metrics of water depth and flow velocity for the control reach (CR), the sediment augmentation reach (SAR), the intervention section (IS) and the downstream section (DS). Values are linearly color coded from 1 (green) via 0.5 (yellow) to 0 (red)

Indicator results / Metrics		CR	SAR	IS	DS
1.1	River bed structures	0.75	1.00	1.00	1.00
1.2	River bank structures	0.92	0.90	1.00	0.86
1.3	Water depth	0.53	0.66	0.49	0.54
	σ [m]	0.32	0.23	0.26	0.13
	μ [m]	0.60	0.35	0.53	0.25
	CV	0.53	0.66	0.49	0.54
1.4	Flow velocity	1.00	0.71	0.56	0.63
	σ [m/s]	0.34	0.33	0.15	0.36
	μ [m/s]	0.31	0.42	0.24	0.52
	CV	1.11	0.78	0.61	0.69
1.5	Presence of cover	0.25	0.25	0.25	0.25
1.6 A2	Substrate mobilisability	0.25	0.25	0.25	0.25
IRS / 1.6 A3	Reproduction suitability (Substrate degradation)	0.32	0.27	0.36	0.25

4. Discussion

A control reach based outcome evaluation has the imminent disadvantage that not all key characteristics of the control reach and the rehabilitated reach fully coincide. In particular, the studied reaches and sections turned out to have considerably varying ratios between areas of riffle, channel, rapids, and shallow water, each representing particular hydraulic characteristics. The intervention and downstream sections of the sediment augmentation reach achieved significantly lower CV values for water depth and flow velocity compared to the entire reach. This fact suggests that special care is required for the interpretation of the two indicators in a control reach based outcome evaluation.

The required time to measure a water depth and flow velocity profile of 25 m width at a spacing of 1.4 m was approximately 30 minutes. The digital recording of measurements within the QField application proved to be highly efficient. The signal to noise ratio (SNR), representing the strength of the acoustic reflection from particles in the water, was at any time ideal (> 10 dB) in the natural environment. In turbulent sections, the number of spikes was sometimes higher than the recommended threshold of 10 %. In the context of this study case, the accuracy of the ADV measurements was largely sufficient.

5. Conclusions

Four years after the artificial flood, the Sarine sediment augmentation continued to affect certain components of the residual flow reach's habitat mosaic. The most noticeable difference between the sediment augmentation reach and the control reach is the increased structural diversity in proximity to the partially eroded sediment deposits. Yet, the study's results suggest that the isolated artificial flood with sediment augmentation was not an effective single measure against streambed degradation in the medium term.

To increase bedload and habitat dynamics in a residual flow reach in the long term, the combination of annual flood events, dynamic e-flows, and continuous bedload feeding could be an effective measure. The digital, GNSS-supported surveying with QField was estimated to provide overall time savings of up to 50 % and improve data accuracy. The handheld Acoustic Doppler Velocimeter greatly enhanced data collection for the eco-morphological assessment of the river rehabilitation measure.

Acknowledgements

This study was financially supported by the FOEN as part of the "Hydraulic Engineering & Ecology" project. Special thanks are due to Dr. Christine Weber (Eawag) for her expert advice.

References

[1] Schleiss AJ, *et al.*: Reservoir sedimentation, Journal of Hydraulic Research, 54 (2016), 595–614.
[2] Peter A: A Plea for the Restoration of Alpine Rivers: Basic Principles Derived from the "Rhone-Thur" Case Study, Alpine Waters, Springer Berlin Heidelberg (2010), 247–260.
[3] Stanford J, *et al.*: A general protocol for restoration of regulated rivers, Regul Rivers: Res Mgmt, 12 (1996), 391–413.
[4] Mürle U, *et al.*: Effects of experimental flooding on riverine morphology, structure and riparian vegetation: The River Spöl, Swiss National Park, Aquatic Sciences - Research Across Boundaries, 65 (2003), 191–198.
[5] Stähly S, *et al.*: Sediment replenishment combined with an artificial flood improves river habitats downstream of a dam, Sci Rep, 9 (2019), 5176.
[6] Döring M, *et al.*: Künstliches Hochwasser an der Saane - Eine Massnahme zum nachhaltigen Auenmanagement, Wasser Energie Luft, 110 (2018), 119–127.
[7] Weber C, *et al.*: Wirkungskontrolle STANDARD – Ablauf und Organisation, Wirkungskontrolle Revitalisierung - Gemeinsam lernen für die Zukunft, FOEN, Bern (2019).
[8] Federal Office for the Environment (FOEN): Fliessgewässertypisierung der Schweiz: Porträt Gewässertyp Nr. 16, (2013).
[9] Sprecher L, *et al.*: Zwei Elemente – ein Ziel: wirkungsvolle Revitalisierungen, Ingenieurbiologie / Genie Biologique, 30 (2020), 12–19.
[10] Schroff R, *et al.*: Eco-morphological evaluation of a sediment augmentation measure, WasserWirtschaft, *under review*.
[11] The QField Project/OPENGIS.ch: QField Documentation, https://qfield.org/docs/index.html, (2020).

20 Development of Advanced UVP Instruments Applicable to 3-D Velocity Vector Measurement

13th International Symposium on Ultrasonic Doppler Methods for Fluid Mechanics and Fluid Engineering
Zürich, Switzerland (13.-15. June 2021)

Development of Advanced UVP Instruments Applicable to 3-D Velocity Vector Measurement

Naruki Shoji[1], Hideharu Takahashi[2], and Hiroshige Kikura[2]

[1] Graduate Major in Nuclear Engineering Course, Tokyo Institute of Technology, 2-12-1 Ookayama, Meguro-ku, Tokyo 152-8550, Japan
[2] Lab. for Advanced Nuclear Energy, Tokyo Institute of Technology, 2-12-1 Ookayama, Meguro-ku, Tokyo 152-8550, Japan

A new UVP instruments applicable to 3-D velocity vector measurement was developed. The instruments consist of four channel UVP measurement channel, and four ultrasonic elements array sensor (1 transmitter and 3 receivers). With this configuration, there are three Doppler frequencies can be obtained, hence the three-dimensional velocity information along the measurement line can be reconstructed. In this study, we confirmed the measurement principle experimentally using by the developed UVP instruments. As the experiment, we performed the piping flow measurement, and reconstructed the velocity vector profile with four elements array sensor. As the result, the three-dimensional velocity vector profile was obtained by the measurement system.

Keywords: 3-D velocity vector, Hardware development, Signal processing

1. Introduction

Recently, optical inspections have been implemented for the decommissioning of the Fukushima Dai-ichi nuclear power plant (1F). The objective of these inspections is to assess the conditions within the primary containment vessels (PCVs) of units 1,2 and 3 at the site, and some achievements has been made so far [1]. However, these inspections have not yet unveiled completely the locations of leaks (the repair of which is vital for fuel debris removal) and accurate distribution of fuel debris (an important factor in deciding the future fuel removal procedure). These inspections are hindered by a high-dose radioactive environment and an opaque environment which becomes from the suspended particulates in the coolant water. Therefore, methods other than optical methods are required to inspect within the PCVs.

Ultrasonic measurement is considered as a promising non-optical inspection method. Ultrasonic sound can be used in opaque liquids and ultrasonic transducers are generally suited to high radiation levels, as used in the decommissioning of Three Mile Island (TMI-2) [2]. In our work, an ultrasonic velocity profiler (UVP) [3] and an ultrasonic phased array sensor were used in combination to identify leakage points [4]. The combination system of UVP and phased array sensor allows for the measurement of two-dimensional (2-D) flow velocity vector fields using the Doppler frequency shift of echoes scattered by particles in the liquid. Hence, leakage points may be identified by observing behavior of liquid flow near pipes or walls.

However, real flow is three-dimensional (3-D) flow, and measurement system is also required to extend to 3-D flow measurement. Peronneau *et al*. [5] proposed a single element cross beam system using two transducers as a transceiver (transmitter/receiver) to measure 2-D at the cross point. Further development of a similar measurement system for measuring 3-D by using three transducers was shown in the work of Fox [6]. However, this system is time-consuming since the transducers must be operated separately to avoid the interference of the sound beam. Later, Dunmire *et al*. [7] developed a 3-D measurement system using 5 transducers (1 transmitter and 4 receivers). With only 1 transmitter, the measurement occurs at the same time and same measurement volume. In fluid engineering, the area of investigation is wider, therefore depth varying (profile) measurement is necessary. Like Dunmire *et al*. measurement system, Huther and Lemmin [8] developed three-dimensional with varying depth measurement system in open-channel flow. Based on this idea, Obayashi *et al*. [9] investigated this system accuracy in rotating cylinder flow. They found that the velocity in receiver line has a relatively high error with the reason of low signal to noise ratio.

These studies are very important to be continuously improved since the flow in fluid engineering often exists with multi-dimensional velocity such as 1F case. Previously, we designed five elements transducer (1 transmitter and 4 receivers) and constructed 3-D velocity vector measurement system [10]. This system achieved 3-D velocity vector profile measurement with a compact sensor. However, this system reconstructed 3-D velocity vector by synthesizing dual 2-D velocity vector, and it used large hardware system due to multi element using. In principle, 3-D velocity vector can be reconstructed at least 1 transmitter and 3 receivers, and it can be more compact system. Furthermore, measurement hardware also can be optimized to the multi elements UVP system.

The purpose of this study is development of the 3-D flow vector measurement system with four elements sensor array and optimized hardware system for multi elements UVP measurement. In this paper, the vector UVP system is described and the velocity profile measurement using this system is demonstrated with piping flow.

2. Three-Dimensional Velocity Vector Measurement

2.1 Principle

In this study, we considered three-dimensional (3-D) velocity vector profile measurements with four ultrasonic elements and UVP principle to simplify the sensor configuration. The principle of 3-D velocity vector profile measurement is illustrated in figure 1, and the sensor configuration is illustrated in figure 2. The sensor unit consists of one transmitter and three receivers. The receivers are installed at 120-degree intervals with each receiver, and the transmitter is in its center. Each receiver gets the echo signals included Doppler frequency, and can calculate a velocity component along with receiving line. Each velocity component can be obtained as the following equation.

$$\begin{pmatrix} v_1 \\ v_2 \\ v_3 \end{pmatrix} = \begin{pmatrix} v_z \cos\alpha + v_x \sin\alpha \\ v_z \cos\alpha - \dfrac{(v_x - v_y)\sin\alpha}{2} \\ v_z \cos\alpha - \dfrac{(v_x + v_y)\sin\alpha}{2} \end{pmatrix} \quad (1)$$

where v_x, v_y and v_z represent each velocity component in the Cartesian coordinate system, and α is the angle between measurement line and receiving line. The receiving angle α is decided by measurement depth z, and it can be calculated by the following equation.

$$\alpha = \tan^{-1}\left(\frac{G}{z}\right) \quad (2)$$

where G is the distance between transmitter element and receiver element as shown in figure 2. By using Eq. (1) and (2), the 3-D velocity vector $\vec{V}$ can be reconstructed by following equation.

$$\vec{V} = \begin{pmatrix} v_x \\ v_y \\ v_z \end{pmatrix} = \begin{pmatrix} \dfrac{2v_1 - (v_2 + v_3)}{3\sin\alpha} \\ \dfrac{v_2 - v_3}{\sin\alpha} \\ \dfrac{v_1 + v_2 + v_3}{3\cos\alpha} \end{pmatrix} \quad (3)$$

Therefore, the 3-D velocity vector profile on the measurement line can ben obtained by calculating the velocity vector using the Eq. (3) at each position.

2.2 Measurement system

To measure a 3-D velocity vector profile with four ultrasonic elements, the UVP measurement hardware which can control four elements was designed and implemented as shown in figure 3. The hardware circuit consists of high voltage pulsers (up to 200 $V_{p\text{-}p}$), programmable gain amplifiers (up to 55 dB) and band-pass filters as echo signal receiver, an eight-channel A/D converter (sampling rate is 50 MS/s, and bit resolution is 12 bit), and other power supply components. The developed hardware performed by 12 V DC power supply. And these circuits are controlled by a FPGA (field programmable gate array) board. The received echo signals are recorded on the DDR3 memory implemented on the FPGA board, and the recorded all echo data is transferred to the host computer through an USB 3.0 cable in real-time. After that, the signal processing is carried out based on Eq. (3) in the host computer. Moreover, the developed hardware size is about 150 mm × 150 mm to mount to a robot system in the future. The developed UVP hardware can control 8 ultrasonic elements simultaneously, but in this time, we used only 4 channels for the measurement. Figure 4 shows the measurement setup. In this study, LabVIEW 2019 (NI) was used for the hardware control and the signal processing of four elements velocity vector UVP measurement.

In this study, the specification of constructed four elements array sensor is below: the basic frequency of each element is 4 MHz, and the element diameter is 5 mm. Also, the distance between transmitter element and each receiver element is set to 10 mm.

And to detect a Doppler frequency, the auto-correlation method [11] was used in this system. The process using this method is performed to obtained echo signals of each receiver. After that, the velocity reconstruction process is applied to detected velocity components using Eq. (3).

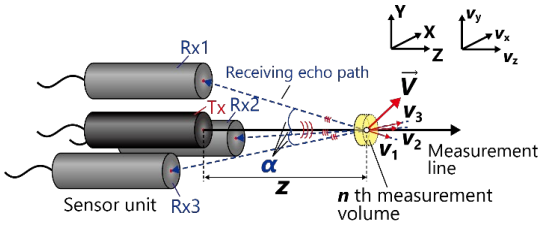

Figure 1: Principle of 3-D velocity vector measurement with four ultrasonic elements.

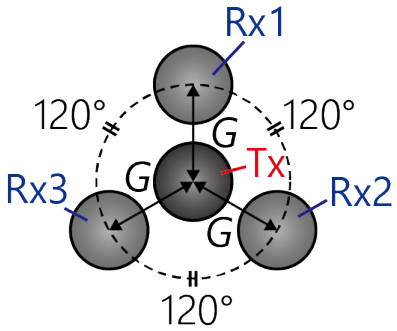

Figure 2: Sensor layout of four elements array.

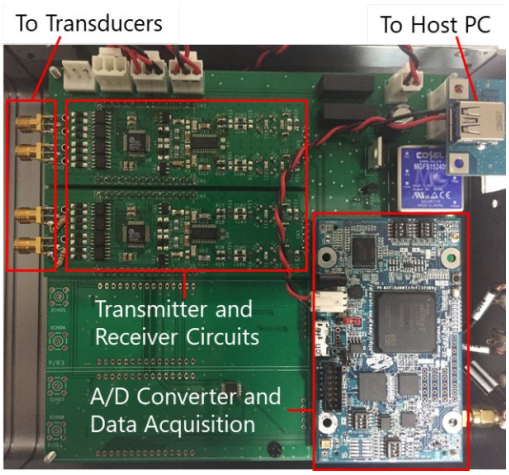

Figure 3: Developed UVP measurement hardware device.

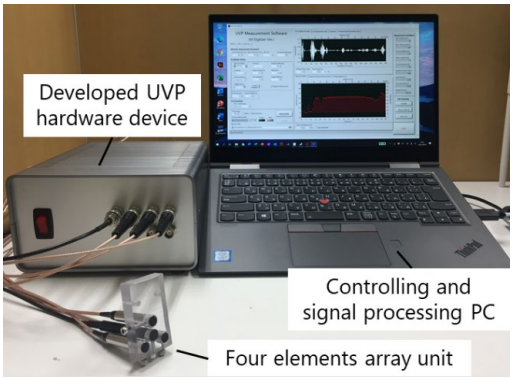

Figure 4: Measurement system.

3. Experiment

The experimental setup is illustrated in figure 5. To demonstrate the 3-D velocity vector profile measurement, the experiment was performed with vertical water piping flow, and we confirmed the measurement principle with four elements array. The pipe diameter was 50 mm, and the pipe material was plexiglass. The test section was located at approximately 800 mm from the flow entrance. The nylon particles (mean diameter: 80 μm) were mixed in water as tracer particle. The flowrate was set to approximately 0.13 m^3/s in this experiment. The array unit was installed at an angle of 0 degrees to the wall to transparent within the pipe. Other measurement conditions are summarized in table 1.

4. Results and Discussion

Figure 6 shows the experimental results of piping flow measurement with developed UVP system. Figure 6 (a) is YZ plane view, (b) is XZ plane view, respectively. In these figures, black line represents the pipe wall. And the center of the transmitter is at the origin (x, y, z) = (0, 0, 0). The piping flow is almost one-dimensional flow; therefore, the measured velocity vectors should be direct to y direction.

In figure 6 (a), there was the influence of multiple echoes around z = 18 mm region. It is considered that the incident angle was 0 degree and the echo from the wall came directly. And the velocity magnitudes were underestimated in near region less than 10 mm, because this region is out-range of receivable angle of receiver elements, and the signal-to-noise ratio was decreased. Thus, it needs to design the sensor layout and size to focus on the near region. However, the measured velocity vector profile was captured the one-dimensional flow patter in the pipe. Therefore, we confirmed measurement principle of 3-D velocity vector profile measurement with four elements array.

Table 1: Measurement conditions.

Ultrasonic frequency	4	MHz
Pulse repetition frequency	2	kHz
Number of cycles	4	-
Number of repetitions	128	-
Spatial resolution	0.74	mm
Temporal resolution	64	ms
Supply voltage	140	$V_{p\text{-}p}$
Incident angle	0	degrees
Number of profiles	2,000	-

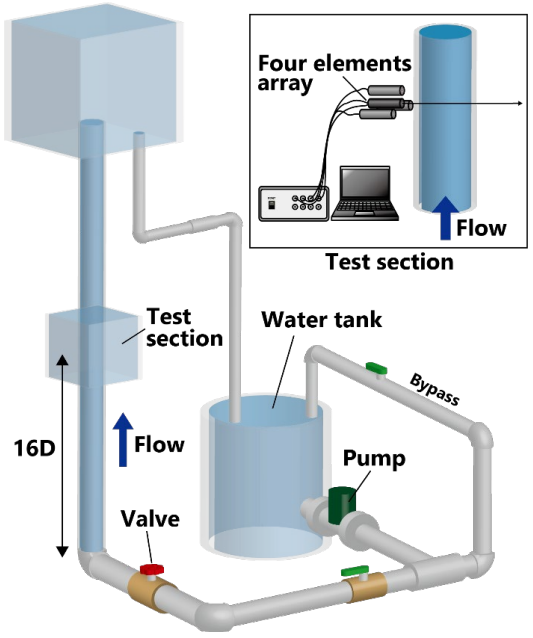

Figure 5: Experimental setup.

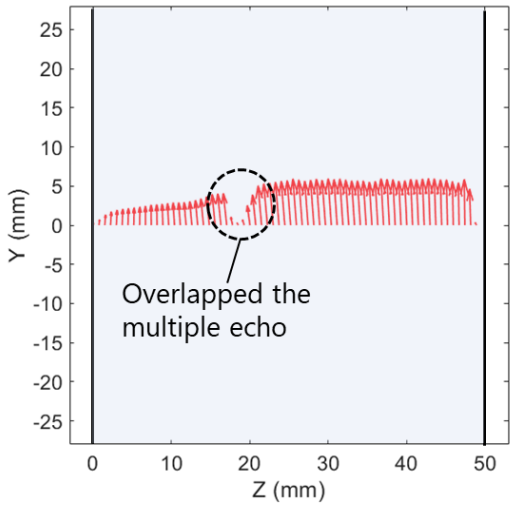

(a) YZ plane view

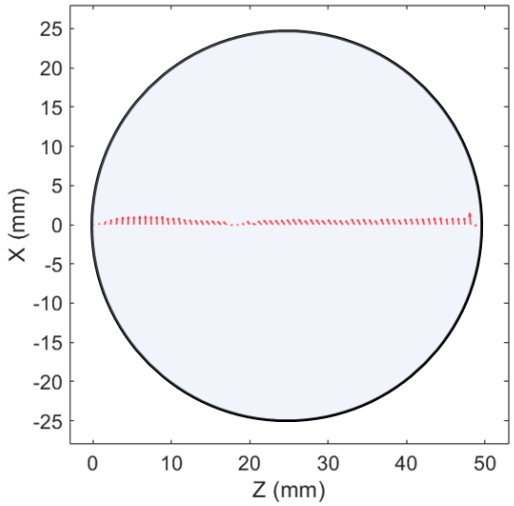

(b) XZ plane view

Figure 6: Mean velocity vector profile of piping flow measurement.

5. Summary

The new sensor configureation of four elements array has been proposed and the measuremetn hardware system has been developed. Through the experiment of piping flow measurement, we confirmed that it can be obtain 3-D veloctiy vector profile on main lobe beam. In the future, we validate the measurement accuracy of this system, and continue improvement the 3-D flow vector measurement in the view point of hardware, signal processing and sensor configuration.

References

[1] International Research Institute for Nuclear Decommissioning (IRID): Current Status of Research and Development for Decommissionig of Fukushima Daiichi Nuclear Power Plant at IRID, https://irid.or.jp/wp-content/uploads/2019/01/20190108.pdf (in Japanese), (2019).

[2] Beller, L.S. *et al.*: Design and operation of the core topography data acquisition system for TMI-2, Three Mile Island Reports (1984), GEND-INF-012, Idaho Fall, Idaho, USA.

[3] Takeda Y: Development of an ultrasound velocity profile monitor, Nuclear Engineering and Design 126 (1991), 277-284.

[4] Nishiwaki R, *et. al*: Development of a Remote Water Leakage Localization System Combined with Phased Array UVP and Robot, 11th International Symposium on Ultrasonic Doppler Methods for Fluid Mechanics and Fluid Engineering (2018), 88-91.

[5] Peronneau P, *et al*: Blood flow patterns in large arteries, Ultrasound in Medicine (1977), 1193-1208.

[6] Fox M D & Gardiner MW: Three-dimensional Doppler velocimetry of flow jets, IEEE transactions on biomedical engineering 35(1988),834-841.

[7] Dunmire B L, *et al.*: A vector Doppler ultrasound instrument, In Ultrasonics Symposium, Proceedings (1995), 1477-1480.

[8] Huther D & Lemmin U: A constant-beam-width transducer for 3D acoustic Doppler profile measurements in open-channel flows, Measurement Science and Technology (1998).

[9] Obayashi H, *et al*: Velocity vector profile measurement using multiple ultrasonic transducers, Flow Measurement and Instrumentation 19 (2008),189-195.

[10] Owen J T, *et. al*: Development of New Ultrasonic Transducer for Multi-Dimensional Velocity Profile Measurement Using Ultrasonic Doppler Method, 11th International Symposium on Ultrasonic Doppler Methods for Fluid Mechanics and Fluid Engineering (2018), 40-43.

[11] Kasai C, *et al*: Real-time two-dimensional blood flow imaging using an autocorrelation technique. IEEE Transactions on sonics and ultrasonics, 32(1985), 458-464.

25 Optimal Vessel Materials for Indirect-contact Ultrasound Measurements

13th International Symposium on Ultrasonic Doppler Methods for Fluid Mechanics and Fluid Engineering
Zürich, Switzerland (13.-15. June 2021)

Optimal Vessel Materials for Indirect-contact Ultrasound Measurements

Bitong Wang[1], Douglas H. Kelley[1]

[1] Department of Mechanical Engineering, University of Rochester, Rochester, New York 14627, U.S.A.

Ultrasound can be used to detect small impurities or bubbles in opaque fluids, such as liquid metals, and measure fluid velocity based on the Doppler Effect. Ultrasound transducers, however, cannot always tolerate direct contact with the test fluid. When performing indirect-contact ultrasound measurements, a suitable vessel material is a prerequisite for good acoustic coupling and thus accurate flow measurement. Here, we present an experimental study focusing on finding the optimal vessel materials for applying indirect-contact ultrasound measurement in liquid gallium. We investigate the effects of the type, thickness, and wettability of vessel materials on ultrasound measurements. Our results suggest that the intensity transmission coefficient alone cannot predict the sound transmission behaviors accurately. Particularly in gallium, wetting plays an important role. Velocity measurements are less sensitive to the choice of vessel material than echo intensity measurements.

Keywords: Ultrasound Doppler velocimetry, Liquid metals, Acoustic coupling, Wetting, Indirect-contact ultrasound measurement

1. Introduction

Ultrasound is a powerful technique for studying the flow in a variety of fluids, especially in liquid metals [1-5]. In the past thirty years, ultrasound Doppler velocimetry (UDV) has been widely applied to industrially-motivated studies, such as measuring flow structures of metal melts in casting molds [6] and liquid metal batteries [7]. Besides measuring the flow velocity, ultrasound is also used to detect bubbles, impurities, and solid/liquid interfaces [8,9].

The working principles of ultrasound detection and ultrasound Doppler velocimetry have been introduced in detail in previous works [1,10]. As the UDV is not fully contactless, to transmit the sound waves from the ultrasound transducer into the test fluid, a continuous acoustic path is required [3]. Therefore, ultrasound transducers are usually inserted into the test fluid directly; we call this direct-contact measurement. However, the ultrasound transducer cannot always tolerate direct contact with the test fluid due to some restrictions of the experimental setup. Especially when the test fluid is metal melt, particular challenges are presented. First, the high temperature and corrosion of metal melts could damage transducers or destroy the piezoelectric materials. Second, as a foreign substance, the transducer itself might contaminate the metal melt. Third, since most of the commercially available UDV transducers are designed for water-based fluids, their acoustic coupling to liquid metals is often poor. In fact, most ultrasound studies of liquid metals were conducted using transducers designed for water. Acoustic waveguides provide one solution, but they reduce the signal quality significantly [3], and the restrictions of experimental setup persist. An alternative is to place the ultrasound transducer outside the vessel of the test fluid; we call this indirect-contact ultrasound measurement.

Indirect-contact ultrasound measurement has been widely used for studying flows in many kinds of fluids, especially in liquid metals. Unlike with direct-contact measurement, the ultrasound waves must pass through an additional layer, the vessel wall, in the indirect-contact measurement. Obviously, the existence of the wall would affect the ultrasound measurements. In previous studies, a variety of materials have been used for the vessel. However, we are unaware of any prior publication that systematically studied the effect of different vessel wall materials on sound transmission and thus ultrasound measurement quality, either in water or in liquid metal.

In the indirect-contact measurement, an acoustic coupling medium should be used for achieving a continuous, low-loss acoustic path between the transducer and the vessel wall. The existence of vessel wall will induce two extra interfaces in the ultrasound path: the acoustic coupling medium/vessel wall interface and the vessel wall/test fluid interface. The acoustic coupling condition at each interface depends on the acoustic impedance $Z = c\rho$, where c is the sound speed and ρ is the density. Usually, good acoustic coupling occurs when the acoustic impedance mismatch is small. The effects of impedance mismatch on ultrasound transmission through two interfaces is expressed by [11]:

$$T_I = \frac{4}{2+\left(\frac{Z_3}{Z_1}+\frac{Z_1}{Z_3}\right)\times cos^2\frac{2\pi f L}{c_2}+\left(\frac{Z_1 Z_3}{Z_2^2}+\frac{Z_2^2}{Z_1 Z_3}\right)\times sin^2\frac{2\pi f L}{c_2}} \qquad (1)$$

where T_I is the intensity transmission coefficient, Z_i are the acoustic impedances (i=1: acoustic coupling medium, i=2: vessel material, i=3: test fluid), c_2 is the sound speed in the vessel material, and L is the thickness of vessel wall.

In Eq. (1), when L equals an integer multiple number of half-wavelengths, ($L = (n/2)\,\lambda$), the Z_2 term is eliminated, so that the vessel wall is predicted to be irrelevant. In this case, the transmission strength matches that of a sound wave transmitted into the test fluid directly. Interestingly, when L equals an odd number of quarter wavelengths ($L = (2n-1)\lambda/4$) and $Z_2 = \sqrt{Z_1 Z_3}$, then the T_I equals 100%. Thus, a material whose acoustic impedance equals the geometric mean of the impedances of the acoustic coupling medium and test fluid is predicted

to maximize the acoustic transmission. A wall made from such a material is called a matching layer [11].

Note that the Eq. (1) was originally developed for liquid phases. When an acoustic wave is normally incident on an interface, many solids obey the same equation [11], but other factors should be considered. For example, wetting becomes a key factor that determines the continuity of the acoustic path between the vessel and test fluid. This is especially true when the test fluid is a liquid metal, because metals have unusually high surface tension. The high surface tension tends to prevent liquid metal from wetting the vessel wall thoroughly, which would cause some air pockets left between the liquid metal and vessel wall. As the acoustic impedance mismatch between gas and liquid is huge, the air gaps will reflect ultrasound waves strongly. Therefore, if poor wetting forms air gaps, even small ones, ultrasound transmission is severely impeded.

We experimentally studied the effects of the vessel materials on ultrasound measurements in liquid gallium. To better understand the ultrasound transmission through a wall, the influences of wall thickness and wetting were investigated. Our results show that in practice, Eq. (1) is not accurate enough to predict which vessel material is optimal. Going beyond Eq. (1), we used contact angles to evaluate the wetting condition, which plays an important role in the ultrasound measurements.

2. Experimental methods

To investigate the effect of vessel material, we used test plates of various materials to perform indirect-contact ultrasound measurements. Figure 1 shows a schematic diagram of the experimental apparatus. A slot near the front wall of the container allowed test plates to be inserted. The apparatus also allowed measurements without any test plate in place, which are used for reference. Two ultrasound transducers with working frequency of 8 MHz (Signal Processing, Switzerland) were placed on the two opposite walls of the container and fixed by swage fittings. The transducer placed on the front wall was connected to a DOP3010 Velocimeter (Signal Processing, Switzerland) and operated in emit/receive mode for data acquisition. During experiments, this transducer was inserted into the acoustic coupling medium until gently touching the test plate. For each test, 1000 UDV profiles were recorded, and the averaged values were used as the final data for echo intensity and flow velocity, respectively. In all UDV measurements, a time gate compensation (TGC) with a uniform magnitude was applied to compensate the sound attenuation in fluid. The second transducer placed on the container's back wall was connected to an oscilloscope (Teledyne LeCroy, U.S.A.) and served as a hydrophone to measure the sound pressure at the backwall position. The pressure measurements were stored and displayed on the oscilloscope.

We used liquid gallium (60°C) as the test fluid and deionized water as the acoustic coupling medium. Flow was driven by a rotating magnetic field generated by a stir plate beneath the container. To produce the similar flow for all tests, both the position of the container on the stir plate and the rotating speed were kept constant.

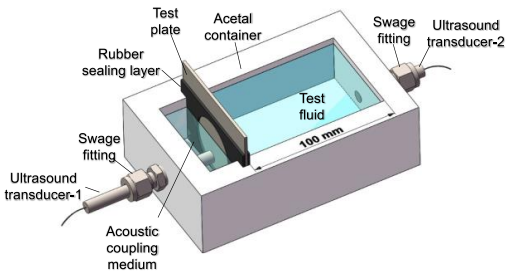

Figure 1: Experimental setup. The slot near the front wall of the container positions the test plate and rubber sealing layers. Transducer-1 was located on the front wall of the container and connected to the ultrasound velocimeter. Transducer-2 was located on the back wall of the container and connected to an oscilloscope.

The test plate materials we selected for liquid gallium are listed in table 1. Those materials were selected as they have been widely used as the vessel material in previous studies of gallium [5,6,9,12,13]. The thickness of each plate is listed in table 1. The thicknesses of selected test plate materials are near-integer multiples of half-wavelengths, except for nylon. The thickness of the nylon plate was chosen to be an odd number of quarter-wavelengths, since nylon has approximately the right acoustic impedance to be the matching layer.

Table 1: Test plate materials selected for liquid gallium

Vessel Materials	Thickness/ half-wavelength	Intensity transmission coefficients	Contact angle
Acrylic	1.48	30.27%	97° ± 4.20
Nylon 6/6	2.23	95.81%	130° ± 2.92
Borosilicate glass	4.71	45.23%	109° ± 8.06
Copper	0.49	29.38%	124° ± 7.46
Steel	0.52	27.85%	121° ± 4.71

As mentioned above, the wetting condition becomes important when ultrasound waves pass through a solid-liquid interface. Contact angles are usually used as the primary data in wettability studies, which indicate the degree of wetting between a liquid and solid [14]. In this study, to investigate the influence of wetting, the contact angles between each test plate material and gallium were measured by static sessile drop method [15] with a goniometer (AST Products Inc., U.S.A. For each test plate, the contact angle measurement was repeated five times; the average values are listed in table 1.

We also calculated the theoretical acoustic intensity transmission coefficients for each test material in gallium, by Eq. (1), and the results are listed in table 1 as well. Since the UDV transducer is designed for water, we assumed a 100% sound transmission rate from the transducer to the acoustic coupling water.

3. Results and discussion

Figure 2 shows the time-averaged echo intensity measured in liquid gallium with different test plate materials. The echo intensity of direct-contact measurement, without any test plate, is shown for reference. All selected test plate materials allowed detection of the loud echo from the back wall of the container, evident as a large peak at about 100 mm in the figure. In addition to detecting large interfaces, ultrasound has the potential to detect echoes reflected from small particles or bubbles suspended in the bulk of the fluid, which is also necessary for measuring fluid velocity. The acrylic test plate transmitted the strongest bulk echo signals, even stronger than the direct contact. Comparing with Table 1, though nylon is predicted to have the highest transmission coefficient, figure 2b shows that the nylon test plate did not transmit signals as strongly as the acrylic test plate. This discrepancy can be explained by wetting. The measured contact angle between the transducer surface material (Epotek epoxy) and liquid gallium is 137°, which means that wetting in direct-contact measurement is poor. The contact angle between nylon and gallium is similar (130°). So with nylon, wetting is similarly poor and the measured echoes have the similar strength as the direct contact, as shown in figure 2b. Acrylic, however, wets gallium much better, as indicated by its lower contact angle (97°). Thus, wetting, which determines the continuity of the acoustic path, seems to explain why indirect measurement through acrylic produces stronger echoes than the direct measurement.

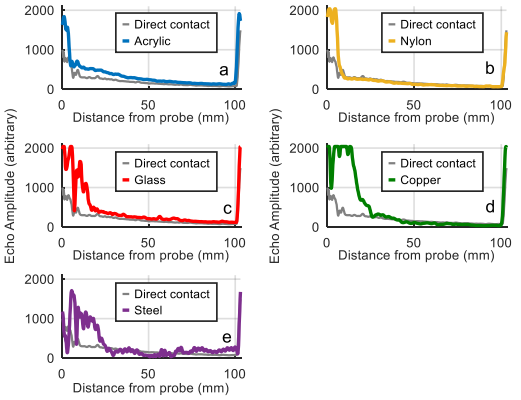

Figure 2: Time-averaged echo intensity measured in gallium with different test plate materials. Results suggest that acrylic has a better performance in terms of sound transmission into liquid gallium than other materials, even better than the direct-contact measurement.

Figure 2 also shows that all test plate materials have induced strong artificial echoes near the transducer surface (0 mm). Those echoes are caused by the acoustic impedance mismatch among acoustic coupling medium (transducer surface), test plate, and test fluid. We refer to these strong echoes as front-wall noises. However, under the same TGC parameter, the front-wall noises are weak and mask bulk echo measurements for only about 5~10 mm when the test plate is plastic; when it is metal, front-wall noises are stronger and mask nearly 30 mm, as shown in figure 2 d-e. Those noises seriously affect the ultrasound measurement. As shown in figure 2e, the steel plate also produces many undesirable artificial peaks appearing in the bulk part of the curve. Those artificial peaks are explained by reverberation artifacts that occur when sound waves reflect repeatedly within the metal plates. Many reflections can occur because the metals have small acoustic damping coefficients, so sound waves are attenuated little as they traverse the metal.

Figure 3 shows the transient sound pressure measured by the transducer located at the back wall. Comparing with the reference (direct contact) pressure curve, more noises appeared in sound pressure curves (at times greater than 2 ms) of glass and metal test plates. In addition, figure 3e clearly shows that the sound pressure is weakened by the steel test plate. Interestingly, for the borosilicate glass test plate, although the echo profile shows strong artificial noises near the transducer surface (figure 2c), the measured bulk echo intensity and sound pressure (figure 3c) are better than that of direct contact. This may be explained by the high predicted transmission coefficient and relatively small contact angle between the borosilicate glass and liquid gallium.

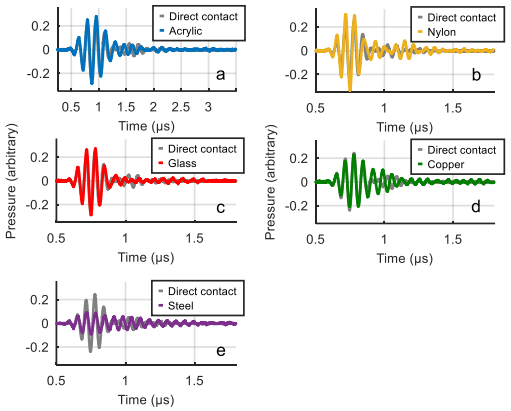

Figure 3: Sound pressure measurements in gallium with different test plate materials. Each curve describes a transient pressure waveform in one pulse duration. More reverberation noises appeared within the metallic materials data.

Figure 4 shows the time-averaged flow velocity measured in liquid gallium with different test plate materials. All measured flow patterns are almost the same as for direct contact. However, the steel plate caused such strong reverberations that velocity could not be measured within 25 mm of the transducer. It seems like the velocity measurements are less sensitive to the choice of wall material than echo intensity measurements.

Considering the echo intensity and flow velocity results, as well as the machineability of the material itself, we would suggest using acrylic as the vessel material for ultrasound indirect-contact measurements in liquid gallium. Borosilicate glass could be used for high-temperature applications. If the purpose is only to detect large interfaces or measure a simple flow, stainless steel

might also be a choice. However, copper is not recommended, since a slow reaction with gallium has been observed in our experiments. Our measurements suggest that wetting plays an important role in experiments with liquid gallium. During the experiment, we also observed that the gallium oxide layer formed at the gallium-vessel interface is likely to improve the wetting. However, this oxide layer would also intensify front noises and degrade ultrasound signals when it became thicker [4, 5].

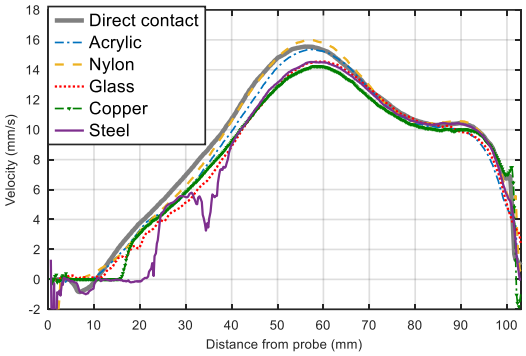

Figure 4: Time-averaged flow velocity measured in gallium with different test plate materials. All selected materials could allow ultrasound velocity measurements in liquid gallium, and the measured mean flow structures are close to the reference data.

To further explore the effect of wetting on ultrasound transmission, two steel plates with different surface roughness were used for ultrasound measurements in gallium. As shown in figure 5, the contact angle between gallium and smooth steel is 121°, small enough that the gallium droplet spreads across the surface somewhat. With roughened steel, however, the contact angle is so large (164°) that the gallium hardly wets the surface at all. Thus, we would expect better acoustic coupling between gallium and smooth steel than roughened steel. That expectation is confirmed by figures 5(b) and (e), which show weaker reverberation noises and a much stronger back-wall echo with smooth steel plate. Little useful information is contained in the echo signals measured through roughened steel plate. Consequently, no real velocity is measured; only noise appears in figure 5(f).

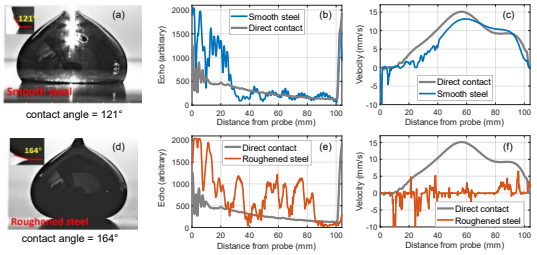

Figure 5: Wetting experiments in gallium: (a) and (d) show the measured contact angle between a gallium droplet and steel plate; (b) and (e) show the time-averaged echo intensity; (c) and (f) show the time-averaged flow velocity. Gray curves are obtained from direct contact measurement and are used as reference. Roughened steel has a large contact angle with gallium and caused poor ultrasound measurements.

4. Summary

By carefully choosing the vessel material, indirect-contact ultrasound measurements can achieve the same or better measurements quality than direct contact. In this work, we experimentally studied the effect of vessel wall material on ultrasound transmission performance when using indirect-contact ultrasound measurements in liquid gallium. Through our study, we found that the calculated intensity transmission coefficients alone cannot predict the sound transmission precisely. In real measurements, especially when the test fluid is liquid metal, the wetting condition between vessel material and test fluid changes the acoustic coupling, as can be predicted from contact angles. For the same type of material, the surface roughness, which is one of the factors that determine its wetting properties, would affect acoustic coupling and thus ultrasound transmission. Therefore, proper surface treatments are desirable to achieve good ultrasound measurements.

References

[1] Takeda Y: Velocity profile measurement by ultrasonic Doppler method. Experimental Thermal and Fluid Science, 1995.10(4): p. 444-453.

[2] Tasaka Y, *et al.*: Ultrasonic visualization of thermal convective motion in a liquid gallium layer. Flow Measurement and Instrumentation, 2008. 19(3): p. 131-137.

[3] Eckert S, *et al.*: Velocity measurement techniques for liquid metal flows. 2007.

[4] Cramer A, *et al.*: Local flow structures in liquid metals measured by ultrasonic Doppler velocimetry. Flow Measurement and Instrumentation, 2004. 15(3): p.145-153.

[5] Brito D, *et al.*: Ultrasonic Doppler velocimetry in liquid gallium. Experiments in Fluids, 2001. 31(6): p. 653-663.

[6] Timmel K, *et al.*: Experimental Investigation of the Flow in a Continuous-Casting Mold under the Influence of a Transverse, Direct Current Magnetic Field. Metallurgical and Materials Transactions B, 2011.42(1): p. 68-80.

[7] Ashour R.F, *et al.*: Competing forces in liquid metal electrodes and batteries. Journal of Power Sources, 2018.378: p. 301-310.

[8] Vogt T, *et al.*: Detection of gas entrainment into liquid metals. Nuclear Engineering and Design, 2015.294: p. 16-23.

[9] Thieme N, *et al.*: Ultrasound Flow Mapping for the Investigation of Crystal Growth. IEEE Transactions on Ultrasonics, Ferroelectrics, and Frequency Control, 2017.64(4): p. 725-735.

[10] Perez A & Kelley D.H: Ultrasound velocity measurement in a liquid metal electrode. Journal of Visualized Experiments, 2015. 2015(102): p. 1-12.

[11] Kinsler L.E: Fundamentals of acoustics. 4th ed. 2000, New York: Wiley.

[12] Aubert J, *et al.*: A systematic experimental study of rapidly rotating spherical convection in water and liquid gallium. Physics of the Earth and Planetary Interiors, 2001.128(1): p. 51-74.

[13] Eckert S & Gerbeth G: Velocity measurements in liquid sodium by means of ultrasound Doppler velocimetry. Experiments in Fluids, 2002. 32(5): p. 542-546.

[14] Yuan Y & Lee T.R: Contact angle and wetting properties, in Surface science techniques. 2013, Springer. p. 3-34.

[15] Clegg C: Contact Angle Made Easy. 2013, Carl Clegg: Netcong, NJ. p. 4-10.

26 Flow process and rheology control by Ultrasound-Doppler along the food value chain from material pre-processing to gastro-intestinal digestion

13th International Symposium on Ultrasonic Doppler Methods for Fluid Mechanics and Fluid Engineering
Zürich, Switzerland (13.-15. June 2021)

Flow process and rheology control by Ultrasound-Doppler along the food value chain from material pre-processing to gastro-intestinal digestion

Erich Windhab[1], Yasushi Takeda[1], Damien Dufour[2], Kim Mishra[1], Samsun Nahar[3] and Beat Birkhofer[4]

[1] ETH Zürich (ETH); Food Process Engineering (FPE); Schmelzbergstr.9, CH-8092 Zürich, Switzerland
[2] Ubertone, 67300 Schiltigheim, France; 14, rue du Brochet, 67300 Schiltigheim-Strasbourg, France
[3] Sheffield Hallam University, Howard Street, Sheffield S1 1WB, United Kingdom
[4] Swiss Re Risk Engineering Services, Swiss Re AG, Mythenquai 50/60, 8022 Zürich, Switzerland

Ultrasound-Doppler has proved to be a powerful in-line measuring technique for non-invasive flow mapping as well as for the characterization of complex fluid rheology in processing flows. Accordingly, it has been exemplary applied along a main part of the value chain for the manufacture of chocolate confectionery from pre-crystallization, emulsification or aeration/foaming to 3D-Printing and molding. During subsequent cooling and solidification Ultrasound attenuation measurements enabled us to characterize structure formation and detachment from the mold walls. After melting during oral processing US-Doppler measurements were readdressed for in vitro studies of the flow characteristics in the oro-gastro-intestinal processing steps of swallowing, gastric mixing/dispersing and duodenal passage. For this, functional models of the human esophagus, stomach and duodenum were designed, and characteristic flow situations explored by Ultrasound-Doppler measurements. It was demonstrated that results from such measurements complemented well to the derivation of process-structure-property (S-Pro2) relationships for each of the considered processing steps. Such allow further integration into an "S-Pro^2 cascade" from which a reverse engineering approach could be derived, thus facilitating the adjustment of targeted consumer-relevant sensory and digestion patterns. This is of interest for the development of chocolate confectionery with low calorie density and a slowed kinetics of the adjustment of the glycemic index in the blood serum phase.

Keywords: Ultrasound-Doppler, flow mapping, in-line rheometry, multiphase food dispersions, oro-gastro-intestinal processing, in vitro models, esophagus stomach and duodenum

1. Introduction

To gain an authentic insight into flow processes in which complex fluid system structures are generated or transformed due to the acting flow stresses, non-invasive in-line measurements of the velocity field are required. In case of laminar flow fields in viscous, non-Newtonian and non-transparent fluid systems Ultrasound Doppler Velocimetry (UVP) has proved to be a powerful tool to not only allow for flow mapping, but also enable in-line rheometry if rheometric flow conditions (stationery plane layer flow) are present [1]. Such exist in cylindrical pipe flow which is in general an indispensable element in flow processing plants. If the viscosity function has been measured as described before once for a certain structural steady state of a non-Newtonian fluid system, locally acting shear stresses and related viscosities acting in more complex laminar velocity fields of such fluid system (as e.g detected by US-Doppler flow mapping), can be determined [2].

With the work presented here, we wanted to exemplarily highlight the versatility of the ultrasonic Doppler technology in its application over a larger part of the value chain for the production, consumption and digestion of chocolate confectionery. Accordingly the flow processing steps of (i) pipe transport, (ii) seed and shear pre-crystallization, (iii) micro-foaming, (iv) molding/3D-printing, (v) swallowing (esophagus transport) , (vi) gastric dispersive mixing and (vii) duodenal transport by peristalsis are followed with major focus on flow mapping for (ii), (iii), (v), (vi) and (vii) and rheological measurements in cylindrical pipe flow sections for (i) before and after (ii).

2. US-Doppler in process flow analyses

2.1 Steady state in-line pipe flow rheometry

In cylindrical pipe flow at Reynolds numbers Re < 2300, the acting shear rate distribution can be calculated from the first derivative of the radial velocity distribution as:

$$\dot{\gamma}(r) = dv(r)/dr \qquad (1)$$

Since, as derived from momentum balance, the radial shear stress distribution $\tau(r)$ in laminar cylindrical pipe flow is a linear function of the radius r as well as of the acting pressure gradient dp/dx but in-dependent of the fluid rheology:

$$\tau(r) = 0.5\, r\, dp/dx \qquad (2)$$

$$\tau(r) = \eta(r)\, dp/\gamma. \qquad (3)$$

simple static pressure difference detection at the pipe wall (r = R) over a defined length dx of such pipe, gives access to the wall shear stress and the radial shear stress distribution. Based on Newton's shear stress law the fluid viscosity function is received in the shear stress range of $0 \le \tau < \tau(R)$ which in case of non-Newtonian fluids means that within a substantial shear rate range the shear rate dependent viscosity function $\eta(\gamma)$ is smartly received from steady state pipe flow [1,3]. Figure 1 shows the setup for UVPPD (**c**: UVP and USA measuring cell; **e**: UVP + pressure difference PD) in-line pipe rheometry and measured velocity profile (**a, d**) and a shear viscosity function for a non-Newtonian (shear-thinning) suspension of a chocolate confectionery palm fat with crystalline solid fat con-

tent of 3.9 wt.% (**b**). The needle-like fat crystal morphology causes the pronounced shear thinning flow behavior at rather low crystal concentration [3].

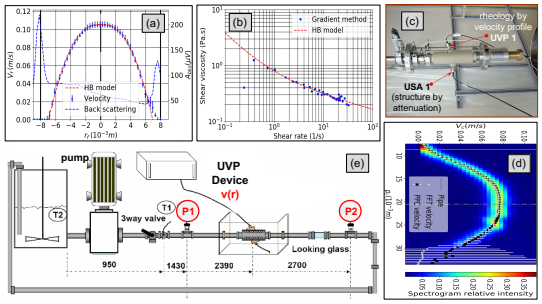

Figure 1: Velocity profile (a,d) and shear viscosity function of conventionally pre-crystallized palm fat with 3.9% SFC (NMR) at 30 kg/h mass flow rate and 26°C, measured in-line by UVP transducer (4 MHz) in experimental pre-crystallization loop schematically shown in (e) [3,4].

2.2 UVPPD rheometry in continuous crystallization process of cocoa butter / chocolate

A UVPPD measuring cell was integrated into a continuous process of cocoa butter/chocolate processing, starting with a batch pre-crystallization step (a) to adjust stable crystal $\beta_{V/VI}$ polymorph structure, followed by a 2nd continuous crystallization step in a surface scraped heat exchanger (SSHE) (b) after which the UVPPD cell (c) was placed for temperature-controlled adjustment of crystal fraction ϕ_{SFC} and related shear viscosity function $\eta(\gamma)$ (Figure 2) [5].

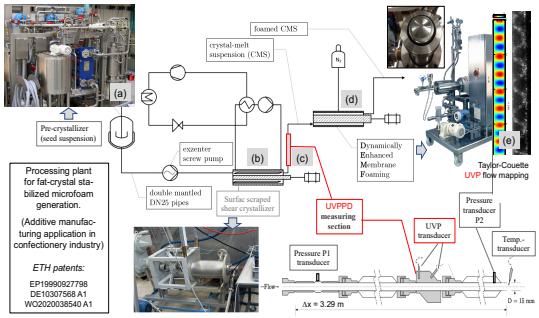

Figure 2: Processing setup for micro-foamed chocolate and fat-based filling masses consisting of: a seed-pre-crystallizer (a), an SSHE crystallizer (b), a UVPPD in-line viscosity measuring cell (c) and a Dynamically Enhanced Membrane Foaming device (d), the latter applying a Taylor-Couette flow field (e) for narrowly size distributed, stable micro-foam structure generation [5].

Figure 3 demonstrates the impact of advancing crystallization with increasing crystal fraction from ϕ_{SFC} = 1.73 to 8.8% on the UVPPD-measured velocity profiles. As has been shown by Mishra [5] for micro-foam formation the fat crystal fraction and the crystal shape are decisive for interfacial and matrix stabilization of gas bubbles thus being a prerequisite for the generation of stable but still flowable/moldable micro-foams of industrial relevance for chocolate confectionery and fat-based filling masses.

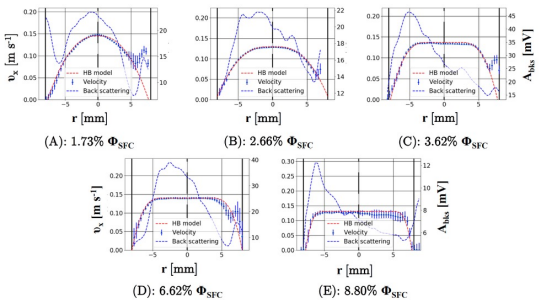

Figure 3: UVPPD-measured velocity profiles for cocoa butter crystal melt suspensions (CB CMS) crystallized at 2150s^{-1} (SSHE) in the process shown in Fig.2 with velocity scale on left y-axis and backscattering amplitude A_{bks} on the right y-axis as function of the pipe radius r [5].

2.3 UVP-flow mapping of Taylor-Couette flow in dynamic membrane foaming

A so-called Dynamically Enhanced Membrane Foaming (DEMF) device is shown in Figure 2 (d) for micro-foaming of chocolate or fat filling confectionery masses in their pre-crystallized state. In such apparatus the outer cylindrical wall of a concentric cylinder arrangement is formed by a sintermetal micro-membrane of 3 µm mean pore size. The inner cylinder is rotated between ca. 10^3-10^4 rpm thus generating high wall shear stress to detach gas bubbles of well-defined size from the membrane surface and mix them into the (pre-crystallized) fluid system which flows axially though the concentric shear gap of 0.5-5 mm width.

Axially oriented US-Doppler (UVP Duo, MetFlow) measurements allowed us to map the Taylor-Couette flow pattern under steady, wavy and modulated Taylor vortex acting conditions (see Fig. 2 (e)) and optimize gas bubble detachment from the membrane surface under adjusted oscillatory wavy Taylor vortex conditions [6].

2.4 US-attenuation measurement in molded chocolate during solidification crystallization

The application of US attenuation measurements in order to detect fat crystal networking during solidification crystallization of molded chocolate masses during continuous cooling in industrial cooling tunnels has demonstrated to allow for further viscosity and elasticity monitoring until the molded solidified product detaches from the mold wall. The latter happens as a consequence of the volume shrinkage of confectionery fats during their solidification crystallization, which is an important characteristic to enable proper demolding. Figure 4 (a) demonstrates the US-transmitter/receiver installation in a Makrolon chocolate mold and the characteristic US attenuation (US amplitude damping) pattern during chocolate mass solidification and final detachment from the mold wall. During solidification crystallization domains of initially (i) increasing viscosity and

subsequent (ii) increasing elasticity upon crystal network formation were distinguished since increase in viscosity leads to increased US-amplitude damping, whereas elasticity increase causes a reduction of the damping effect [7].

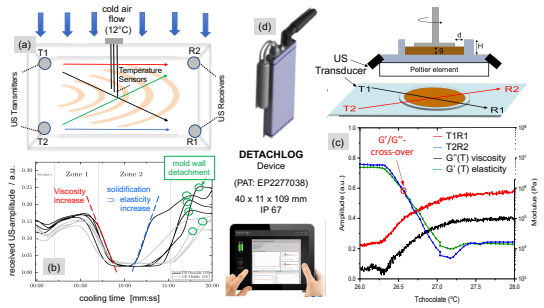

Figure 4: US-attenuation-based in-line measurement of molded chocolate solidification and mold wall detachment by ETH-Detachlog (d): (a) US transmitter/receiver placement at chocolate mold bottom; (b) US-amplitude attenuation with differentiation of viscous/elastic contributions; (c) detailed analysis of viscous and elastic moduli (G", G') during chocolate mass solidification [7].

2.5 US-Doppler flow mapping of esophagus flow during swallowing of non-Newtonian fluid

Food bolus transport through the human esophagus is caused by the peristaltic motion of the periodically collapsing elastic esophagus tube. Food after oral processing is typically in a liquid or semi-solid state with non-Newtonian rheological characteristics. In order to explore such non-Newtonian liquid food flow in a peristaltically collapsing elastic tube, an artificial esophagus was designed based on a "Sterling-resistor" flow setup as shown in figure 5 (a), in which an elastic silicon tube of 20 mm in diameter and a length of 40 cm was immersed in a water-filled transparent glass cylinder, with the entrance and exit sections of the tube being connected to inflow/outflow stainless steel pipes. Within such experimental device a transmural pressure gradient could be superimposed to the pressure gradient between entrance and exit of the elastic tube. If a critical value of the transmural pressure was exceeded the tube started to collapse. UVP-measured velocity profiles in to different degrees collapsed tubes, were in satisfying agreement with CFD simulated results. Valuable quantitative information on the significant influence of the non-Newtonian (shear thinning) rheological characteristics on esophagus flow have been gained, which are intended to be applied for development of rheology-optimized food products for elderly.

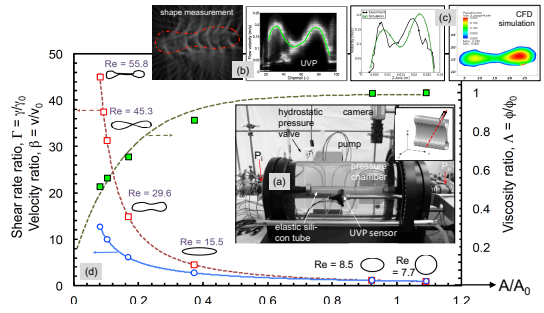

Figure 5: Experimental setup and results for artificial esophagus flow experiments in Sterling-resistor flow chamber [8]: (a) flow chamber with (i) immersed elastic silicon tube, (ii) US-Doppler transducer holder for longitudinal shift along the tube, (iii) video camera with circumferential movability for 3D-image processing of the collapsed silicon tube shape; (b) partially collapsed tube cross section and UVP detected velocity profile; (c) comparison of measured and CFD simulated velocity profiles; (d) diagram with shear rate, viscosity and mean velocity information as a function of the degree of tube collapse (expressed as cross sectional area ratio A/A_0 of the elastic tube).

2.6 US-Doppler flow mapping of gastric dispersive mixing flow

When fat continuous food systems like chocolate or fat spreads are eaten, an o/w emulsion type of 2-phase fluid system will be generated in the watery gastric juice surrounding. Depending on interfacially active components in the food and the interplay with gastric laminar and dispersive mixing, such emulsion structure can be either homogeneous or de-mixed by creaming and/or partial gelling effects. This impacts significantly on the gastric pre-digestion kinetics of the disperse fat phase with strong impact on the subsequent (final) duodenal fat digestion which in turn influences satiety.

In order to study gastric dispersive mixing flow in vitro, a functional flow model was designed for the simulation of peristaltic flow motion in the antrum. Based on fMRI images/videos the peristaltic Antrum Compression Wave (ACW) patterns were simulated.

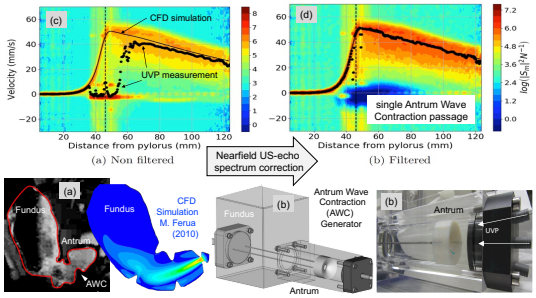

Figure 6: Flow device for in vitro testing of gastric dispersive mixing by Antrum Contraction Wave triggered flow and results from UVP flow mapping of a single ACW passage: (a) fMRI and CFD simulation as ACW study base; (b) In vitro dynamic ACW flow simulator; (c) UVP-measured velocity field in longitudinal antrum direction without "echo-correction" for the moving ACW-contour disc; (d) see (c) but with applied UVP echo correction [9].

Under the acting ACW-based dispersive mixing flow field additional simulated "fat drop" dispersing experiments were carried out and the dispersing efficiency under various ACW propagation velocity conditions and for diffe-

rent starting positions of immiscible oil droplets was systematically tested in flow experiments as well as by CFD-simulation. From these a critical dimensionless Capillary Number (Ca) was derived as denoted by equation [9],

$$Ca = \frac{R_d \tau}{\sigma} = \frac{4\eta R_d v_c RO\,(2-RO)\left[1-\frac{\delta_{apex}}{R(1-RO)}\right]^{\epsilon}}{\sigma R\,(1-RO)^3} \quad (4)$$

with R_d (drop diameter), v_c (antrum wave velocity = v_{ACW}), RO (relative occlusion = 1-Di/Da), δ_{apex} (distance from open wave contour cross section radius Ri), a (exponent), σ = interfacial tension, η (viscosity)

Figure 7 demonstrates the dependency of the capillary number experienced by the drop as function of the drop starting position. Indicated drop break-up domains are preferably related to drop-tracks passing closer to the wave contour wall and experiencing Ca-numbers ≥ ca. 0.12 (according to definition in eq. 4).

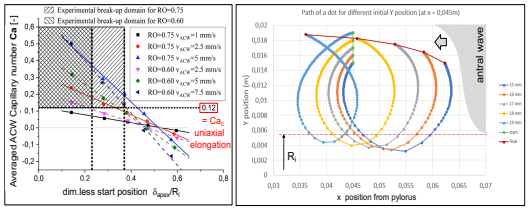

Figure 7: left: Critical Ca-number domain as a function of the starting drop position (δ_{apex}/R_i), the relative opening size of the wave contour cross section (OR) and the ACW propagation velocity (v_{ACW}); right: droplet tracks in the ACW flow field (CFD simulation) depending on the drop starting position [9].

More efficient dispersing of the fat droplets in the gastric ACW flow field, being dominated by a repulsive jet flow directed backwards from the pilorus and with high elongation rates (ε. up to ca. 5 s^{-1}) and shear rates (γ. up to ca. 10 s^{-1}), leads to the generation of an enlarged specific surface area of the oil drops which in turn leads to faster digestion in the duodenum under the action of lipolytic enzymes.

2.7 US-Doppler flow mapping of duodenal peristalsis driven intestinal juice flow

In the human small intestine, the transport of partially digested food suspensions is driven by peristaltic wave motion and /or segmentation contraction of the intestinal wall. In order to also access such flow authentically for optimized experimental in vitro simulation of digestive flow mechanisms, another "intestinal" flow device was designed as demonstrated in Figure 8. A silicon tube was immersed in a tempered transparent water bath of 1.20m in length and dynamically contracted by three roller pairs moving along the tube, with a UVP transducer connected to the roller suspension in order to keep the relative position to one selected of the roller pairs fixed, but adjustable to be directed either normal to the crest or trough section of the deformed elastic silicon tube. Flow mapping was carried out with an 8 MHz UVP transducer placed at different Positions after the roller pairs 1-3 and for different roller velocities along the tube in the range of 3 - 10 mm/s, adapted to physiological conditions of the peristaltic motion of the human small intestine (Fig. 8) [10].

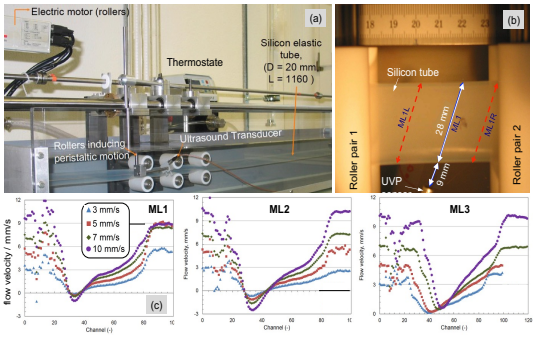

Figure 8: Small intestinal peristaltic flow testing devise with (a) intestinal tube, three contraction roller pairs and mounted UVP transducer (fixed to roller suspension, flexible for different measurement directions in the tube flow (b); (c) exemplary measured tube flow velocity profiles after each of the roller pairs (ML1-ML3) in left to right roller motion with UVP fixed in "trough" position [10].

The insight gained into experimentally approximated intestinal flow patterns will be applied for improved in vitro digestion simulation under authentically adapted flow field and flow stress conditions which impact on mixing and food structure disintegration.

3. Summary

The US-Doppler technology was approved to be a valuable tool for in-line non-Newtonian rheology measurements in rheometric pipe flow as well as for flow mapping of more complex flow situations along the chocolate confectionery food value chain from production to consumption and digestion. New insights gained into physiological flow conditions will serve for the optimization of sensory and nutritionally optimized food products.

References

[1] Windhab, E. J (1995). Rheology in food processing, chapter 5, pp. 80–116. Springer US, Boston, MA, 1995.

[2] Ouriev, B., Windhab E. (2004); Measurement Science and Technology, 14(11):1963-1972, 2004.

[3] Birkhofer, B., S. A. Jeelani, E. Windhab, B. Ouriev, J. Lisner, P. Braun, Y. Zeng (2007), Flow Measurement & Instrumentation, 19:163–169, 2007.

[4] J Wiklund, B Birkhofer, S Jeelani, M Stading, E Windhab (2012); Appl. Rheol. 22 (2012) 42232

[5] K. Mishra, D. Dufour, E. Windhab (2020); Crystal Growth & Design, 20(2):1292–1301, 2020.

[6] Pokorny L., Kohler L., Takeda Y., Windhab E. (2016); Flow Measurement and Instrumentation; 52, pp.137-143

[7] E. Windhab et al. (2012); Patent Nr. EP2277038

[8] Nahar S., Jeelani, S., Windhab, E. (2012); Chemical Eng. Science, 75:445–455, 2012.

[9] Dufour D. (2018; Dissertation ETH Zürich Nr. 24851

[10] S. Nahar, B. N. Dubey, E. J. Windhab (2019); Phys. Fluids 31, 101905 (2019); https://doi.org/10.1063/1.5123182

27 The development of ultrasonic velocity profiler for velocity vector profile measurement in bubbly flow

13th International Symposium on Ultrasonic Doppler Methods for Fluid Mechanics and Fluid Engineering
Zürich, Switzerland (13.-15. June 2021)

The development of ultrasonic velocity profiler for velocity vector measurement in bubbly flow

Wongsakorn Wongsaroj[1], Hideharu Takahashi[2], Natee Thong-un[1], and Hiroshige Kikura[2]

[1] Dep. of Instrumentation and Electronics Engineering, King Mongkut's University of Technology North Bangkok, 1518 Wongsawang, Bangsue, Bangkok 10800, Thailand
[2] Lab. for Advanced Nuclear Energy, Tokyo Institute of Technology, 2-12-1 Ookayama, Meguro, Tokyo 152-8550, Japan

In Boiling Water Reactors (BWRs), the multi-dimensional velocity distribution of the coolant in the bubbly flow region on fuel rod bundles of the reactor core is important to be elucidated by experimental investigation. The applicable measurement technique is required. To achieve this aim, this paper presents the development of an ultrasonic velocity profiler (UVP). The integration of special ultrasonic transducers and developed UVP signal processing is proposed to obtain a velocity vector of the bubbles and liquid in the bubbly flow. Firstly, the applicability of the proposed UVP was verified by the experiment in a swirling bubbly flow. The velocity vector profile measurement in bubbly flow was performed experimentally. The ability of the measurement was confirmed by comparing it with another technique. Lastly, the UVP system was applied to measure the velocity vector in the narrow flow channel in the rod bundle configuration.

Keywords: Ultrasonic, Velocity, Vector, Bubbly flow

1. Introduction

The Boiling Water Reactor (BWR) is a nuclear power plant having many operating units currently. The safety concept is the main issue for the reactor operation. The gas-liquid two-phase bubbly flow, which works as the coolant occurs in the reactor, significantly influences the safety aspect in BWR. In the reactor core, the spacer grids, which support the fuel rod bundle, are also as an effective mixing device by attaching flow deflectors such as swirling vanes. It is installed for heat transfer enhancement between fuel rod and coolant, which relates strongly to plant safety. The velocity distribution of the bubble and liquid, which has multi-dimensional motion, affects heat removal from the fuel to the coolant. Hence, the multi-dimensional velocity or velocity vector of the bubble and liquid distributed in fuel rod bundle is needed to be investigated. The experimental investigation on this parameter in rod bundles is a necessity. The measurement technique is needed.

Several intrusive techniques have been utilized to measure the velocity data in a two-phase bubbly flow, such as the conductive probe [1]. It is an intrusive method that disturbs the flow and leads to instrument lifetime distortion. Moreover, it cannot obtain liquid data. To eliminate these limitations, non-intrusive measurement techniques that can derive the velocity data of both phases have been proposed, such as Particle Image Velocimetry (PIV) [2]. It is capable of obtaining a velocity profile in two-dimensional (2D). The PIV requires optical access for the laser sheet and the camera to derive the 2D velocity profile at the region of interest, whereas the flow field in a typical fuel rod bundle with spacer-grids is optically obstructed by the rods themselves. The method cannot provide information on the full velocity profile or flow field along the flow path of rod bundles. Therefore, the measurement technique for obtaining a multi-dimensional velocity profile in this application is needed.

Ultrasonic Velocity Profiler (UVP) is a powerful method for visualizing the spatial-temporal velocity distribution in liquid flows [3]. In the UVP, the ultrasonic wave can transmit through various materials, and optical access is not required. This method is a non-intrusive measurement and can be applied to an opaque fluid.

In the UVP, an ultrasonic pulse is transmitted from the transducer along the measurement line to the liquid. The same transducer derives the echo signal reflected from the moving reflector, such as a tiny particle dispersed in the fluid. When the ultrasonic pulse is emitted repeatedly, the echo signals are obtained sequentially. Doppler signal influenced by the velocity of moving particle can be demodulated from the echo signals. The Doppler frequency $f_D(i)$ directly relates to the velocity of the particle (i is position or channel). Hence, the velocity of the particle at that position $V(i)$ can be computed as

$$V(i) = \frac{cf_D(i)}{2f_0} \tag{1}$$

where c is the sound velocity in fluid, f_0 means the basic frequency of the ultrasonic pulse, and θ is the incident angle. If the stokes number on the relation between small particles and liquid < 0.1, the particle will follow the liquid streamline. Then, if particles are dispersed in the liquid, the velocity profile of the liquid can be obtained. However, the original UVP can obtain the velocity data only in one dimension. Huther et al. [4] developed a three-dimensional velocity measurement in open-channel flow using one transmitter and four receivers, while Obayashi et al. [5] proposed a UVP system for two-dimensional measurement using one transceiver and one receiver. These techniques can obtain a multi-dimensional velocity profile. However,

they can only measure in liquid flow.

In bubbly flow, Wongsaroj et al. [6] developed the UVP method to measure a 2D velocity vector profile in open-channel flow using one transmitter and two receivers. Nevertheless, this purpose has not yet been applied in the small channel which has a narrow flow field like in the rod bundles. This paper presents the development of the UVP system to obtain the multi-dimensional velocity distribution or velocity vector of the bubbly flow in the narrow area which is applicable for experimental investigation in the rod bundle application. This study focus on two-dimensional measurement.

2. UVP measurement in bubbly flow

2.1 Single Ultrasonic gas-liquid Two-phase Separation (SUTS)

To separate the gas bubble and liquid velocity data, the phase separation algorithm is necessary. Fig. 1 illustrates the schematic of the Single Ultrasonic gas-liquid Two-phase Separation (SUTS), which is a phase separation technique. It is contained in the UVP system to separate the velocity data of both phases.

This technique is the integration of time-frequency analysis and Doppler amplitude classification [6]. Short-Time Fourier Transform (STFT) is selected to be a time-frequency estimator. It decomposes frequency components of the Doppler signal according to the time. The frequency value can be observed from peak energy occurring on spectrogram in each time location as express in equation (2) and (3).

$$X(k, f_D) = \sum_{n=0}^{N_{REP}-1} D(n)\, W_n(n - kS_n) exp(-jn2\pi f_D) \quad (2)$$

$$P(k, f_D) = |X(k, f_D)|^2 \quad (3)$$

where k is discrete-time, D(n) is Doppler signal, W_n is window length, S_n is time step, and $P(k, f_D)$ represents the energy density of spectra in time-frequency function. Then, each frequency component is classified as Doppler frequency of particle and bubble by comparing the value of Doppler amplitude in that time location with a threshold value. If the amplitude value is higher than the threshold, the frequency value will be defined as the Doppler frequency of the bubble. On the contrary, if the value is lower than the threshold, the frequency value in that location will be the Doppler frequency of particles. The Doppler frequency of bubble and liquid groups is averaged separately. Then, the velocity value of bubble and liquid can be obtained separately by placing these Doppler frequencies into equation (1).

$$V_x(i) = \frac{c}{2f_0 \sin\theta\,(i)}(f_{D1}(i) - f_{D2}(i)) \quad (4)$$

$$V_y(i) = \frac{c}{2f_0\,(1 + \cos\theta\,(i))}(f_{D1}(i) - f_{D2}(i)) \quad (5)$$

$$V(i) = \sqrt{V_x^2(i) + V_y^2(i)} \quad (6)$$

2.2 Integration of SUTS and multiple transducers for two-dimensional measurement in bubbly flow

To obtain a 2D velocity vector profile, the multiple transducers with one transmitter and two receivers are utilized, as shown in Fig. 2, which is called a multi-ultrasonic element sensor system. The receivers are employed to obtain two Doppler frequencies, $f_{D1}(i)$ and $f_{D2}(i)$, respectively, from the echo signals reflected by the reflectors along each measurement channel i with a certain echo angle $\theta(i)$. The echo angle depends on the measurement distance and transmitter-receiver gap G. To minimize uncertainty, the receiving area of receivers is designed to be small. By using $f_{D1}(i)$ and $f_{D2}(i)$ in each measurement channel, the 2D velocity vector profile can be reconstructed using equation (4) to (6).

To achieve the measurement in bubbly flow, the SUTS is integrated with a multi-ultrasonic element sensor system and applied into the UVP which is called 2D vector UVP gas-liquid separation system. It can measure the 2D velocity vector profile of bubble and liquid in the bubbly flow. Fig. 3 represents a system schematic of the integrated measurement system. The sensor system is connected to the multiple-channel pulser/receiver. The echo signals were obtained via receivers 1 and 2. The signals are amplified by pulser/receiver. The signals are sent to UVP processing, including the SUTS to compute the velocity of bubble and liquid (particle); $V_{\text{particle1}}$,

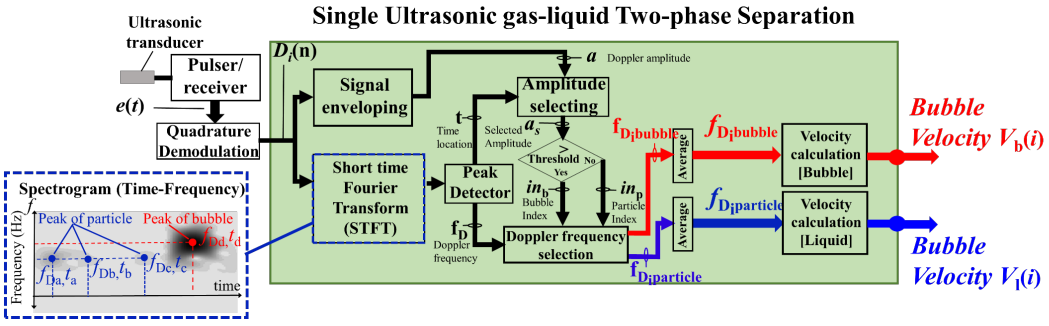

Figure 1: the schematic of the UVP with SUTS

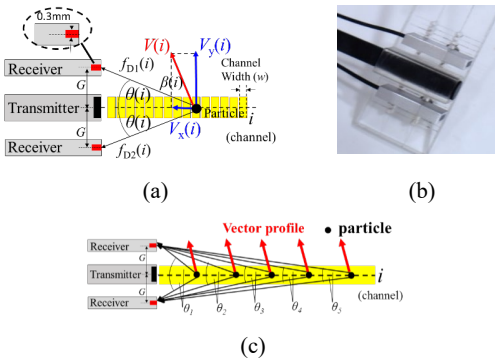

Figure 2: multi-ultrasonic element sensor system, (a) schematic of measurement with a single particle, (b) image of transducer, (c) schematic of measurement with multiple particles,

$V_{bubble1}$, $V_{particle2}$, and $V_{bubble2}$. The 2D velocity of bubble and liquid can then be reconstructed separately by the vector reconstruction section based on the equation (4) to (6).

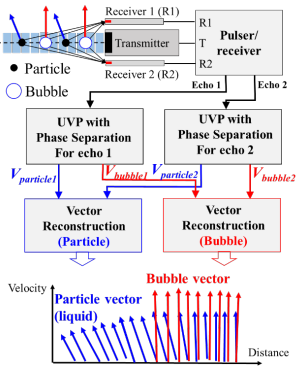

Figure 3: the schematic of the integration of UVP with SUTS and multi-ultrasonic element sensor system

3. Two-dimensional measurement in the swirling bubbly flow

In order to demonstrate the performance of the UVP, firstly, the experimental measurement was executed in the swirling bubbly flow. Fig. 4 represents a schematic diagram of the experimental apparatus and the UVP system. The UVP system consisted of a multi-ultrasonic element sensor system; one 4MHz transmitter and two 4MHz receivers, a multiple channels ultrasonic pulser/receiver, a digitizer, and a computer with LabVIEW software version 2011. The pulser/receiver emitted ultrasonic pulses via the transmitter and received the echo signals through receiver1 and receiver2. Then, the echo signals were received and amplified by the pulser/receiver. The signals were converted to a digital signal by the digitizer, with a sampling rate of 250 MS/s. Signal data from the digitizer was sent to the computer via PCI port. The signal processing and velocity computation were performed using LabVIEW software. The transducers were installed in the test section (in the water box). The pipe was made from acrylic with an internal diameter of 20 mm. Tap water at temperature 12ºC ±2ºC dispersed with nylon particles 80 µm and bubbles were working fluid. The water was circulated from the bottom to the top by the pump. The electromagnetic flowmeter was used to measure the water flow rate. A bubble generator was put on upstream 50D from the test section to generate the bubble. The swirling motion was induced by a twisted tape inserted in the acrylic pipe. The twist ratio y was set to = 3 to be the same with industrial purpose. For the UVP parameter setting, the basic frequency was f_0 4MHz with the 4 cycles per pulse, the voltage was 160 Vp-p, pulse repetition frequency f_{PRF} was 4 kHz, and the number of repetitions N_{REP} 128.

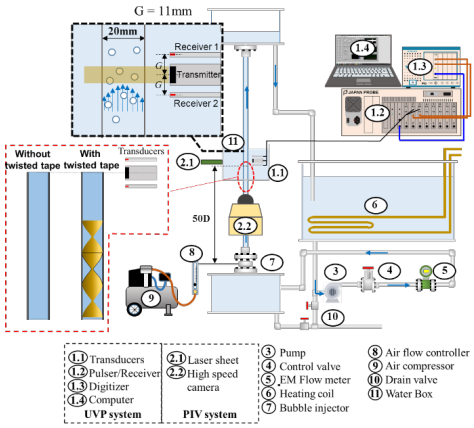

Figure 4: the schematic of the integration of UVP with SUTS and multi-ultrasonic element sensor system

In this experiment, the U_L was set at 500 mm/s, The average 2D velocity vector of swirling bubbly flow was measured by the UVP and the PIV. Fig. 5a illustrates the measurement results of the UVP. The brown color vector and the blue color vector represent the velocity vector of the bubble and liquid obtained from the UVP. The velocity vector of both phases could be obtained separately. Fig. 5b and Fig. 5c show the comparison of the velocity vector measurement with the PIV measurement; bubble and liquid, respectively. The discrepancy of comparison was almost 15%, as shown in Fig. 6. However, the bubble has a high response toward the light, the bubble outside the laser plane that moves in a not similar direction to the bubble in the plane is able to be captured and appeared on the PIV image which causes the deviation in the measurement result of tangential velocity and direction of the bubble velocity vector.

4. Measurement in the rod bundle

To achieve the target, the demonstration of 2D vector UVP gas-liquid separation system to investigate the 2D velocity vector of bubbly flow in rod bundles is required. The experiment was conducted in the rectangular column in which four rods were used to simulate to be the fuel rod bundle, as shown in Fig. 7. The rod diameter was 12 mm

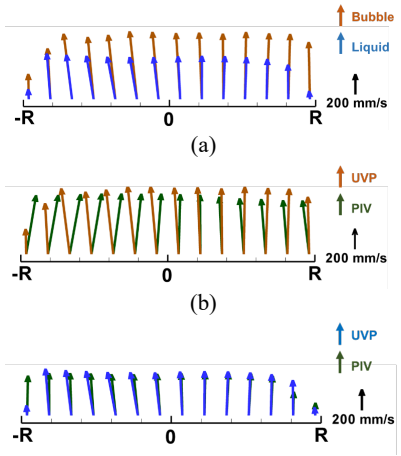

Figure 5: Measurement result in swirling bubbly flow, (a) the result of the UVP, (b) the comparison result of bubble, (c) the comparison result of liquid

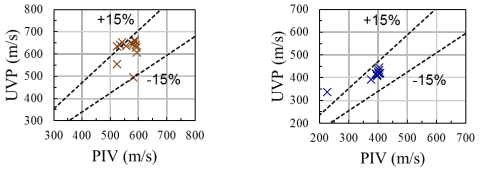

Figure 6: Discrepancy of measurement in swirling bubbly flow, (a) bubble, (b) liquid

The gap between the two rods was set at ≈ 8 mm. This configuration was referred as the experimental investigation proposed by [7]. The working fluid was tap water dispersed by nylon particle with a diameter of 80 μm and bubble generated by the bubble generator. The water was circulated from the inlet to the outlet by the pump. The 2D flow field was formed. The impeller flow meter monitored the flow rate. The transducer was immersed in the water and installed at position H = 20 mm from the outlet center. The measurement equipment and parameter setting were similar to the previous experiment.

Fig. 8 represents the measurement result of a 2D velocity profile derived from the bubbly flow distributed in the rod bundles. The profile was the average value of 5000 instantaneous profiles. The 2D velocity profile of bubble and liquid on the path between two pairs of rods can be reconstructed. The 2D velocity vector profile after the near field region to the tank wall surface was obtained. The profile of the bubble phase had a vertical rising direction, only on the right side of the profile the vector direction pointed to the outlet. The profile of the liquid phase at a distance between 30 mm and 70 mm has a direction to the outlet, indicating the reasonableness of the result obtained. It can be concluded that 2D vector UVP gas-liquid separation system is applicable to measure the 2D velocity vector profile of the bubbly flow in the rod bundles application.

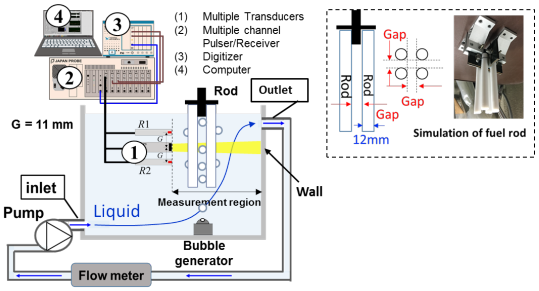

Figure 7: Experimental setup for the UVP measurement in rod bundle

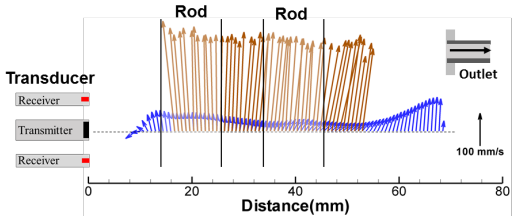

Figure 8: 2D velocity vector profile in rod bundle

5. Summary

The UVP measurement which has modified by the integration of Single Ultrasonic gas-liquid Two-phase Separation (SUTS) technique and multi-ultrasonic element sensor system was proposed to measure the velocity vector of the bubbly flow in the narrow area of rod bundles. Preliminary, the applicability of this system was verified by the experiment on a swirling bubbly flow. The 2D velocity vector profile in bubbly flow was obtained experimentally. Lastly, the UVP system was applied to measure the 2D velocity vector profile in the narrow flow channel in the rod bundle configuration. The 2D velocity vector of bubble and liquid can be derived reasonably.

References

[1] Muñoz-Cobo J. L, *et al.*: Development of Conductivity Sensors for Multi-Phase Flow Local Measurements at the Polytechnic University of Valencia (UPV) and University Jaume I of Castellon (UJI)", Sensors, 17 (2017), 1077.

[2] Lindken R, *et al.*: Velocity measurements of liquid and gaseous phase for a system of bubbles rising in water, Exp. Fluids, 29 (2000), 194-201.

[3] Takeda Y: Velocity profile measurement by ultrasonic Doppler shift method, Int J Heat Fluid Flow, 7 (1986), 313-318.

[4] Huther D, *et al.*: A constant-beam-width transducer for 3D acoustic Doppler profile measurements in open-channel flows, Meas Sci Technol, 9 (1998), 1706-1714.

[5] Obayashi Y, *et al.*: Velocity vector profile measurement using multiple ultrasonic transducers, Flow Meas Instrum, 19 (2008), 189-195.

[6] Wongsaroj W, *et al.*: 2D velocity vector profile measurement on bubbly flow using ultrasonic technique, Mech. Eng. J, 7 (2020), 19-00519.

[7] Yun B, *et al.*: Flow Structure of Subcooled Boiling Water Flow in a Subchannel of 3x3 Rod Bundles, J Nucl Sci Technol, 45 (2008), 402–422

28 An instantaneous velocity vector measurement using conventional ultrasonic transducers

13th International Symposium on Ultrasonic Doppler Methods for Fluid Mechanics and Fluid Engineering
Zürich, Switzerland (13.-15. June 2021)

An instantaneous velocity vector measurement using conventional ultrasonic transducers

Dongik Yoon[1], Hyun Jin Park[1] and Tomonori Ihara[2]

[1] Laboratory for Flow Control, Graduate school of Engineering, Hokkaido University N13 W8, Kita-ku, Sapporo 060-8628, Japan
[2] Dep. of Marine Electronics and Mechanical Engineering, Tokyo University of Marine Science and Technology, 2-1-6 Etchujima, Koto-ku, Tokyo 135-8533, Japan

A new profiling method of velocity vectors using three conventional transducers is proposed in this study. Since the conventional transducers include uncertainty for the detection points on receivers, a new configuration of transducers was constructed to minimize the uncertainty. The configuration consists of a central emitter and two side receivers. Measurable distances are theoretically determined by the configuration, thus a feasibility test for the measurable distance was firstly carried out in a towing tank facility. The distance was evaluated by measured velocities, and it was confirmed that the measurable distance agreed well with the theoretical distance. The other feasibility test was completed to assess the velocity vector measurement in the measurable distance, and the measured vectors showed a good agreement to reference values. As an application of the new method, the Reynolds stress in a turbulent pipe flow was measured, and it showed a good agreement with the PIV result.

Keywords: Ultrasound Velocity Profile, Vector profiling, Conventional transducer, Turbulent flow

1. Introduction

Ultrasound Velocity Profile (UVP) is one of the efficient measurement techniques in fluid engineering because it allows measuring opaque flows without intrusions in flow fields. Since it also provides high temporal resolution, the UVP is widely used in many fluid fields. However, a disadvantage is that only one vector on a measurement line can be obtained. Namely, it is less informative when turbulent flows are measured. In response to this problem, there are many challenges about velocity vector profiling methods called vector-UVP, and special transducers such as a focusing transducer, a phased array transducer, and an element array transducer were adopted in the vector-UVP studies [1–3]. However, these transducers also have other problems. For example, large errors in a receiver can be included with the focusing transducer. A reduction of time resolution is unavoidable in the case of phased array transducer because the phased array setup requires a certain scanning time for the measurement plane. Besides, the element array transducer has lower availability than the UVP because special transducer designs are required for each measurement cases. Additionally, expenses by the purchase of them are required, and the expenses also remind for the above-mentioned transducers. For these reasons, the vector-UVP is not commonly used in the fluid engineering fields, even though it can offer more information than the UVP. In this study, a new method for measuring velocity vectors with conventional transducers is suggested. A new configuration with conventional transducers was constructed to minimize uncertainty about the detection points on receivers. In this paper, we introduce this new methodology and show results of its feasibility tests performed in towing tank facility and a turbulent pipe flow.

2. Measurement principle

2.1 Configuration of transducer

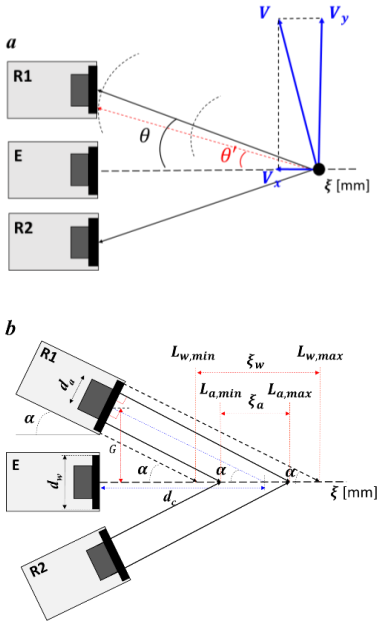

Figure 1: A measurable distance determined by the configuration of conventional transducers. E is central emitter and R1 and R2 are tilted side receivers.

In the general configuration of vector UVP with conventional transducers (Figure 1(a)), there is an uncertainty to determine the detection points on receivers because the sensor diameter of the transducer is quite large compared to measurement length. For example, the included angle between an emitted line and a reflected line

becomes θ with an assumption that the echo signals are always detected at the center points of each receiver, even though the actual angle is not θ but θ'. This uncertainty can be minimized by giving angles on the receivers as shown in Figure 1(b). With this configuration, the detecting points at the receivers can be known if we assume that the echo signal is sensed by the nearest point of receivers from the reflected point by a media, and the measurable distance (ξ_a) can be also theoretically estimated by the active diameter (d_a) of the transducer. In the measurable distance, the reflected lines are perpendicular to the receiver surface, then the angle between the emitted and the reflected line becomes the tilted angle of the transducer (α). Consequently, the vector-UVP equation can be expressed in Eq. (1) where V_{R1} and V_{R2} are receiver direction velocities.

$$V_x = \frac{V_{R1} + V_{R2}}{1 + \cos\alpha}, \quad V_y = \frac{V_{R1} - V_{R2}}{\sin\alpha} \tag{1}$$

To discuss the measurable distance in more detail, it is likely that the ultrasound detected at areas other than the d_a is transferred by oscillating a wear plate. Accordingly, a measurable distance depending on the whole diameter of the transducer (d_w) was also considered. The information about theoretical measurable distance is summarized in Table 1, and the distance between the center of emitter and center of each receiver (G) was 8.9 mm. About the conventional transducer, not only the emitter and but also the receivers were made up of TX4-5-8-40 (Met-Flow S.A) which f_0, d_a and d_w are 4 MHz, 5 mm and 8 mm, respectively.

Table 1: Geometric information about transducer configuration changed by receiver angles

	α = 5°	α = 10°
$L_{a,\,min}$ [mm]	74.2	37.0
$L_{a,\,max}$ [mm]	131.8	65.8
$L_{w,\,min}$ [mm]	57.2	28.4
$L_{w,\,max}$ [mm]	149.0	74.4
ξ_a [mm]	57.6	31.8
ξ_w [mm]	91.8	46.1

2.2 Pulsed Doppler method

The emitter was driven by a pulser/receiver (JPR-600C, Japan Probe Co., Ltd), and the echo signal received from R1 and R2 was amplified by preamplifiers (PR-60BP, Japan Probe Co., Ltd) which include band-pass filter function to improve the signal to noise ratio (SNR), and it is recorded on a memory of PC. The signal was demodulated by quadrature phase demodulation [4], and the autocorrelation method was adopted to compute a Doppler frequency (f_D). The receiver direction velocity (V_R) was obtained using Eq. (2) where c is sound speed and f_0 is the basic frequency of ultrasound.

$$V_R = \frac{cf_D}{2f_0} \tag{2}$$

3. Feasibility test

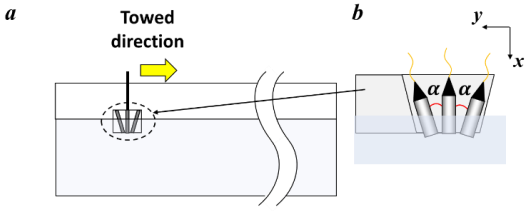

Figure 2: Schematic of experiment apparatus (a) a towing tank facility and (b) a transducer holder.

Two feasibility tests were carried out; one was to evaluate the measurable distance by α and the other was to assess the measurement of velocity vector. For these tests, a towing tank facility was utilized with a transducer holder as shown in Figure 3(a) and (b), respectively. Tracer particles were mixed in water (HP 20SS, Mitsubishi Chemical), and their density and diameter are 1010 kg/m^3 and 50–120 μm, respectively. The water temperature was 21°C.

3.2 Feasibility test for measurable distance

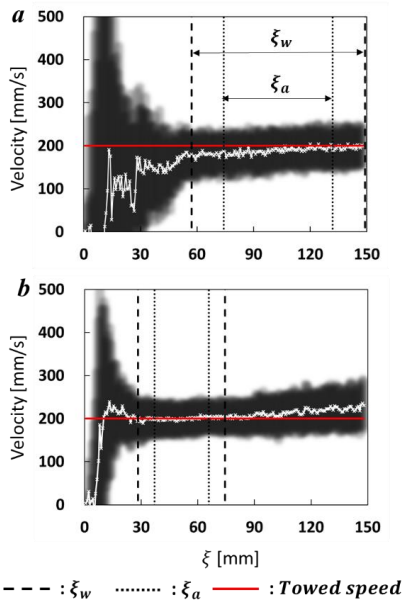

Figure 3: Time-averaged velocity (a) α = 5° and (b) α = 10°. Black region implies standard deviation.

In the feasibility test for the measurable distance, the transducer holder was submerged horizontal to the water surface as shown in Figure 3(b) and towed as 200 mm/s. The ultrasound (4 cycles) was emitted with f_0 of 4 MHz

and f_{PRF} (pulse repetition frequency) of 1 kHz, and the number of pulse repetitions in a velocity profile was 25. The fifty velocity profiles were averaged (Figure 4). In the ξ_a and the ξ_w, the measured velocity is converged well to the towed speed for each α, while it shows higher residuals in the outside of the ξ_a and the ξ_w than that in the ξ_a and the ξ_w.

$$E_R = \frac{|V - \overline{V_y}|}{V} \times 100\ [\%] \qquad (3)$$

To evaluate this result, error rate (E_R) was computed using Eq . (3), and the spatio-temporal average E_R for each α is summarized in Table 2. As the average E_R for each α is equal within the ξ_a and the ξ_w, it can be said that the ξ_w is also adopted using the TX4-5-8-40. In addition, the E_R is below in 6%, thus the measurable distance is constructed well for each α.

Table 2: Spatio-temporal averaged error rate for each α

	α = 5°	α = 10°
ξ_a	6 %	1 %
ξ_w	6 %	1 %

3.3 Feasibility test for vector measurement

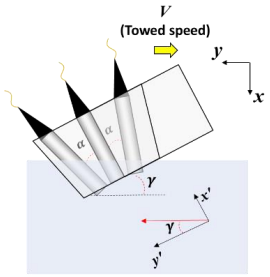

Figure 4: A virtual coordinate by tilting transducer holder.

The transducer holder was tilted with an angle γ to generate two vectors in the towing tank as shown in Figure 4. A virtual coordinate is formed with x' and y' with the γ, and the velocity in the x' and y' can be theoretically estimated by Eq. (4) where V is towed speed. In this test, the γ was 30°.

$$V_{x',\mathrm{theo}} = V\sin\gamma,\ \ V_{y',\mathrm{theo}} = V\cos\gamma \qquad (4)$$

The experimental condition is the same as to previous feasibility test other than f_{PRF} and α. The f_{PRF} was changed to 2 kHz to prevent the aliasing problem, and the α of 5° is adopted in this test. Figure 5 shows the time-averaged $V_{x'}$ and $V_{y'}$ when the γ is 30°. A red line indicates $V_{x',theo}$, and a yellow line means $V_{y',theo}$. It can be clearly recognized that $V_{x'}$ and $V_{y'}$ are converged to the theoretical value in the ξ_a and the ξ_w. To estimate the error of this result, magnitude velocity (V') was obtained and error rate (E_v) was computed using Eq. (5).

$$E_V = \frac{|V - V'|}{V} \times 100\ [\%],\ V' = \sqrt{V_{x'}^2 + V_{y'}^2} \qquad (5)$$

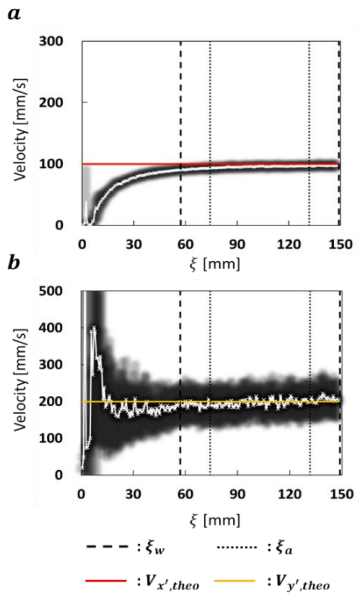

Figure 5: Time-averaged $V_{x'}$ and $V_{y'}$ when γ is 30°, and black region implies standard deviation.

The spatio-temporal averaged E_v are 2% and 1% in the ξ_a and the ξ_w, respectively. Based on this result, it is possible to say that two vectors can be obtained with low errors using the vector-UVP in time-average. Meanwhile, the condition of this experiment can be considered as a steady state flow because the towed speed is constant regardless of measurement time. Nevertheless, the standard deviation of $V_{y',theo}$ is much high, whereas that of $V_{x',theo}$ is converged to zero. This means that the fluctuations of velocity are included in instantaneous velocity profiles, and this is due to the lack of velocity resolution of $V_{y',theo}$. To explain, the velocity resolution of $V_{x'}$ ($\Delta V_{x'}$) and $V_{y'}$ ($\Delta V_{y'}$) can be expressed as Eq. 6 where ΔV_R is the velocity resolution in the beam direction. Although it is difficult to calculate the ΔV_R in the autocorrelation frequency analysis, the resolution is roughly estimated using the denominator of the equation by substituting 5° in α.

$$\Delta V_{x'} = \frac{\Delta V_R}{1+\cos\alpha},\ \Delta V_{y'} = \frac{\Delta V_R}{\sin\alpha} \qquad (6)$$

$$\Delta V_{x'} = 0.5\Delta V_R,\ \Delta V_{y'} = 11.5\Delta V_R \qquad (7)$$

As shown in Eq. (7), the $\Delta V_{y'}$ is 23 times much larger than the $\Delta V_{x'}$. For this reason, the standard deviation of $V_{y'}$ is much higher than that of $V_{x'}$. Therefore, the α should be optimized to minimize the error caused by the lack of velocity resolution considering the measurement distance.

4. Application of developed vector-UVP

As a demonstration of the developed vector-UVP, we measured the Reynolds stress in a turbulent pipe flow. A schematic diagram of experimental equipment is shown in Figure 6(a). A bent hose is connected with the inlet of a pipe as shown in Figure 6(b), and this led to asymmetric flow in the pipe. The pipe has a 50 mm inner diameter (D) and 2000 mm length (L), and the transducers and high-speed camera were installed at $L/2$. Same as to feasibility tests, HP 20SS was mixed in the water. The bulk velocity (U_{bulk}) is 1 m/s, and the Reynolds number defined as $Re = U_{bulk}D/\nu$ where ν is a kinematic viscosity is 50,000.

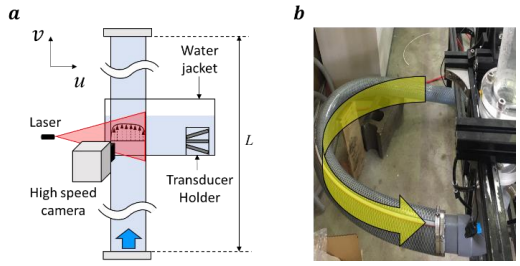

Figure 6: Experimental equipment for the measurement of Reynolds stress in a pipe flow. (a) A schematic diagram of experimental set-up. (b) A bent hose at pipe inlet. A yellow arrow indicates flow direction in the bent hose.

About measurement conditions, images of pipe flow were obtained by the camera with 1,500 fps to compare the vector-UVP and the PIV result. The ultrasounds were emitted f_0 of 4 MHz with f_{PRF} of 2 kHz. The spatial resolution is 0.74 mm, and 27 repetitions were included in a velocity profile. 500 velocity profiles were used to compute the mean velocity and the Reynolds stress, and they are shown in Figure. 7. For the time-averaged magnitude velocity (Figure 7(a)), there are small differences between the PIV and the vector-UVP up to the diameter of 24 mm, however, the velocity distributions of the two measurement systems are almost the same as each other. The magnitude velocity at a diameter of 2 mm includes erroneous data in the vector-UVP result due to the multiple reflections. As explained previously, velocity profiles by vector-UVP and PIV shows asymmetric velocity distribution because of the bent hose connected with the pipe inlet as explained previously. Generally, the Reynolds stress can be obtained from velocity profiles on multiple measurement lines of UVP, not a vector-UVP, by assuming the $\overline{u}$ becomes zero [5]. However, it is likely that the $\overline{u}$ is not zero in this asymmetric flow, and then the Reynolds stress cannot be estimated using the UVP. As two vectors in the flow field can be obtained by developed vector-UVP, the Reynolds stress can be gained in any flow condition by using the vector-UVP. To talk about the measurement result of Reynolds stress, small differences exist between the two measurement results, but they are closely agreed to each other except for the multiple reflection points. The Reynolds stress means turbulent fluctuations in fluid momentum, and instantaneous velocity profiles are required to acquire the stress. Since the Reynolds stress obtained by the PIV and the vector-UVP are consistent, the instantaneous velocities measured by the vector-UVP are statistically valid.

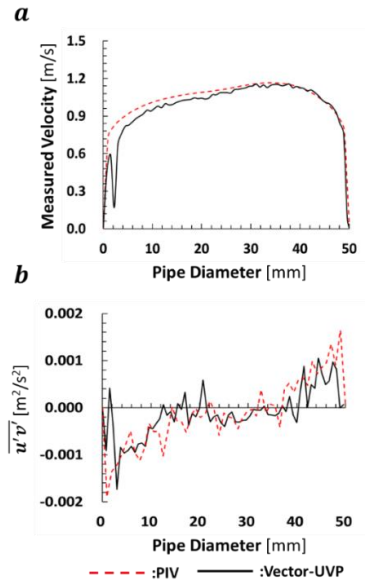

Figure 7: A comparison of vector-UVP and PIV results. (a) Time-averaged magnitude velocity and (b) Reynolds stress.

5. Summary

The new vector-UVP system using conventional transducers was successfully developed in this study. According to the angle of the receiver, the measurable distance is determined, and it was confirmed that the velocity error is below 2% in the measurable distance. In this system, the optimal angle of the receiver should be adopted considering the measurement distance because nonnegligible error can be included with the low angle which causes the lack of velocity resolution. The applicability of developed vector-UVP was examined by measuring the Renoylds stress in the turbulent pipe flow, and it shows a good agreement to the PIV result.

References

[1] H. Obayashi, *et al.*: Velocity vector profile measurement using multiple ultrasonic transducers", Flow Measure. Instrum. (2008), 19:189–195.

[2] S. Shwin, *et al.*: Two-dimensional velocity measurement downstream of the double bend pipe using phased array ultrasonic velocity profiler, Advance Exp. Mech. (2018), 3: 111–117.

[3] J.T. Owen, *et al.*: Design of new ultrasonic transducer with two elements for flow rate measurement using ultrasonic Doppler method, E3S Web Conf. (2018), 43: 01011.

[4] H. Murakawa, *et al.*: Effects of the number of pulse repetitions and noise on the velocity data from the ultrasonic pulsed Doppler method with different algorithms, Flow Measure. Instrum. (2014), 40:9–18

[5] H. Murakawa, *et al.*: Measurement of Reynolds stress in bubbly flow uisng ultrasound doppler method, 3rd ISUD, Lausanne (2002), pp 97–102.

29 Measurement System for Flow Mapping and Shape Detection using Sectorial Array Sensors

13th International Symposium on Ultrasonic Doppler Methods for Fluid Mechanics and Fluid Engineering
Zürich, Switzerland (13.-15. June 2021)

Measurement System for Flow Mapping and Shape Detection using Sectorial Array Sensors

Zeliang Zhang[1], Munkhbat Batsaikhan[2], Hideharu Takahashi[2], and Hiroshige Kikura[2]

[1] Dep. of Mechanical Engineering, Tokyo Institute of Technology, 2-12-1 Ookayama, Meguro-ku, Tokyo 152-8550, Japan
[2] Lab. for Advanced Nuclear Energy, Tokyo Institute of Technology, 2-12-1 Ookayama, Meguro-ku, Tokyo 152-8550, Japan

The Fukushima Dai-ichi nuclear power plant (FDNPP) was damaged by the Great East Japan Earthquake 10 years ago. Reactor cores of units 1, 2, and 3 were melted and large amounts of fuel debris generated to reactor pressure vessel (RPV) and primary containment vessel (PCV). Researchers have a number of measures and techniques to detect the location of fuel debris and leakage point in RPV and PCV. In recent years, ultrasonic waves, with their light-free and high radiation-resistant properties, have led researchers to propose a number of methods for the application of ultrasonic techniques to fuel debris and leakage point detection. This paper proposes a method to detect the location of fuel debris and leakage point by ultrasonic sectorial array sensors using Ultrasonic Velocity Profiler (UVP), Full Matrix Capture (FMC), and Total Focusing Method (TFM), respectively. A mock-up experiment has performed in a laboratory-scale tank where simulated fuel debris and leakage points were placed. The sectorial array sensors were applied to measure the shape of simulated fuel debris and flow around it. The results of the experiment have demonstrated that the sectorial array technique can be applied in leakage point and fuel debris detection.

Keywords: Fukushima Dai-ichi NPP, Decommissioning, UVP, Sectorial array sensors, TFM

1. Introduction

During the 2011 Great East Japan Earthquake, the Fukushima Daiichi nuclear power plant (FDNPP) suffered severe damage. The core temperature is rising because the reactor cannot be cooled properly due to power failure caused by the earthquake and tsunami coming after. That led to the melted down of core and a large amount of radioactive fuel debris was deposited through the core in the reactor pressure vessel (RPV) and primary containment vessel (PCV). After the disaster, the Japanese government has been actively organizing efforts to respond to the disaster, and in the mid- and long-term roadmap towards 1F decommissioning issued by the Japanese government in 2019 [1], the detection of fuel debris deposited in the PCVs and RPVs and leakage points on the PCVs and RPVs has become a priority for advancing the decommissioning of the nuclear power plant. In this regard, various efforts have been made, including the use of various types of robots instead of human power to enter the reactor for investigation, the use of optical equipment for investigation, etc. [2].

At same time, ultrasound has been applied to this task. Ultrasound has characteristics not found in optical measurements: it is independent of radiation, light intensity, and environmental turbidity, and it can make measurements in real time [3]. These advantages of ultrasound have led it to be used in the investigation of nuclear reactor interiors as early as the Three Mile Island nuclear accident in the United States [4]. Among ultrasonic techniques, the ultrasonic velocity profile (UVP) is a measurement technique that cannot be ignored. Using the UVP we can obtain real-time velocity profiles inside the fluid, and combined with other measurement techniques, we can more accurately determine the environment and flow velocity of the fluid. Prior to this study, the UVP method has been applied to leakage detection by R. Nishiwaki et al. and T. Ihara et al. [5, 6], and shape reconstruction using phased array transducers by T. Kawachi et al. [7]. Meanwhile, sectorial array transducers have been applied to obtain leakage point by H. Kikura et al. combined with UVP [8] and two-phase flow measured using sectorial array transducer combined with UVP and PIV by M. Batsaikhan [9].

In this study, 2D ultrasonic shape measurement experiments and UVP experiments were conducted using a sectorial array transducer in order to detect the location and shape information of the simulated leak port and simulated fuel debris. During the 2D shape reconstruction conducted by sectorial array transducer, the full matrix capture (FMC) method and total focusing method (TFM) algorithm were applied. By combining the results of both shape measurement and flow velocity profile, the location and shape information of the simulated leak and simulated fuel debris can be more accurately inferred.

2. Method

2.1 Principle of ultrasonic velocity profile

UVP technology is based on pulsed ultrasound echography [3], when the ultrasound beam emitted by the transducer collides with the tracer particles in the fluid, a reflected beam will be generated on the surface of the tracer particle, which is opposite to the direction of the emitted ultrasound beam and is called echo signal. The echo signal will be received by the transducer. Because the particles remain in motion during the process, the echo signal is Doppler-shifted compared to the emitted ultrasound beam. By

analyzing the Doppler shift frequency, the velocity of the tracer particle can be measured and thus the velocity of the fluid can be known. The distance from a tracer particle to a transducer and the velocity of this tracer particle can be expressed as Eq. 1 and Eq. 2:

$$x = \frac{cT}{2} \tag{1}$$

$$u = \frac{cf_d}{2f_0} \tag{2}$$

Where T is the time delay and c is the sound velocity, f_0 is the basic frequency of the transducer, f_d is the Doppler-shift frequency, processing the f_d is the main part of UVP method.

The above principle is obtained in a one-dimensional environment. In a two-dimensional environment, UVP measurements are usually performed by two transducers. As shown in Figure 1, two transducers emit two ultrasonic beams at the same time, which propagate forward along two measurement lines and intersect at a point where the velocity on each measurement line is calculated in the same way as in the one-dimensional case, and after obtaining the velocities on the two measurement lines, the final velocity at the point is obtained by synthesizing the equations as shown in Eq. 3, Eq. 4, and Eq. 5. We can find that the more intersection points of the measurement lines, the more velocities are measured in the same area and the more accurate the measurement is.

$$u_1 = V_x \sin\alpha + V_y \cos\alpha \tag{3}$$

$$u_2 = -V_x \sin\alpha + V_y \cos\alpha \tag{4}$$

$$\boldsymbol{u} = \begin{pmatrix} V_x \\ V_y \end{pmatrix} = \begin{pmatrix} \frac{u_1 - u_2}{2sin\ \alpha} \\ \frac{u_1 + u_2}{2cos\ \alpha} \end{pmatrix} \tag{5}$$

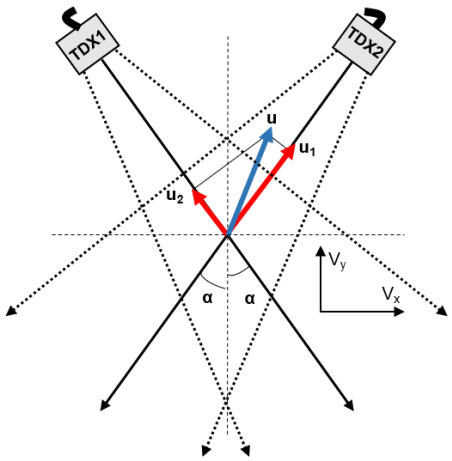

Figure 1: Basic principle of vector reconstruction using two transducers

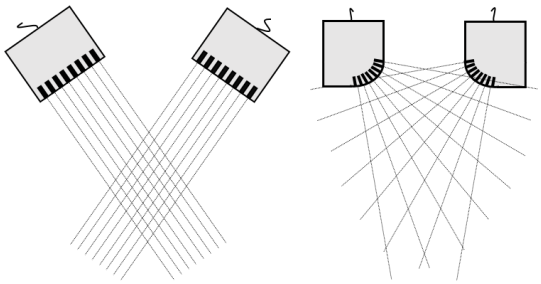

(a) Linear array transducer (b) Sectorial array transducer

Figure 2: Measurement range with 2 types of array transducer

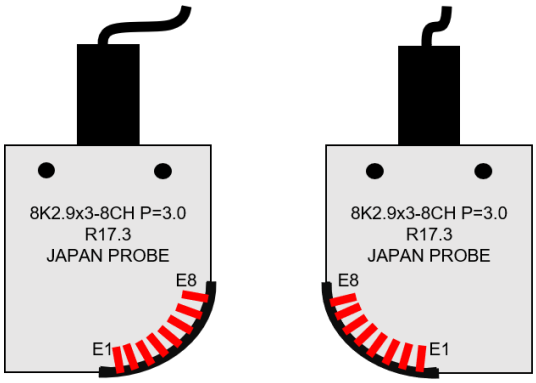

Figure 3: Schematic diagram of sectorial array transducer

2.2 Ultrasonic array transducer

In contrast to a single transducer, an array transducer contains multiple array elements within a single probe, which means that it can emit multiple ultrasonic beams simultaneously. Similar to the one-dimensional case, two-dimensional measurements can be measured by a combination of at least 2 array transducers. The spatial resolution of the measurement can be significantly improved by using such transducer.

As shown in Figure 2, compared with linear array transducers, sectorial array transducers have wider measurement range when element numbers are same. Based on this, sectorial array transducer is selected in this experiment. The schematic diagram of an 8 channels sectorial array transducer is shown in Figure 3.

2.3 Full matrix capture and total focusing method

Firstly, in order to introducer the full matrix capture (FMC) and TFM, the introduction of traditional phased array (PA) process will be conducted. PA technology uses multiple independent transmit-receive channels. In the transmission process, the standard PA system imposes a time delay on each element of the PA transducer, so as to generate an ultrasonic beam with specific acoustic characteristics through the interference of each wave surface. In the receiving process, the system also applies a time delay to the signals received by each element so that they are in phase during the hardware summation process. The summed and digitized A-scan signal is transmitted to the computer for display and recording.

Comparing to traditional method, the FMC is a data

method based on ultrasonic array transducer. In an array ultrasound, when one array element emits an ultrasonic beam, a different order on the reception of other array elements leads to a change in the result. In the FMC method, each possible transmit/receive combination in an array ultrasound (number of array elements is n) is formed into a $n \times n$ matrix, which is the full matrix. In the traditional PA acquisition process, the original basic signal is processed at the hardware level, so it cannot be used for offline software processing. In contrast, FMC technology involves capturing and recording all possible time-domain signals (A-Scans) from each pair of transmitter-receiver elements in the array [10], as shown in Figure 4.

TFM is an algorithm based on the FMC method. Usually it is called TFM post-processing. The TFM post-processing algorithm processed as follows:

Divide the target area (in the X, Z plane) into a grid. Then the signals from all the elements in the array are added together to synthesize the focal point of each point in the grid. The image intensity at any point in the scan I(x, z) is given by the Eq. 6 [11]:

$$I(x,z) = \left| \sum h_{tx,rx}\left(\frac{\sqrt{(x_{tx}-x)^2+z^2}+\sqrt{(x_{rx}-x)^2+z^2}}{c_1}\right)\right| \quad \text{for all tx, rx} \tag{6}$$

The resolution has been improved significantly and the signal noise ratio (SNR) is also increased. In addition, the TFM image increase the probability of locating defects at the edge of the measurement location.

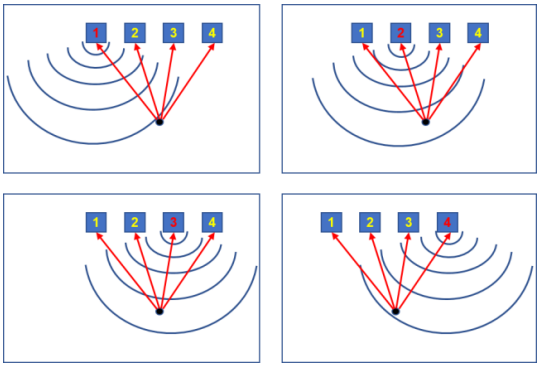

(a) Transmit/receive combination in FMC method (4 elements)

Emitting Elements \ Receiving Elements	1	2	3	4
1	A11	A12	A13	A14
2	A21	A22	A23	A24
3	A31	A32	A33	A34
4	A41	A42	A43	A44

(b) 4×4 full matrix generated by FMC

Figure 4: Principles of full matrix capture method

3. Experimental setup and configuration

In this study, both UVP experiment and 2D shape reconstruction experiment were carried out. In the UVP experiment, an 8ch/side ultrasonic sectorial array transducer from Japan Probe was applied, and the UVP-DUO multiplexer was used in signal receiving and processing. In 2D shape reconstruction experiment, transducer kept same with UVP experiment, and the pulse receiver utilized the JPR-10C-8CH from Japan Probe. Two experiment conducted one by one.

The experiments were conducted in a laboratory scale tanks, which is a rectangular acrylic box with a size of 1200 mm×450 mm×450 mm. Tap water was the measured fluid in this experiment, and the height is 290 mm from the bottom. Nylon particles with 8μm diameters was used as tracer particle in this experiment (Ideal particles should have specific weight similar to that of the fluid they flow in, but should have different acoustic impedance to form strong reflections). Two sectorial array transducers were placed into the water, and with a height of 150 mm, the distance between two transducers is 90 mm, and they are placed above the leakage point of the fluid container (shown in Figure 5). The flow was controlled by the control value and the flowmeter, the flow rate was controlled in the 10L/min and the accuracy of it is ±5%. The parameters of UVP measurement and shape reconstruction measurement are shown in Table 1 and Table 2.

Table 1: 2D shape reconstruction measurement parameters

Parameters	value
Cycles number	8
PRF [kHz]	2.6
Supplied voltage for each element [V]	150
Maximum depth [mm]	294
Number of profiles per elements	3600
Gain	30
Number of channels	265
Channel distance [mm]	0.75
Channel width [mm]	0.75
Sound speed [m/s]	1507
Frequency [MHz]	8

Table 2: UVP measurement parameters

Parameters	value
Cycles number	4
Supplied voltage for each element [V]	150
Sampling rate [MHz]	60
Gain	30
Sound velocity [m/s]	1507

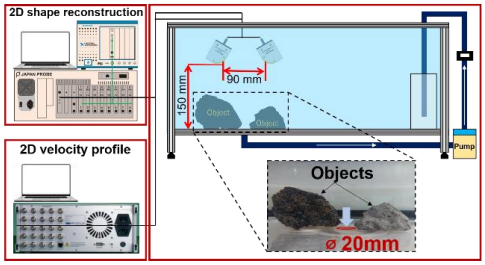

Figure 5: Schematic diagram of experiment setup

4. Result and discussion

To optimize the result of the experiment, the sectorial transducers are placed at an angle of 20 degrees to ensure that the signals emitted from all elements can participate in the measurement and forming images. Meanwhile, to make the result more accurate, the experiment of shape measurement was repeated 5 times by changing the location of transducers horizontally. Transducers are connected to the ultrasonic pulse receiver (JPR-8CN, Japan Probe). Then, After the UVP measurement, the UVP result was combined with the shape measurement result manually. The shape measurement result was shown in Figure 6, the UVP result was shown in Figure 7.

After measurement, the result of UVP and shape measurement was overlapped as shown in Figure 8, we can clearly find that the simulated leakage point and fuel debris detected using the TFM method is consistent with their presumed location. This result demonstrated that the TFM worked successfully in the two-dimensional shape measurement.

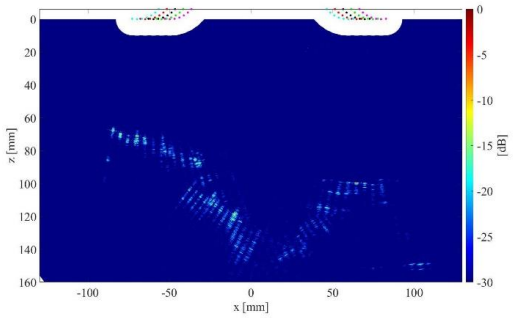

Figure 6: Result of 2D shape reconstruction using TFM algorithm

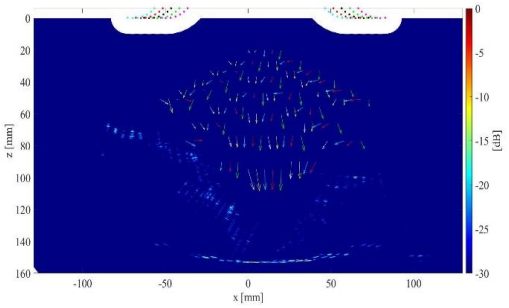

Figure 7: Result of 2D velocity profile using UVP method

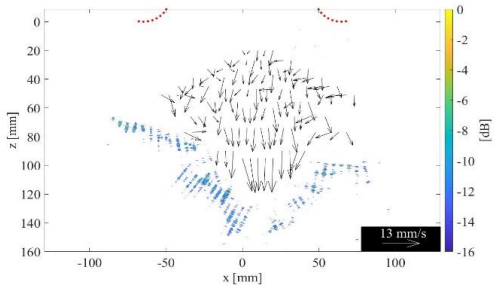

Figure 8: overlapped result with velocity profile and shape reconstruction

5. Conclusion

In the present study, a method for real-time measurement of fluid velocity profiles and in-plane reconstruction of shapes using ultrasound was proposed for the detection of internal reactor leaks and fuel debris in the disassembly of the Fukushima Daiichi nuclear power plant. To make the method more accurate, a sectorial array transducer with TFM algorithm was used for the experiment. 5 measurement results were integrated in a figure to make the result less defection, and the experimental results show a high match between the shape reconstruction using the TFM algorithm and the flow velocity measurements using the UVP method, which demonstrates the validity of this experiment and this method.

References

[1] Tokyo Electric Power Company Holdings Corporation: "Progress of Medium- and Long- Term Roadmap" (2019). http://www.tepco.co.jp/decommission/information/committee/roadmap_progress/pdf/2019/d191219_05-j.pdf (Reference date: April 4, 2021).

[2] Tokyo Electric Power Company Holdings: Decommissioning Plan of Fukushima Daiichi Nuclear Power, Inc. (TEPCO). http://www.tepco.co.jp/en/decommision/index-e.html (accessed 17.05.28).

[3] Takeda Y: Development of an ultrasound velocity profile monitor, Nuclear Engineering and Design, 126 (2) (1991), 277-284.

[4] Beller L S. et al.: Three Mile Island Reports, GEND-INF-012, Idaho Falls, Idaho, USA, (1984).

[5] Nishiwaki R, et al.: Development of a remote water leakage localization system combined with phased array UVP and robot, 11th International Symposium on Ultrasonic Doppler Methods for Fluid Mechanics and Fluid Engineering, (2018).

[6] Kikura H, et al.: Study on ultrasonic measurement for determination of leakage from reactor vessel and debris inspection, The 11th National Conference on Nuclear Science and Technology, (2015).

[7] Kawachi T, et al.: A study on two-dimensional vector flow mapping by Echo-PIV with total focusing method, WIT Transactions on Engineering Sciences, 120 (2018), 275-286

[8] Kikura H, et al.: Study on ultrasonic measurement for determination of leakage from reactor vessel and debris inspection, The 11th National Conference on Nuclear Science and Technology, (2015).

[9] Batsaikhan M, et al.: Velocity measurement on two-phase air bubble column flow using array ultrasonic velocity profiler, Multiohase Flow: Theory and Applications, (2018), pp. 89-100.

[10] Patrick T & Daniel R: Development and validation of a full matrix capture solution, The 9th International Conference on NDE in Relation to Structural Integrity for Nuclear and Pressurized Components, (2012).

[11] Holmes C, Drinkwater B, Wilcox P, Post-processing of the full matrix of ultrasonic transmit-receive array data for non-destructive evaluation, NDT&E International, (2005).

30 Awards


ISUD 2021 – Ubertone Student Award
for outstanding scientific contribution
2021 AWARD
PROUDLY PRESENTED TO
Kim Mishra
Zürich, June 15, 2021
Dr. S. Fischer
Ubertone
Dr. G. De Cesare
ISUD Board Chair


ISUD 2021 – Incipientus Student Award
for outstanding scientific contribution
2021
AWARD
PROUDLY PRESENTED TO
Lucas Grob
Zürich, June 15, 2021
Dr. R. Kotzé
Incipientus
Dr. J. Wiklund
Incipientus
Dr. G. De Cesare
ISUD Board Chair


ISUD 2021 – Met Flow Student Award
for outstanding scientific contribution
2021 AWARD
PROUDLY PRESENTED TO
Nisa Sardini
O. Mariette
Met-Flow
Dr. G. De Cesare
ISUD Board Chair
Zürich, June 15, 2021

31 Group Foto

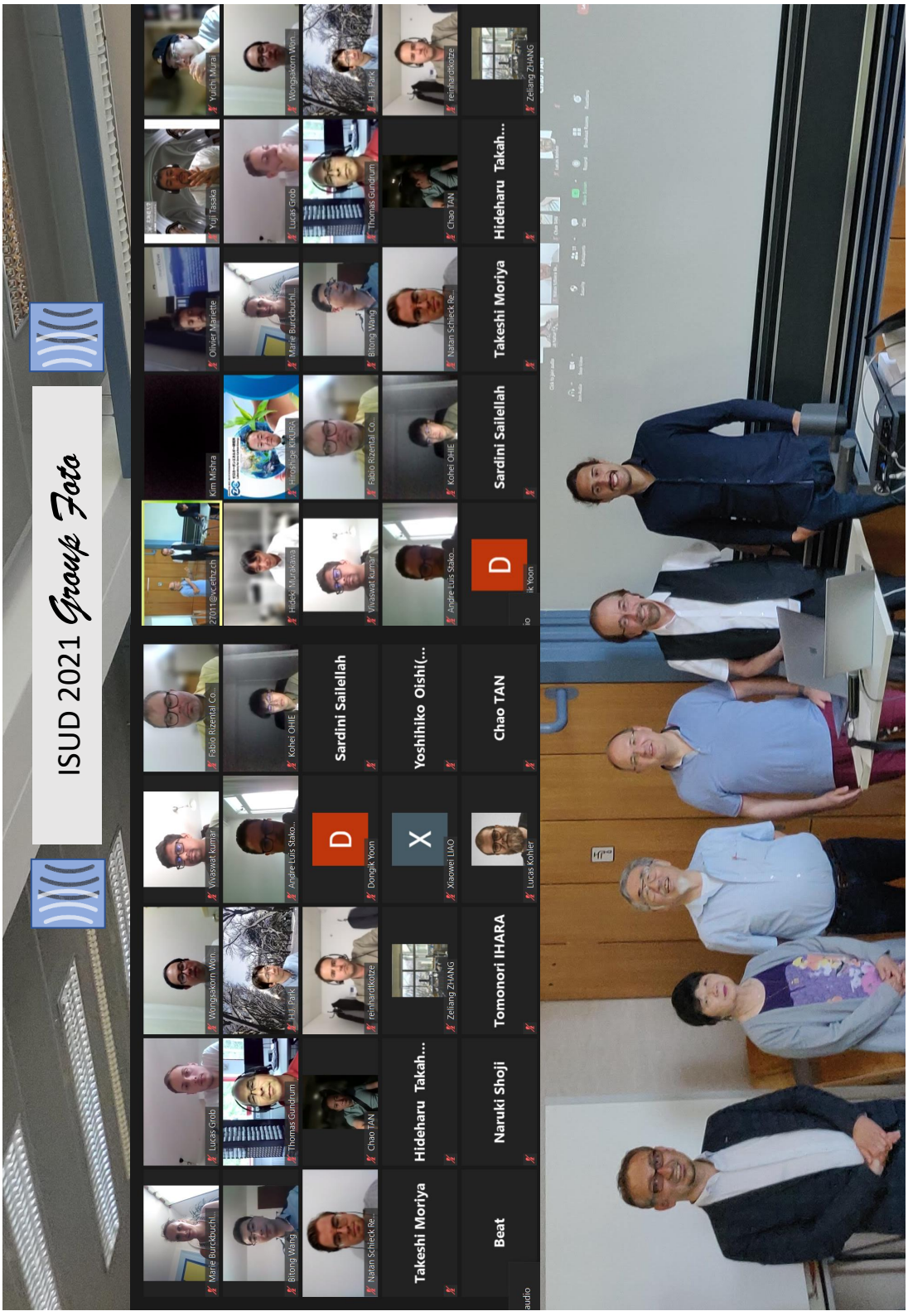
ISUD 2021 Group Foto